UNIVERSIDADE DE LISBOA
FACULDADE DE CIÊNCIAS
DEPARTAMENTO DE FÍSICA

Hunting for Brown Dwarfs in Corona Australis

André G. C. Baptista

Mestrado em Física
Especialização em Astrofísica e Cosmologia

Dissertação orientada por:
Koraljka Mužić
Karolina Kubiak

2021

Abstract

Brown dwarfs are substellar objects with masses ranging from 0.08 Solar masses at the high end, down to those overlapping with masses of giant exoplanets. The study of young brown dwarfs is key to understanding both planet- and star-formation processes. It helps constrain the low-mass regime of the Initial Mass Function which, for nearby star-forming regions, is well characterized down to $\sim 10 - 20$ Jupiter masses but becomes loosely defined for lower mass values. Having in mind that young brown dwarfs are very faint sources, a complete census of brown dwarfs in nearby star-forming clouds, where they can be more easily detected, is imperative to improve our knowledge on both planetary and stellar formation models, as well as the shape of the substellar Initial Mass Function.

The Corona Australis cloud is one of the closest star-forming regions to the Solar system, at a distance of ~ 150 parsecs. In 2017, it was observed using the Suprime-Cam instrument at the Subaru telescope. These observations have a field-of-view of ~ 0.255 deg^2, and result in the deepest optical photometric catalog of the region with magnitudes ranging down to 23 mags in the I-band, which is equivalent to ~ 3 Jupiter masses at a distance of 150 pc (with no extinction) using the AMES-COND model. The work of this thesis consists of the data reduction of this dataset and of the selection of a list of candidate sources for future spectroscopic observations in Corona Australis. The PSF photometry has been performed using the *Source-Extractor* and *PSFEx* software and calibrated with the help of the DENIS I-band photometry, and colours were obtained by cross-matching the dataset with the VISTA Hemisphere Survey catalog. This resulted in an IJKs catalog of 21 133 sources.

After photometry, we selected sources from our catalog which presented colours consistent with those of young objects. From the resulting list of sources, we made two further selections. One for the sources present in the *Gaia* EDR3 catalog, selecting those with proper motions and parallaxes similar to spectroscopically confirmed members of Corona Australis. This selection produced a list of 15 objects. For the other selection, below the *Gaia* limit, we use only colours. Most of the sources we are interested in are substellar objects and are, hence, very faint. Because of this, they were not detected by *Gaia*. As such, we selected sources which are below the *Gaia* limit (I $\sim$ 19 mag) and above 22 mag. This method resulted in a list of 313 sources, where 145 objects present colours for masses below 5 Jupiter masses, and with most of our candidates residing in the planetary-mass regime (if indeed confirmed as members of Corona Australis) according to the AMES-COND models. It should be stressed, however, that this selection method is expected to produce a large number of contaminants and therefore requires further confirmation through spectroscopy observations. The total list of candidates for follow-up spectroscopy observations is then composed of 328 sources. During the Subaru observations, an H_α catalog was also produced. H_α information from this catalog was used to flag possible active accretors in our list of candidates, although only 3 sources from our list of 328 candidates present bright H_α emission.

Using empirical models from Pecaut and Mamajek (2013), we built an extinction map of the observed field. This extinction map was used alongside the *Besançon* galaxy model to estimate the number of contaminants in our list of candidates for follow-up spectroscopy observations. We found a contamination rate of $\sim 90\%$, meaning we expect to confirm ~ 30 new planetary

mass brown dwarfs. Having only $\sim$ 100 of these objects been identified so far, our spectroscopy efforts may increase the current budget of known free-floating planetary mass objects by $\sim$ 30%.

The preparatory work for the follow-up spectroscopy observations is also developed here. These observations will be done using the K-band Multi Object Spectrograph at the Very Large Telescope. Seven different fields are proposed encompassing 219 sources from our selection list. Using the Exposure Time Calculator, KMOS-dedicated software and the observation preparation tool *p2*, we estimate a full exposure time of six hours and twenty-five minutes.

Keywords: Brown Dwarfs, Corona Australis, Data Reduction, Photometry, Subaru

Resumo

Anãs castanhas jovens são cruciais para percebermos os mecanismos por detrás da formação estelar e planetária. Elas ajudam-nos a caracterizar a Função de Massa Inicial que, para as regiões de formação estelar mais próximas, está bem definida até cerca de $10 - 20$ Júpiters. Regiões de formação estelar são os lugares na Via Láctea onde a maior parte das estrelas e objectos sub-estelares são formados. Ao observar estas regiões, podemos detectar anãs castanhas quando estas ainda estão em estágios de formação e evolução. A Função de Massa Inicial é uma função que representa a distribuição de massas de objectos formados numa dada região. No entanto, para massas mais baixas, a Função de Massa Inicial ainda não tem uma definição bem estabelecida. Está melhor definida para massas maiores (objectos mais luminosos) e existe um debate sobre a universalidade desta função que ainda não obteve um consenso. Por isso, a detecção de anãs castanhas em regiões de formação estelar é importante para obtermos uma versão completa da Função de Massa Inicial e para obter conhecimentos à cerca dos mecanismos de formação tanto de estrelas como de planetas.

Existem vários cenários hipotesizados para a formação de anãs castanhas. Diferentes observações ao longo dos anos têm favorecido certos cenários em prol de outros, mas ainda não existe um consenso para o mecanismo de formação dominante nem a frequência relativa com que cada cenário acontece. As anãs castanhas são objectos particularmente pouco brilhantes, por isso a sua detecção torna-se mais fácil para as regiões de formação estelar mais próximas. Corona Australis é uma destas regiões de formação estelar, a apenas uma distância de ~ 150 pc do sistema Solar. Esta região foi primeiro identifacada na década de 1910s e tem sido extensivamente observada, mas estas observações direccionam-se maioritariamente aos objectos mais brilhantes desta região. As observações também tem sido direccionadas maioritariamente para o *Coronet Cluster*, um agregado de estrelas a Oeste da nuvem estelar onde se espera que grande parte da população da região estelar resida. Recentemente, esta associação foi observada por Bo Reipurth em Maio de 2017 usando o instrumento Suprime-Cam no telescópio Subaru. Estas observações produziram o catálogo óptico mais sensível desta região, tendo sido observada na banda I. O trabalho apresentado nesta tese consiste na redução destas observações e na selecção de objectos para observações espectroscópicas consequentes. Esta selecção é feita prioritizando objectos que apresentem propriedades cinemáticas semelhantes às de membros de Corona Australis espectroscopicamente confirmados e/ou cores características de fontes luminosas jovens. Com este fim, o catálogo foi calibrado em relação ao catálogo DENIS e foi feita uma correspondência cruzada com o catálogo VHSDR6 de forma a obtermos cores para estes objectos. Assim, construímos um catálogo de 21 133 objectos detectados nesta região. Depois, representámos a fotometria do nosso catálogo num diagrama cor-magnitude. Este diagrama permite identificar objectos jovens e prováveis membros da nuvem, já que estes vão apresentar cores avermelhadas características destes objectos. Desenhámos uma linha arbitrária no diagrama cor-magnitude e selecionámos objectos do nosso catálogo mais vermelhos que esta linha. Isto resultou numa lista de 650 objectos que foram redireccionados para o nosso processo de selecção baseado nas propriedades cinemáticas. As propriedades cinemáticas de alguns dos objectos neste catálogo foram obtidas do catálogo produzido pela missão *Gaia*. Utilizámos membros confirmados espectroscopicamente para determinar os

valores cinemáticos característicos da nuvem. Objectos selecionados pelo diagrama cor-magnitude com valores cinemáticos semelhantes aos dos membros de Corona Australis foram selecionados. Esta selecção produziu uma lista de 15 candidatos com cores características de objetos jovens e propriedades cinemáticas semelhantes às dos membros da nuvem. Nem todos os objectos no nosso catálogo têm um par no catálogo *Gaia* por serem pouco brilhantes e, consequentemente, não terem sido detectados durante a missão *Gaia*. Atendendo a isto, uma lista de 313 candidatos foi produzida, onde objectos abaixo do limite da missão *Gaia* (I $\sim$ 19 mag) e acima de I = 22 mag, presentes na lista de selecção de objectos por cor-magnitude, foram seleccionados. 145 desses candidatos apresentam massas mais baixas que 5 Júpiters e a maior parte pertence ao regime planetário da função de massa (de acordo com o modelo AMES-COND). No total, a nossa lista de candidatos para observações espectroscópicas futuras é composta por 328 objectos. Durante as observações de Maio de 2017, Corona Australis também foi observada usando um filtro H_α. Como não existe um cátalogo público de Corona Australis para observações em H_α, não foi possível calibrar este catálogo. No entanto, não deixa de ser possível identificar os objectos mais brilhantes neste filtro. Isto é importante porque a emissão de H_α pode indicar a existência de acreção numa fonte luminosa, que é um sinal de juventude. No entanto, apenas 3 dos 328 candidatos apresenta uma forte emissão de H_α.

Usando os modelos empíricos de Pecaut and Mamajek (2013), cálculamos a extinção presente em alguns dos objectos no nosso catálogo. Com estas extinções, conseguimos construir um mapa da extinção presente no campo observado pelo telescópio Subaru. Este mapa foi usado para estimar o número de contaminantes na nossa lista de candidatos. Estes contaminantes serão estrelas vermelhas ou galáxias por detrás da nuvem que são erroneamente identificadas como objectos jovens. Outras hipóteses incluem a presença de estrelas gigantes existentes no interior da nuvem, ou, menos provavelmente, objectos jovens entre nós e Corona Australis. Calculámos uma taxa de contaminação de 90%, o que significa que esperamos confirmar cerca de 30 anãs castanhas jovens com massa no regime planetário. Até agora, foram catalogados $\sim$ 100 objectos flutuantes de massa planetária, logo as nossas observações espectroscópicas poderão aumentar a amostra destes objectos por $\sim$ 30%.

A preparação para as observações espectroscópicas futuras também é apresentada nesta tese. Estas observações vão ser feitas com o instrumento K-band Multi Object Spectrograph presente no *Very Large Telescope*. Vão ser executadas na banda H + K e são dispostas em sete campos diferentes que englobam 219 objectos da nossa lista de candidatos. A Exposure Time Calculator do European Space Observatory foi utilizada para determinar a melhor configuração para o número e duração de exposições. O resultado são dez exposições de 120 segundos cada. A combinação do programa *KMOS Arm Allocator* com a aplicação *p2 tool* permitiu-nos calcular o tempo total de observação para cada exposição, que resultou em 55 minutos para cada execução totalizando seis horas e vinte-e-cinco minutos de tempo de telescópio.

Palavras-Chave: Anãs Castanhas, Corona Australis, Fotometria, Redução de Dados, Subaru

Acknowledgments

I want to start by thanking my supervisors Koraljka Mužić and Karolina Kubiak. They were always available to discuss the progress and details of this work. They constantly checked if everything was going smoothly and if I needed any help, in which case they would point me in the right direction. To Kora, I want to give a special thanks for reaching out to me and invite me to work with her once again. I feel very lucky to have crossed paths with her, she is a very dedicated and thoughtful mentor. To Karolina, I want to thank her for the best crash course on academic presentation and writing I could have asked for. Her lessons have already earned me a lot of compliments on my poster presentations, seminars and written reports. I hope this thesis makes justice to her teachings as well. I also want to thank Víctor Almendros-Abad, one of our colleagues in our work group. Victor always stepped up when needed, providing knowledge on subjects that complemented my work.

I am immensely grateful for having shared this MSc journey with wonderful colleagues. Ana, Cipri, Miguel, Victor, you are people who I will cherish for the rest of my life. Many of my best memories were made with you.

My oldest friends, Afonso, Maxy, Carlos, DevM, and some more recent ones, Bee, Beatriz, Ned, Sara, have been my emotional support over the past few years. I keep finding meaning in life in the stories we write together.

I must also mention my dear friends at *O Covil de Lisboa*, where many late nights were spent working on this thesis, whether it was tackling a particularly challenging step or researching papers for hours on end. The setting and the music were always a great help to keep me from getting stuck inside my own head while working, and whenever in need of a break I would always have the company and words of encouragement from friends telling me to keep pushing.

To my cat Charlie, thank you for being the best boy. You will never understand just how much you have already helped me. I also find it particularly cute that, even though we live in a big house, you are always in the same room as me. You are a son to me, and I love you very much.

Contents

List of Figures

List of Tables

Abbreviations

2MASS - Two Micron All-Sky Survey
BD - Brown Dwarf
CCD - Charge-Coupled Device
CMD - Colour-Magnitude Diagram
CrA - Corona Australis
DANCe - Dynamical Analysis of Nearby Clusters
DENIS - Deep Near Infrared Survey of the Southern Sky
ESO - European Space Observatory
ETC - Exposure Time Calculator
HRD - Hertzsprung-Russell Diagram
IMF - Initial Mass Function
IR - Infrared
KARMA - KMOS ARM Allocator
KMOS - K-band Multi Object Spectrograph
NIR - Near-Infrared
PMs - Proper Motions
PMS - Pre-Main Sequence
PSF - Point-Spread Function
SFR - Star-forming Region
SMOKA - Subaru Mitaka Okayama Kiso Archive
SNR - Signal-to-Noise Ratio
SONYC - Substellar Objects in Nearby Young Clusters
VHS - VISTA Hemisphere Survey
VISTA - Visible and Infrared Survey Telescope for Astronomy
VLT - Very Large Telescope
WCS - World Coordinate System
YSO - Young Stellar Object
ZAMS - Zero-Age Main Sequence
ZP - Zero-Point

Chapter 1

Introduction

The main motivation of this work is the search of young substellar objects - specifically young brown dwarfs (BDs) - in the Corona Australis (CrA) star-forming region (SFR) using a dataset obtained via the Suprime-Cam on the Subaru telescope. These observations were made by Bo Reipurth in May of 2017 and were downloaded from the Subaru Mitaka Okayama Kiso Archive (SMOKA). The work presented here produces a list of candidate sources for future spectroscopic campaigns in the CrA region with the aim of providing a complete substellar census of the star-forming cloud.

In this introductory chapter, concepts surrounding star-formation, SFRs and BDs (including the spectral features of these objects) is covered. An overview is provided of the Substellar Objects in Nearby Young Clusters (SONYC) survey as well as of the CrA region, and a review of the Initial Mass Function (IMF) - one of the main motivations behind projects of this nature - is also made.

The starting point for the work of this thesis is the reduction of a dataset acquired while observing the CrA SFR (Chapter 2). The data was reduced manually using our own routines written in *Python*. Each step taken during the reduction is explained, with exemplary figures for each process shown in dedicated sections. The end result of this process is a catalog with photometric measurements as well as the positions for each detected source, which were later cross-matched with existing catalogs of the CrA region in order to compile as much information as possible about these objects.

This collection of information was used in the follow-up step of membership determination: since some of the objects detected were background (or foreground) sources to our region of interest, a selection was needed to ascertain which of these sources are relevant to the subject of this work. This process of candidate selection is explained in the chapter of the same name (Chapter 4) along with the methods that were implemented to perform the selection. H_α emission from the sources in our dataset is also studied and a list of bright emitters is produced. Extinction was also estimated for the sources in our catalog leading to an extinction map of the observed field. With this map, the contamination rate of our list of candidates is estimated.

Later on, the preparatory work for the follow-up spectroscopy observations is made in Chapter 5. Here, the instrument which will be used to perform follow-up spectroscopy observations - the K-band Multi Object Spectrograph (KMOS) at the Very Large Telescope (VLT) - is introduced. The proposed observations using KMOS, as well as the exposure time considered for these observations, are shown in later sections of this chapter. Lastly, to calculate the total amount of time needed for follow-up spectroscopy, a walkthrough of a

KMOS ARM Allocator (KARMA) and *p2 tool* run can be found in the last sections of this chapter.

Finally, a summary of this work can be found in Chapter 6.

1.1 Star-Formation

Stars are created in molecular clouds - complexes of gas and dust in the interstellar medium. A cloud can be described as a region in the interstellar medium with a density larger than $10 - 30$ atoms per cm^3 (Schulz, 2005), being mostly comprised of hydrogen. Molecular clouds are the densest regions in the interstellar medium. They are created by gravitational instabilities in a relatively clumpy region of the interstellar medium (Elmegreen, 1989). The interstellar medium is constantly subject to perturbations whether from stellar winds from massive stars, cloud collisions, photoevaporation (the evaporation of dust and molecules by the ultraviolet radiation of a nearby O-type star; Oort and Spitzer 1955; Hollenbach and Tielens 1999), photoionization or supernova explosions (Schulz, 2005). These events produce shockwaves which are compressive and dependent of the interstellar magnetic field (Schulz, 2005), and originate the gravitational instabilities which spur the formation of molecular clouds. Molecular clouds are self-gravitating and move as a singular entity around our galaxy, with each cloud presenting its own peculiar velocity. Molecular clouds have a lifespan $\sim$ 10 million years (Myr; Schulz 2005) which means existing clouds in our galaxy are young (Stahler, 1984; Schulz, 2005). Their sizes can vary between 1 and 200 parsecs (pc; with an average size of 10 pc) and their masses range from $10 - 10^6$ Solar masses ($M_\odot$; with an average mass of up to ~ 100 $M_\odot$; Schulz 2005). The more massive clouds - usually called giant molecular clouds - have masses $> 10^4$ $M_\odot$ and there are about 4 000 of them in our galaxy (Schulz, 2005). Still, these clouds only show 5% of the expected star-formation rate were they supported only by thermal pressure (Williams and McKee, 1997). This means additional dynamics and physical processes inducing instability are at play inside these regions.

Molecular clouds are mostly composed of H_2 molecules with densities $\sim 10^2 - 10^6$ H_2 molecules per cm^3 (Schulz, 2005). The formation of H_2 molecules is promoted by the presence of dust grains in the region meaning that molecular clouds are areas of particularly high *extinction*. Extinction was first described by Trumpler (1930) as a selective absorption of light which varies with wavelength and increases with distance. They also noted that extinction is much more significant towards the galactic plane. As such, the observed colour of a source affected by extinction is different from its true colour. Because this absorption is biased towards shorter wavelengths, the real colour of a source is reddened - this *reddening* effect is especially relevant when observing clouds since these constitute strong absorption mediums. For longer wavelengths (i.e., $\lambda > 100$ μm), the absorption and scattering effects are negligible and we are only able to observe thermal emission from dust. At sub-millimeter wavelengths and longer, we can detect thermally-induced vibrational and rotational transitions inside these clouds allowing astronomers to map their structures using millimeter and sub-millimeter radio telescopes.

It is in molecular clouds that stars are formed. At temperatures $\sim$ 100 Kelvin (K; Schulz 2005), these clouds are not gravitationally unstable in order to induce star-formation, but, subject to instabilities from the interstellar medium, molecular clouds can fragment into clumps and cores (Blitz and Shu, 1980). Fragmentation is the entire process from instabilities in the interstellar medium to the formation of stars. Clouds are fragmented into sub-clouds which, in turn, fragment to smaller structures – clumps and cores. Cores are gravitationally bound structures which form

single or binary stellar systems. Clumps are larger structures which are also gravitationally bound and which lead to the formation of multiple stellar systems. Clumps remain gravitationally bound after their formation, creating stellar clusters. These clusters, embedded in the molecular clouds, are numerous across the galaxy and are thought to be the main place where stars are born (Clarke et al. 2000, Lada and Lada 2003). Most stars are presumed to have been born in big clusters with more than 100 members (Adams and Myers, 2001), and the most massive stars for each cluster are expected to be found at their center (Lada and Lada, 1991; Hillenbrand et al., 1998; Nürnberger et al., 2002; Jiang et al., 2003). Another interesting observation is that the mass of these clusters is only a fraction of the clouds in which they were formed (there seems to be a cut-off at masses $> 1\,000$ $M_\odot$ for stellar clusters; Schulz 2005), with Lada and Lada (2003) determining a star-formation efficiency for clusters of 10%−30%. This is still higher than the 5% efficiency seen in our galaxy (Williams and McKee, 1997). Along with the high frequency of stellar clusters (2−4 Myr^{-1} kpc^{-2}; Lada and Lada 2003), this is why most stars are expected to have been formed in these clusters (other places where stars can form are planetary nebulae and supernova remnants). Because members of these clusters share distance, age and chemical composition, they constitute a homogeneous sample valuable to studies of stellar evolution. Clusters with ages $t > 5$ Myr are generally no longer associated to the molecular cloud they originated from (Schulz, 2005). These are called *open clusters* and the timescale and dynamics in these clusters affect the evolution of their members. Members of open clusters are less gravitationally bound since the interstellar molecular content has vanished, whether through star-formation or photoevaporation.

The condition for a cloud, clump or core to be gravitationally bound is given by the Virial theorem:

$$\frac{1}{2}I > 2K + M + W \tag{1.1}$$

Here, I is a function for the inertia of a cloud. K is the net kinetic energy of the cloud (total kinetic energy − pressure energy from the surrounding gas). M is the net magnetic energy with reference to the background medium. W is the gravitational binding energy of the cloud. When in Virial equilibrium $I \sim 0$ and for $M = 0$, we can use the gas law (Schulz, 2005):

$$K = \frac{3}{2}\bar{P}V \tag{1.2}$$

where V is the volume of the cloud (or clump, core) and $\bar{P}$ is the mean total (thermal + turbulent) pressure given by (Schulz, 2005):

$$\bar{P} = P_0 + \frac{3\pi a}{20}G\Sigma^2 \tag{1.3}$$

where P_0 is the surface pressure from the background medium (for the case of the cloud) or from the molecular cloud (for the case of a clump, core), a is a parameter detailing the sphericity of the structure, G is the gravitational constant and Σ is the average projected surface density:

$$\Sigma = \frac{M}{\pi R^2} \tag{1.4}$$

where M and R are the mass and radius, respectively, of the cloud (or clump, core). Equation 1.1 can then be rewritten as:

$$W > \frac{3}{5}a\frac{GM^2}{R} \tag{1.5}$$

for ideal conditions. When the M component is non-negligible, thermal and magnetic pressure push back against gravity and the cloud (or clump, core) is in a state of magnetohydrostatic

equilibrium (Shu, 1977; Shu et al., 1987). This, along with turbulence from shockwaves, may help explain the observed slow star-formation rates.

In 1902, J. Jeans applied the definition of the gravitational potential ($\nabla^2\phi = 4\pi G\rho$), the equation of continuity ($\frac{\partial\rho}{\partial t} - \nabla(\rho\mathbf{v}) = 0$) and the equation of motion described by Euler's equation ($\rho\frac{\partial\mathbf{v}}{\partial t} + \rho\mathbf{v}\cdot\nabla\mathbf{v} = -\nabla P + \mathbf{F}$) to demonstrate that there is a critical mass (M_J) up from which a cloud or core becomes unstable to density perturbations:

$$M_J = \frac{4}{3}\pi R_J^3\bar{\rho} = 1.6(\frac{T}{[10\text{ K}]})^{3/2}(\frac{n}{[10^4\text{ cm}^{-3}]})^{-1/2}M_\odot \tag{1.6}$$

where $\bar{\rho}$ is the average uniform density and n is the number density of the cloud or core. A core with mass $M > M_J$ may collapse. Star-formation is the process of collapse of molecular clouds in interstellar space. During this process, the core is subject to huge changes with an initial density $\sim 10^{-20}$ g cm^{-3} originating i.e. a Sun-like star with density ~ 1 g cm^{-3} (Schulz, 2005). The size of the core also changes from light years to just a few hundred thousand kilometers in radius, and starting temperatures of a few Kelvins heat up to ~ 30 million K (Schulz, 2005). During this stage, the infall of gas generates optical emission which is absorbed by dust grains envolving the core and is re-emitted as infrared (IR) thermal radiation. The product of this collapse is a *protostar* implying that, at some point, the inflow of matter is counteracted by the internal pressure with the core entering a state of quasi-hydrostatic equilibrium (an oscillating state of contraction and expansion around an equilibrium). Three different stages can be defined for the collapse of a core. In the first stage, the matter in a collapsing core follows a free-fall motion, since there is no internal pressure yet to counteract the pull from gravity. This infall of matter can be reproduced by the equation of motion of an harmonic oscillator (Schulz, 2005):

$$\frac{d^2r}{dt} = -\frac{GM_r}{r^2} = -\frac{4}{3}\pi G\rho r \tag{1.7}$$

where M_r is the mass included within a radius r. Here, it is assumed that the cloud is a uniform isolated sphere (i.e., $M_r = (4/3)\ \pi\ r^3\ \rho \wedge \rho\ \mathbf{v}\cdot\nabla\ \mathbf{v} = 0$), where gravity is the only external force being applied to the core (i.e. external radiation and external pressure from the molecular cloud are not taken into account). The equation for the free-fall time (t_{ff}) can be determined from this relation and yields (Spitzer, 1978):

$$t_{ff} = \sqrt{\frac{3\pi}{32G\bar{\rho}}} \sim 2.1\times10^3\sqrt{\frac{\text{g cm}^{-3}}{\bar{\rho}}}\text{ s} \tag{1.8}$$

If we consider an initial mean density $\bar{\rho} \sim 10^{-19}$ g cm^{-3}, a core takes $\sim 200\,000$ years to completely collapse. But, eventually, due to the rise of internal pressure, this free-fall stage comes to an end. This happens once the core reaches a density value $\sim 10^{-13}$ g cm^{-3} (Schulz, 2005). At this time, the innermost layers of the core are optically thick and energy cannot be released, thus increasing the pressure inside these layers. A first, stabilized core is formed, a few astronomical units wide and weighing only a small fraction of the initial cloud core mass (Schulz, 2005). This core is supported by thermal pressure and enters a Kelvin-Helmholtz timescale (t_{KH}) where the quasi-static protostar thermally adjusts to its own gravity:

$$t_{KH} = \frac{|W|}{L_R} \sim 7\times10^{-5}\kappa_R\frac{M_R^2}{R^3T^4}\text{s} \tag{1.9}$$

where W is the gravitational energy, L_R is the luminosity across the core surface and κ_R is the Rosseland mean opacity of the core. For a Sun-like star ($R = 0.1$ pc $\wedge$ $T = 10$ K $\wedge$ $\kappa_R \sim 1.2$ cm^2 g^{-1}), this timescale is approximately 3×10^7 years (Schulz, 2005). Then, the Kelvin-Helmholtz timescale is $\sim$ 100 times longer than the free-fall stage. During this time, the core undergoes a cycle of contraction and expansion. When contracting, the temperature at the core of the protostar increases and hydrogen molecules are compressed until they are split. After enough hydrogen atoms have been ionized this way, the core is able to adiabatically expand once again. This adiabatic expansion is caused by ***hydrogen burning*** in the core. Ionized hydrogen atoms (protons) form ^{4}He nuclei through the thermonuclear fusion of hydrogen. This process requires very high densities at the core, since protons naturally repulse each other because they are all positively charged. Due to the high temperatures at the core ($> 4 \times 10^6$ K; Reid and Hawley 2005), these protons move very fast, and the highly compressed state of these particles allow for them to be "glued" together when they eventually collide in such a dense environment. Energy is released during this reaction, since not all of the mass from the hydrogen atoms is converted into helium - a portion of it is converted into energy. Photons emerging from this reaction push outwards, expanding the core of the protostar. This cycle can repeat for atoms of higher Z. The result is an optically thick *embryo star* with $M \sim 0.01\ M_\odot$ (Schulz, 2005) and which begins its main accretion stage. This is also called the *zero-age* of a star. It is at this stage that an accretion disk is formed around the core, the object is classified as a *protostar* and the protostar + accretion disk + envelope constitute the *protostellar system*. The accretion disk is disconnected from the stellar surface, since magnetic fields would disrupt the presence of any disk so close to the protostar. Also, there is a minimum distance from the star, corresponding to the sublimation temperature of dust grains ($T \sim 1\,500$ – $2\,000$ K; Schulz 2005), where dust cannot exist. Matter from the surrounding envelope is transported to the accretion disk, which is then fed to the protostar. The inflow of matter prevents radiation from escaping the protostellar core, obscuring both the protostar and accretion disk from observations. Another result is that accretion shocks heat up the outer layers of the protostar expanding its size to a few Solar radii (Schulz, 2005) which stays virtually constant during its accretion phase (Masunaga and Inutsuka, 2000). The internal structure of the protostar evolves as it accretes more mass (Palla and Stahler, 1990; Stahler et al., 1980a,b). The Kelvin-Helmholtz timescale must be much smaller than the accretion time (t_{acc}) for the protostar to be able to thermally adapt to gravitation. The accretion timescale is given by (Schulz, 2005):

$$t_{acc} = \frac{M_{core}}{\dot{M}} \tag{1.10}$$

where $\dot{M} = dM/dt$ is the accretion rate. If $t_{KH} > t_{acc}$, the evolution of the protostar is adiabatic and accretion shocks become the main source of emission. It should be kept in mind that we have been neglecting the external pressure from the surrounding matter in the cloud. Although not a part of the collapsing process, this material is available during the accretion stage. We used typical values for low-mass stars ($M \leq 2\ M_\odot$; Schulz 2005) to estimate the times of the free-fall and Kelvin-Helmholtz stages. These stars will finish their accretion phase before reaching the main sequence, and will need to contract further until they are able to start burning hydrogen in their cores. Because they have depleted their envelope they become visible, and until they reach maturity they are denominated *pre-main sequence* (PMS) stars. With respect to their lifetime, Haisch et al. (2001) estimated that accretion disks around low-mass stars survive up until $\sim$ 6 Myr. More massive stars, on the other hand, will reach their main sequence stage while still

undergoing accretion. Accretion disks around massive stars are dispersed by the strong winds emitted from these stars. In fact, these winds are destructive enough to evaporate material still present in their envelope, as well as to dismantle nearby star-disk systems. Although the *young stellar object* (YSO) nomenclature is often used to describe any star system throughout all its evolutionary stages, it is especially used for these massive systems where evolutionary stages overlap. We want to highlight that after the end of the accretion phase matter can still be flowing into the YSO. The end of the accretion phase is rather defined as the point when the accretion disk is no longer predominantly fed by the envelope. The *zero-age main sequence* (ZAMS) of a star signifies the end of its PMS evolution and the time at which the star reaches its main sequence stage, thus ceasing from contracting further. Physically, it can be described as the first moment in the life of the star when the energy it produces from nuclear reactions in its core fully evens out the energy that is radiated from its photosphere.

Deuterium Burning

Once low-mass protostars ($M \leq 1\ M_{\odot}$; Schulz 2005) reach a temperature at their center $T > 10^6$, they start burning deuterium. Here, the accretion rate is correlated to the duration of the burning phase with rapid-declining accretion rates corresponding to shorter times for deuterium burning. This means that low-mass protostars burn as much deuterium as it is fed from the outer envelope. The luminosity of the protostar is then related to its mass accretion rate by (Schulz, 2005):

$$L_{D_0} \simeq 12 L_{\odot} \left(\frac{\dot{M}_{acc}}{10^{-5} M_{\odot} \mathrm{yr}^{-1}}\right) \tag{1.11}$$

where L_{D_0} is the luminosity from deuterium burning and $L_{\odot}$ is the luminosity of the Sun. Since the amount of deuterium burn is of the same magnitude as the accreted deuterium, the luminosity produced by this reaction is proportional to the total gravitational binding energy of the protostar. As such, deuterium burning constrains the mass-radius relation of low-mass YSOs, but only for a narrow accretion range since, realistically, more deuterium is consumed than accreted in these protostars. A more general equation is (Palla et al., 2002; Schulz, 2005):

$$L_D = L_{D_0} \left(1 - \frac{\mathrm{d}(f_D M)}{\mathrm{d}M}\right) \tag{1.12}$$

where f_D is the fractional deuterium concentration. For more massive stars ($M > 2\ M_{\odot}$; Schulz 2005), deuterium burning continues even after it is depleted in the core of the YSO through a shell-type burning (Palla and Stahler, 1990).

Lithium Burning

Lithium is $\sim 7 \times 10^{-7}$ times less abundant than deuterium (Schulz, 2005). As such, its contribution to the overall energetic balance of the protostar is negligible. Still, the detection of this element in YSOs allow us to probe their internal structure and evolutionary stage (Ventura et al., 1998). Temperatures at the center of the YSO must be $T > 2.5 \times 10^6$ K (Bodenheimer, 1965) to be able to burn lithium, which corresponds to a mass $M \sim 0.06\ M_{\odot}$ (Schulz, 2005). For higher-Z elements, temperatures inside the star must reach $T > 15 \times 10^6$ K in order to sustain a CNO cycle (Schulz, 2005).

1.2 Star-forming Regions

When a molecular cloud becomes massive enough or is subject to external forces that initiate cloud fragmentation and collapse, it becomes an SFR. SFRs are the stage for a variety of physical processes, whether between their members, or due to a number of interactions with the interstellar medium surrounding them, resulting in emissions that range throughout the entire electromagnetic spectrum. As mentioned in Section 1.1, star-forming clouds collapse into multiple cores - meaning stellar formation occurs in clusters. For example, the Orion A and B clouds are divided into several centralized clusters like NGCs 2023, 2024 (Depoy et al., 1990; Schulz et al., 1991) and the Orion Nebulae Cluster. SFRs are then crucial for our understanding of early stellar evolution since in no other place in the Universe can we find such a dense sample of stars still in the early stages of their lives.

For very young clusters in SFRs, observations are usually made at the near-IR (NIR) and mid-IR range, since optical emission from the young objects embedded in the star-forming clouds will be absorbed by the envolving gas and dust. But some observations are also made at the sub-mm, X-ray and optical wavelengths. The constituents of these clusters usually cover the entire stellar mass regime, with lower-mass objects outnumbering more massive ones (Lada and Lada, 2003). Because members of SFRs are at virtually the same distance from us, we can build Hertzsprung-Russell Diagrams (HRDs) of these SFRs. These diagrams relate the luminosity of the sources to their respective effective temperature. Figure 1.1 shows one such HRD from Bayo et al. (2011) where a compilation of spectroscopically confirmed members (black and red dots) of the Collinder 69 cluster at the Lambda Orionis SFR is plotted. Red dots indicate sources which display accretion and open circles flag sources which show IR excess during observations. During their evolution, stars follow specific paths in an HRD. These paths tread through zones of instability in HRDs which allows astronomers to constrain the evolution of protostars (Gaustad, 1963; Gould, 1964). As such, evolutionary tracks can be drawn in an HRD for specific stellar masses - these are called the *Hayashi tracks* (dashed lines). Although in reality these are not true evolutionary paths, they constitute asymptotes for the instability regions in an HRD. The starting point of these tracks is during the Kelvin-Helmholtz timescale of a protostar. As it was already mentioned, massive stars can still be accreting when they reach their ZAMS, as they show very short contraction timescales towards their ZAMS (Palla and Stahler, 1990; Palla et al., 2002). Iben (1965) calculated a timescale on the Hayashi tracks of ~ 100 Myr for very-low-mass stars and of a few hundred years for stars $M > 10\ M_{\odot}$.

When observing SFRs, Colour-Magnitude Diagrams (CMDs) can be used as a proxy for the canonical HRDs. Young objects are redder since they are still on the Hayashi tracks. On a CMD, these sources are then further to the right than field objects. As such, by plotting the CMD of a dataset, we are able to discriminate which sources present photometry indicative of youth and/or membership. Another important concept of HRDs and CMDs are isochrones. These are evolutionary tracks for different masses with the same age (solid lines). Isochrones are very useful when performing studies of SFRs since their age is fairly constrained and their members were born at approximately the same time. This allows astronomers to estimate the mass of members of these SFRs from their photometry. Studies of SFRs then provide knowledge about an evolution stage across a range of masses. Still, background sources also reddened by the intervening cloud constitute contaminants on the redder subset of a CMD, and complementary methods to CMD-selection are required to assert the cloud membership of the observed sources.

The reddening is not uniform across these regions, so correcting for it is no simple task as well. Fortunately, we are able to take advantage of another property of these clusters. Because they are born from the same cloud, they adopt its peculiar velocity. Then, we can identify new members of an SFR by comparing their kinematic properties with those of known members of the region.

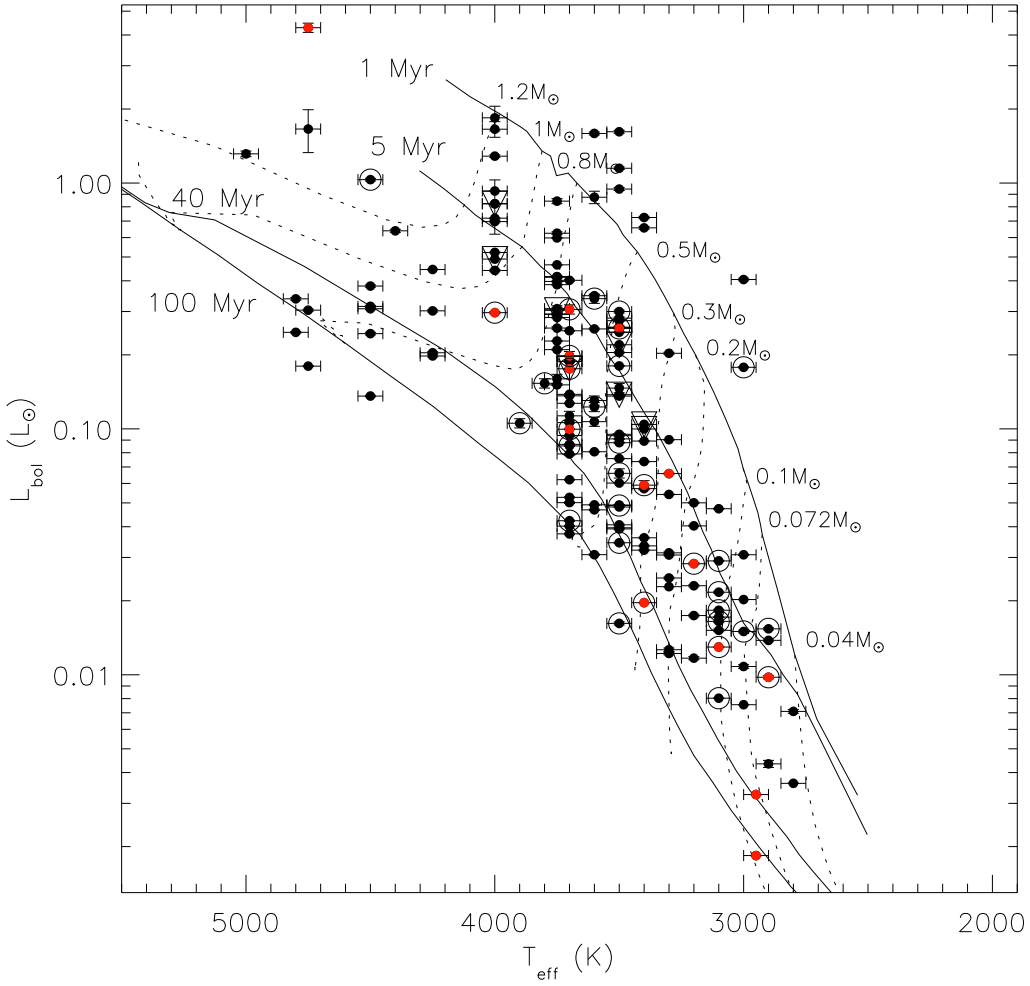

Figure 1.1: *A compilation of spectroscopically confirmed members of the Collinder 69 cluster at the Lambda Orionis SFR produced by Bayo et al. (2011). Dashed lines represent the Hayashi tracks for a given mass and solid lines are isochrones. Red dots constitute active accretors and open circles flag objects with bright IR emission.*

1.3 The Initial Mass Function

One of the questions astronomers pose when deliberating about stellar clusters is what factor is responsible for the total mass of a cluster. When performing studies of these clusters, a universal IMF is often used to make estimations of the total mass. The IMF is one of the most important constraints in star-formation theory and is based on the empirical luminosity functions of stellar clusters. Salpeter (1955) noticed that the relation between the luminosity function of an observed sample of main sequence stars with its mass function is smooth and leads to the conclusion that each luminosity function has its own respective mass function. Defining the luminosity (L) function as (Schulz, 2005; Lada and Lada, 2003):

$$f(L) = \frac{dN}{dm} \tag{1.13}$$

where N is the number of stars with magnitude m, and the mass function g(M):

$$g(M) = \frac{dN}{d\left(log_{10}\left(M\right)\right)} \tag{1.14}$$

where N is the number of stars with mass M, a relation between the two can then be derived if we make the substitution $dN = g(M)d\left(log_{10}\left(M\right)\right)$:

$$f(L) = \frac{dlog_{10}\left(M\right)}{dm} \times g(M) \tag{1.15}$$

The IMF is a probability density function stating the number N of stars in a cluster with masses between $M \pm \Delta M$. Salpeter (1955) derived an expression for the IMF:

$$N\Delta M = N_0 \left(\frac{M}{M_\odot}\right)^{-\alpha} \left(\frac{\Delta M}{M_\odot}\right) \tag{1.16}$$

with $\alpha = 2.35$. But, at the time, observations were only sensitive to massive stars. More recently, the IMF is often defined by a series of power-laws. An example is Kroupa (2001), which ramified the values for α: 1) $\alpha = 0.3$ for $M < 0.08\ M_\odot$; 2) $\alpha = 1.3$ for $0.08\ M_\odot < M < 0.5\ M_\odot$; 3) $\alpha = 2.3$ for $M > 0.5\ M_\odot$. Chabrier (2003) also presented a log-normal form:

$$N = 0.158 \left(\frac{1}{ln\left(10\right) M}\right) e^{-(log(M)-log(0.08))^2/\left(2\times 0.69^2\right)} \text{ , for } M < M_\odot \tag{1.17}$$

$$N \propto m^{-\alpha} \text{ , for } M > M_\odot \text{ with } \alpha = 2.3 \pm 0.3 \tag{1.18}$$

for individual stars, and:

$$N = 0.086 \left(\frac{1}{ln\left(10\right) M}\right) e^{-(log(M)-log(0.22))^2/\left(2\times 0.57^2\right)} \text{ , for } M < M_\odot \tag{1.19}$$

$$N \propto m^{-\alpha} \text{ , for } M > M_\odot \text{ with } \alpha = 2.3 \pm 0.3 \tag{1.20}$$

for stellar systems.

There are still important questions not yet answered about the IMF such as its universality (whether the IMF is the same for every SFR in the Universe) and whether it is continuous across mass ranges. Massive stars contribute to much of the uncertainty in the modelling of the IMF because of their short lifespans. In Fig. 1.2, we show a collection of IMFs produced from observations of several SFRs (Bastian et al., 2010). A tapered power-law was fit to the observations. For higher masses, the slope of the fit remains approximately the same throughout the different regions. There is a peak in the IMF at lower masses and, from here, the slopes vary across the sample. The different slopes are a consequence of the incompleteness at the low-mass regime. Reddening effects make it difficult to assess the membership of detected low-mass objects, and a better characterization of the IMF demands the exercise of deep photometry paired with follow-up spectroscopy efforts and/or kinematics of these regions. Only then will we have a robust representation of the low-mass regime of the IMF from which we will be able to discuss its universality. In this respect, BDs play a pivotal role as they populate the substellar range of the IMF. Detection and membership assessment of BDs are then crucial to constrain the lower mass end of the IMF.

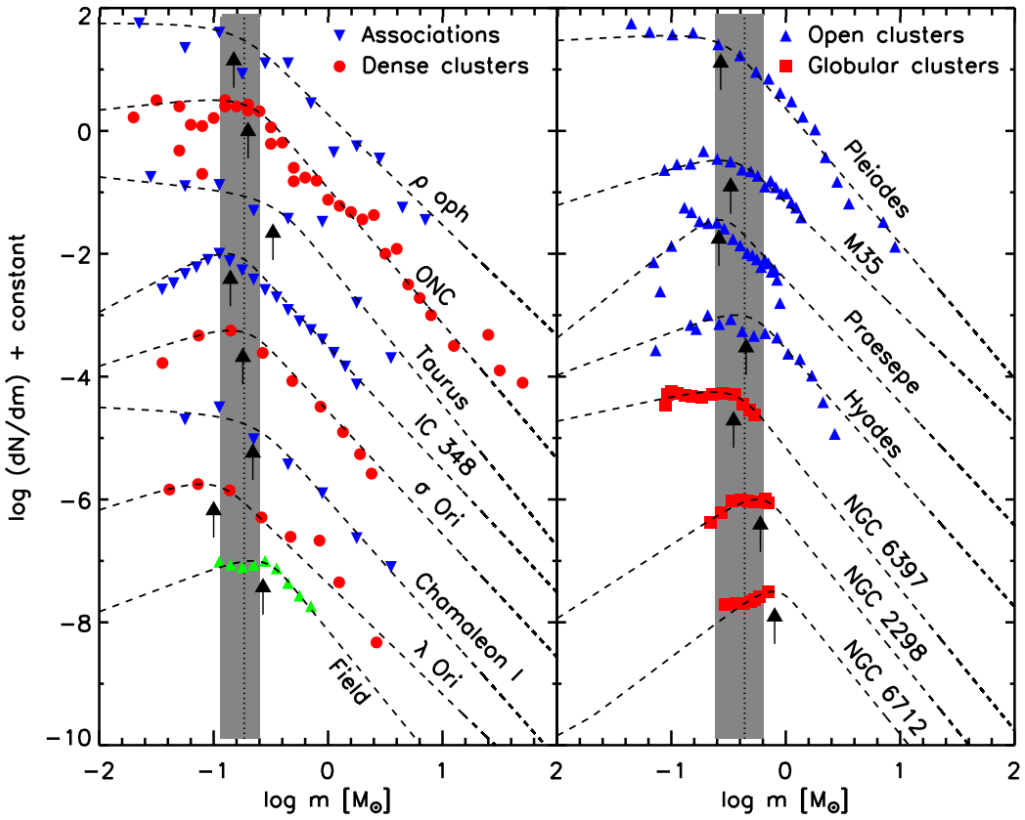

Figure 1.2: *The mass functions of a collection of SFRs, open clusters and globular clusters from De Marchi et al. (2010). Dashed lines represent a "tapered power-law" fit to the data, and the arrows indicate the characteristic mass of each sample. The vertical dashed line is the mean of all characteristic masses and the grey region is the standard deviation of this mean (excluding the field sample). All mass functions seem to agree with the existence of a universal IMF, although the lower-mass end needs to be further constrained to affirm this.*

1.4 The SONYC Survey

The SONYC survey is one of the many efforts being made to detect and characterize low-mass objects, particularly young ones. The main goal of SONYC is to construct a comprehensive, unbiased census of substellar objects in the surrounding SFRs. This survey is performed using deep optical and NIR wide-field imaging along with other publicly available catalogs, combined with proper motions (PMs) when available, to determine substellar candidates for comprehensive follow-up spectroscopy campaigns with the Subaru telescope and the VLT. Candidates are selected using optical and NIR photometry, with observations reaching masses below $0.1 M_{\odot}$, the lowest mass example being a cool $\sim$ L3-type BD with an estimated mass $M \sim 6$ M_J. SONYC has obtained more than 700 spectra of candidate objects and confirmed around 100 of these sources as BDs. The survey has conducted these studies for five different regions so far: NGC1333 (Scholz et al., 2012a), ρ Ophiuchius (Geers et al., 2011; Mužić et al., 2012), Chamaeleon-I (Mužić et al., 2011), Upper Sco (Scholz et al., 2011), and Lupus-3 (Mužić et al., 2014, 2015). It has determined a star-to-BD ratio in our galaxy of $2-5$ and an IMF:

$$\frac{dN}{dM} \propto M^{-\alpha} \text{ with } \alpha = 0.5 - 1 \tag{1.21}$$

This is in agreement with surveys in IC348 (Alves de Oliveira et al., 2013), σ-Orionis (Peña Ramírez et al., 2012), ρ Ophiuchius (Alves de Oliveira et al., 2012) and λ-Orionis (Bayo et al.,

2011). In Figure 1.3, the star-to-BD ratio in the clusters studied by the SONYC survey is matched against the stellar surface density of the respective cluster (as taken from Mužić et al. 2019). Although the stellar density increases by order of magnitudes, the star-to-BD ratio remains relatively the same, unlike the scenario predicted by Bonnell et al. (2008). The star-to-BD ratio also seems to be independent of the presence of OB-type stars.

Deep surveys of star-forming complexes are crucial for our understanding of star- and planet-formation and early evolution, since they provide a compact, homogeneous sample riddled with objects of interest (a requirement to study disks, accretion and multiplicity). They also supply important data to determine the full shape of the IMF of these regions, as these surveys are able to detect sources in the low-mass regime of the IMF which are very faint.

When identifying low-mass objects in SFRs, one should look for sources with PMs and positions in the CMDs on par with their respective cloud (these methods are explained later in Chapter 4). For candidate selection, it is best to cross-match the data from a survey against existing publicly available catalogs of that region, which provides astronomers with multi-band information on the observed sources. When this is not available, theoretical models estimating the temperature and luminosity of these objects should be converted to colour-magnitudes using the respective relations. This provides photometry measurements for the dataset which can be used to narrow down the sources in the survey to those we are interested in (in the case of this thesis, young, low-mass BDs). By identifying and studying young BDs, astronomers acquire information about the formation processes of both planets and stars. The next step for the SONYC survey, and the body of this work, refers to the CrA SFR.

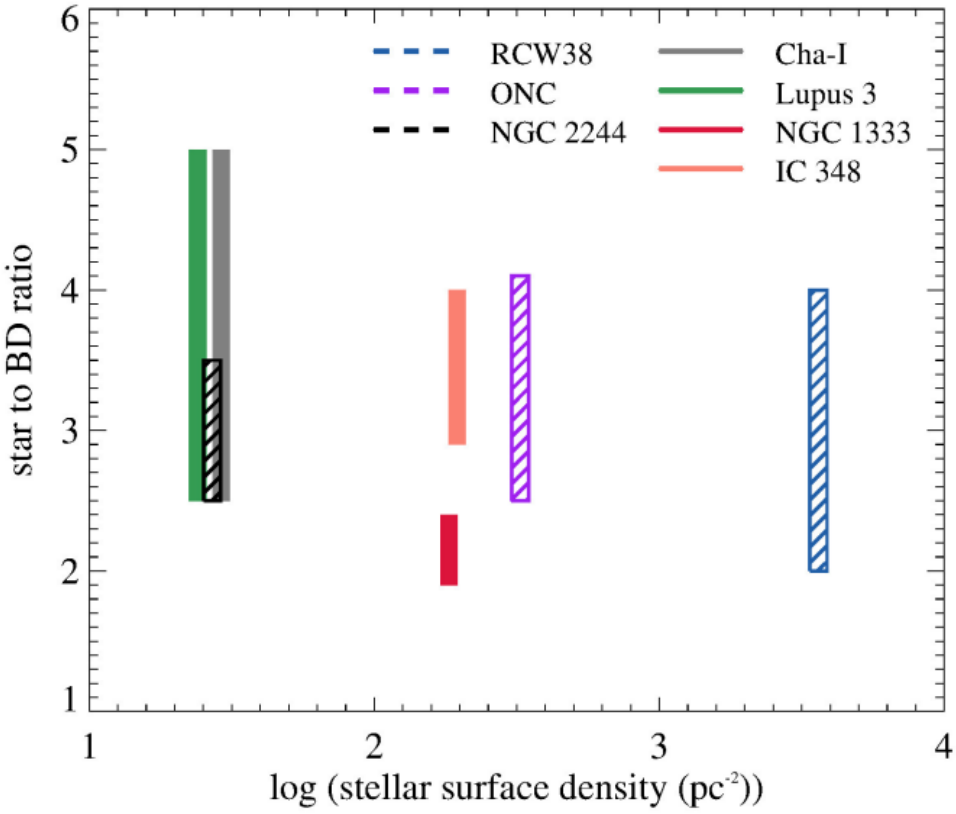

Figure 1.3: *The relation between star-to-BD ratio with cluster surface density. The height of each polygon indicates the 1-σ deviation or the range in star-to-BD ratio in the case of Cha-I and Lupus 3. Filled polygons are regions with few or no massive stars. Dashed polygons represent regions with a substantial OB-star population. Credit: Mužić et al. (2019).*

1.5 Brown Dwarfs

BDs are substellar mass star-like objects. They did not accrete enough matter during their formation process which would make them capable of burning hydrogen. As such, they are devoid of a central energy source with pressure support against gravity being provided by electron degeneracy, and they possess short luminous lifetimes (Kumar, 1963). This does not mean that they are not able of burning other elements with lower combustion temperatures, and some BDs partake in deuterium-burning (10^6 K) and/or lithium-burning (2.5 x 10^6 K). They are then distinguished from other objects by their mass, although mass cannot be directly determined from observations and is rather inferred from matching secondary indicators (i.e. temperature or luminosity) against theoretical models. The definition for the upper mass-limit for BDs is usually considered by astronomers to be around the mass-threshold for hydrogen-burning - around 75 Jupiter masses (M_J). After formation, BDs rapidly cool to $\sim 2\,500$ K (Reid and Hawley, 2005), so the first surveys of these objects consisted of searching for extremely red objects using broadband photometry. But, for very low-mass BDs (i.e. T $\lesssim 1\,300$ K), methane absorption actually leads to bluer colours in the NIR (Tsuji, 1964). This lead to a miscategorization of BDs during early NIR surveys. There is also the matter between distinguishing very low-mass BDs from high-mass planets. The lower mass-limit for BDs can be loosely defined as the mass threshold for deuterium-burning ($\sim$ 0.013 $M_\odot$ or $\sim$ 14 M_J at solar abundance; Burrows et al. 1997), with any lower mass bodies being classified as planets (assuming these are orbiting a parent star). This definition would also match the one for the upper mass limit at the stellar/BD boundary. Deuterium is very hard to detect at such low temperatures (Reid and Hawley, 2005), and this division is hard to apply in a practical sense. Also, surveys in young SFRs and clusters reported free-floating objects with 5 - 10 M_J (Scholz et al., 2012b; Mužić et al., 2015; Peña Ramírez et al., 2012; Alves de Oliveira et al., 2013) and these objects cannot be categorized as planets since they are not orbiting a parent star (a necessary requirement to be classified as a planet). This should highlight how little we still know about the low-mass regime, which will have ramifications in the constraints of the IMF and, as such, makes the subject of studying BDs a very requisited one. No more so because, since BDs are in mass-regimes between those of stars and planets, their formation processes also provide a bridge for understanding the formation processes of both these types of objects. There are four widely regarded theories for the formation of BDs:

1) Turbulent fragmentation (Padoan and Nordlund, 2004; Hennebelle and Chabrier, 2009a): BDs form from the fragmentation and gravitational collapse of a cloud, but the molecular core from which they originate is not massive enough to sustain the development of a star. Standard fragmentation is unlikely to produce BDs since the initial cloud would need to be small to form a BD. From the Jeans mass relation, this means it would need to have a very high density in order to become unstable and collapse. Fragmentation becomes more practical if turbulence is inserted into this scenario, where the flow of material can generate high density clumps in the cloud which collapse to form BDs;

2) The disk surrounding a protostar may fragment into multiple low-mass objects, from low-mass H-burning stars to BDs and planetary-mass objects (Stamatellos et al., 2007; Goodwin et al., 2004). These low-mass companions can then be ejected from the system due to interactions between themselves. Because BDs ejected this way are expected to have low velocity dispersion values they are able to retain disks, sustaining accretion even after ejection. BD-binaries formed in the stellar disk are also able to survive when they are released onto the field;

3) The embryo ejection hypothesis considers that some of the cloud cores, instead of collapsing into a singular object, collapse into 2 to 4 different objects (fragmentation during rotation) which compete for the accretion of the environment matter (Schulz, 2005). Since gravity will favour more massive initial perturbations in the cloud these will grow more rapidly, with the bodies closer to the center of mass of a multiple system being favoured for accretion. Since these objects are close enough between one another, due to dynamical interactions between each of these objects, it is possible that the lowest mass object is ejected from the group. If such an object would have a mass lower than the hydrogen-burning limit (~ 75 M_{Jup}), and since far from the dense core it would not be able to gain any more matter, it would become a free-floating BD;

4) Photoevaporation (Whitworth and Zinnecker, 2004): During the accretion phase of a protostar, the envelope feeding the system may be partially or completely blown away by the stellar winds of a nearby massive star, hampering the development of the object so that a BD will remain as the end result.

There are still questions regarding the formation of BDs which have not been answered yet, such as: 1) What is the ratio of objects below the deuterium-burning mass limit with respect to BDs and stars? 2) Although we have not yet observed major differences between different environments, how do the initial conditions of a molecular cloud influence the number of BDs produced? 3) Is there a dominant BD-formation scenario in comparison to others?

More massive BDs tend to form like stars do, while lower mass ones do not show a discernible process from those of giant planets (Chabrier et al., 2014). In Luhman (2012), they concluded that turbulent fragmentation is the mechanism responsible for a considerable fraction of BDs in low-density regions like the Taurus SFR. In a more general sense, Thies and Kroupa (2007) argue that both the turbulent fragmentation and disk fragmentation hypothesis are responsible for the majority of observed BDs. Scholz et al. (2013) used the findings from SONYC surveys on the NGC1333 and IC348 clusters to constrain BD-formation theories for which stellar density is a critical parameter (i.e. Bate 2012 which follows the embryo ejection hypothesis). They found a star/BD ratio (> 2.6, > 4.1) and median mass values (0.21, 0.24 $M_{\odot}$) comparable with theoretical predictions, although they argue that the influence of object density is difficult to ascertain since theoretical simulations were made for a limited set of initial conditions. They then compare with predictions from the scenario conjectured by Bonnell et al. (2008) which admits a turbulent fragmentation mechanism for BD formation. Here, they find that the denser NGC1333 cluster has a higher fraction of very low mass stars and BDs, as predicted by Bonnell et al. (2008). Still, they mention their observed values are higher than those predicted when admitting solely a turbulent fragmentation scenario, with an interplay between this mechanism, disk fragmentation and embryo ejection providing a possible answer for the excess low mass objects. When comparing with the turbulent fragmentation model from Padoan and Nordlund (2002) and the gravoturbulent scenario of Hennebelle and Chabrier (2009b), they found that the expected influence of stellar density is much greater than what was observed. However, Scholz et al. (2013) comment that other cluster parameters (i.e. the Mach number) can explain this difference and that, being so heavily dependent on initial conditions, these models are difficult to test from empirical IMFs.

With so much still to learn about BDs, it is then imperative to look for BDs in SFRs where they are still forming or at early evolutionary stages. Due to their size, BDs are also particularly faint sources without even taking into account extinction factors. For these reasons, nearby SFRs such as CrA pose a prime study candidate to achieve this since astronomers are able to conduct

deep surveys of these regions.

1.5.1 Spectral Features of Brown Dwarfs

As they grow older, the luminosity and colours of BDs change Burrows et al. (2001). Figure 1.4 shows how the luminosity of Solar-metallicity objects evolves with age. It shows this evolution for masses ranging from 0.3 M_J to 0.2 $M_\odot$. Red lines correspond to objects below 13 M_J, green lines to objects with masses above 13 M_J and below the main sequence, and blue lines are main sequence objects. Brown dots and pink dots indicate when deuterium and lithium reserves have been depleted, respectively. This means that only the most massive BDs are capable of burning lithium in their core, while most BDs possess a lithium-rich atmosphere. Only at ages > 1 Gyr do main sequence stars and BDs deviate significantly from each other. Then, unlike stars which plateau once they reach a stage of equilibrium, BDs cannot burn hydrogen to counteract the energy lost when emitting. Because of this, their brightness diminishes over time. When young, BDs can have temperatures akin to those of an M-dwarf, transitioning, as they evolve, to later types (i.e. T-type). The luminosity of BDs in different bands also changes with age along with prominent spectral features in these bands. Because of this, spectral absorption lines, particularly in the NIR, provide age constrains for an observed BD. The spectra of BDs present numerous features which depend on the age, effective temperature, spectral type and surface gravity. Figure 1.5 (taken from Mužić et al. 2015) shows the H + K ($\sim$ 1.3–1.9 μm + $\sim$ 1.8–2.6 μm) spectra of two different BDs in the Lupus-3 SFR (SONYC-Lup3-28 and SONYC-Lup3-29) and of one BD (SONYC-ChaI-1) in the Chameleon I region. In the NIR, young sources with spectral type M5 or later show a triangular peak in the H-band (delimited by two vertical dark red lines) due to water absorption in their atmospheres (Lucas et al., 2001; Cushing et al., 2005). This feature is strongly dependent on the effective temperature of the source, with cooler objects presenting a deeper peak than warmer ones, meaning it is stronger for later (i.e. older) sources (Burrows et al., 2001). Also, the shape of this feature is surface gravity-dependent (Almendros-Abad et al., 2021). Higher gravity sources show a round peak unlike the triangular shape of low-to-intermediate gravity objects. In the K-band, CO absorption bands (flagged) help differentiate dwarf objects from K- and M-type giants, since the latter are expected to show deeper CO absorption (e.g. Rayner et al. 2009). H_2 emission lines can also be seen in the K-band (Mužić et al., 2015). These lines can be associated with accretion which is an indicator for youth. Although not seen here, the appearance of methane bands in the K-band suggests a transitioning state in the L/T-type regime, since older BDs are expected to show methane absorption bands in place of CO bands (Burrows et al., 2001). Observing candidate sources in the H + K bands is then a great choice when looking for young BDs.

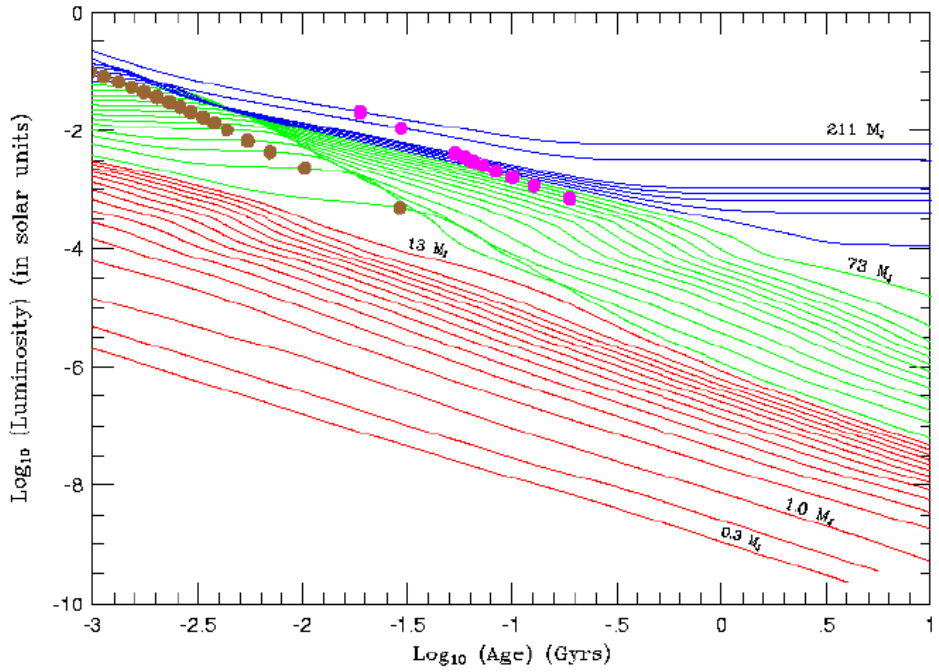

Figure 1.4: *The evolution of luminosity with age for objects ranging 0.3 M_J − 0.2 $M_\odot$. Blue lines represent main sequence objects, while green lines are objects below the main sequence and above 13 M_J and red lines are below this limit. Brown dots indicate the stage at which deuterium reserves are depleted, while pink ones refer to the depletion of lithium reserves.*

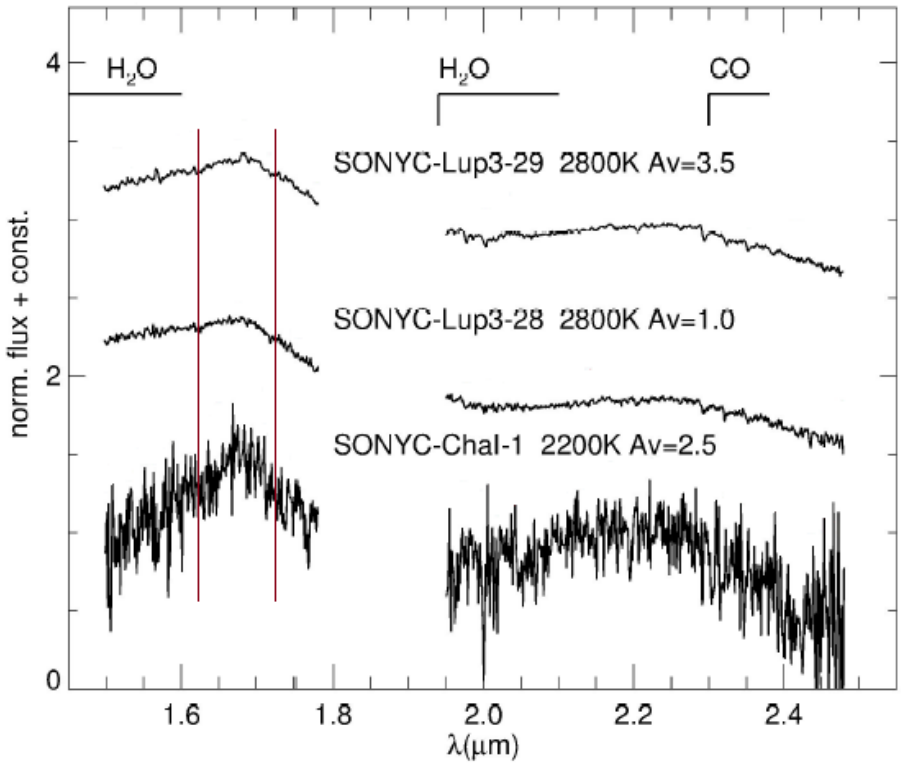

Figure 1.5: *Spectra of two confirmed BD members of Lupus 3 and one BD member of Chamaeleon-I (black). Offsets were introduced to each spectra for visibility. The 1.8 − 1.95 μm region is absorbed by our atmosphere and was omitted for clarity. The prominent molecular absorption bands (H_2O and CO) are flagged.*

1.6 Corona Australis

CrA is an SFR in the constellation of the same name. It is one of the closest SFR to the Solar System at an estimated distance of 150 parsecs (Galli et al., 2020), allowing it to be probed deeply with a large telescope in search for low-mass objects since it is close enough for these faint sources to be detected. It is near the Gould Belt complex - an association of stars and molecular clouds situated within $\sim$ 20 degrees of the Galactic Plane (Herschel 1847, Gould 1879) - but, with a declination of $\sim -$ 40 degrees, it falls outside of the region of this structure. CrA has an estimated mass of 7000 $M_{\odot}$ (Cappa de Nicolau and Poppel, 1991), with a mean extinction of $A_V \sim 5$ mag reaching a maximum of $A_V \sim 30$ mag (as measured by Peterson et al. 2011 using *SPITZER* data) in the *Coronet Cluster* - a small open cluster isolated at the edge of the Gould Belt with its center mostly composed of young stars (Vrba et al. 1976, Knacke et al. 1973, Brown and Zuckerman 1975, Forbrich et al. 2007, Garmire and Garmire 2003, Schöier et al. 2006, Henning et al. 1994 are a number of works reporting observations of the CrA region in different bands). It also has many members starting at late-B spectral types (Neuhäuser and Forbrich, 2008). The CrA region has been mostly surveyed in the IR, X-Ray and mm-continuum bands with follow-up spectroscopy from centimeter-radio to X-Ray bands being focused on the Coronet protostar cluster. The main subject of observations in this region is the R CrA star - the brightest star in this cluster - as well as its population. IR observations were made by many groups (Glass and Penston 1975; Vrba et al. (1976); Taylor and Storey 1984; Wilking et al. 1986), as well as H_{α} observations (Marraco and Rydgren, 1981) and emission-line observations (Graham, 1993). These were followed by early X-ray (Walter 1986; Koyama et al. 1996; Neuhaeuser and Preibisch 1997; Walter et al. 1997; Patten 1998), radio (Brown 1987; Cappa de Nicolau and Poppel 1991), millimeter (Harju et al., 1993), and far-IR studies (Wilking et al. 1992).

Regarding the age of CrA, different works have determined different values for this parameter. Knacke et al. (1973) derived an age of $\sim$ 1 Myr for a group of variable stars near R CrA. Wilking et al. (1997) assumed an age of 3 Myrs to estimate the number of low-mass members of the molecular core around R CrA. James et al. (2006) determined an age of 9 ± 4 Myr for a sample of targets in the CrA cloud. Nisini et al. (2005) derived from low- and moderate-resolution spectra of embedded YSOs in CrA ages ranging 10^5 – 10^6 Myr with the youngest YSO (IRS 1) showing an age of $\sim$ 0.1 Myr. In Sicilia-Aguilar et al. (2008), they used an age of 1 Myr citing the work of Nisini et al. (2005), and arguing that it is more congruent with the the presence of material and Class 0 objects (Chen et al., 1997). In this work, we use an age of 3 Myr when using models for our selection process, mimicking Wilking et al. (1997) who also performed a photometric study of the region, and to take into account the high dispersion of reported ages for the CrA SFR.

In Figure 1.6, the CrA cloud is shown highlighting the sky positions of its oldest known members, plus the stars HR 7169/70. R CrA and TY CrA are the brightest stars in the complex. R CrA is an A5-type star while TY CrA is a primary B8-B9-type star (Herbig and Kameswara Rao 1972, Knacke et al. 1973, Marraco and Rydgren 1981) in a, at least, quadruple system (Casey et al. 1995, Chauvin et al. 2003) at $\sim 5'$ northwest of R CrA. HD 176386 is $1'$ south of TY CrA (Knacke et al. 1973, Marraco and Rydgren 1981). It was discovered by Wilking et al. (1997) to be a binary system with spectral types A0V and K7, and a 3.”7 separation (Meyer and Wilking, 2009). S CrA is a binary with spectral type K6 (Neuhäuser and Forbrich, 2008). DG CrA, T CrA and VV CrA are, respectively, K0-, F0e- and K1-type stars (Neuhäuser and Forbrich, 2008).

HR 7169 and HR 7170 are two B8V stars outside the Coronet Cluster (around ∼12′ southwest from R CrA), but they are expected to be associated with the star-forming complex since Loren (1979) observed evidence of possible heating of the cloud by these two stars, indicating these may belong to the cloud complex.

The Coronet Cluster

The *Coronet Cluster* is a cluster of embedded sources to the west of the CrA cloud first discovered by Taylor and Storey (1984). The Coronet Cluster presents the highest extinction in the entire CrA SFR with an $A_V \sim 30$ mag (Peterson et al., 2011). From far-IR studies done in Wilking et al. (1985), and using mid-IR photometry, Wilking et al. (1986) found 13 sources in the Coronet Cluster at different evolutionary stages. In Sicilia-Aguilar et al. (2008, 2011), they performed optical spectroscopy of objects in the Coronet Cluster confirming 18 members. When compiling a list of 116 candidate YSOs in the CrA cloud, Peterson et al. (2011) noted that 68 of their YSO candidates are located in the Coronet Cluster, citing it as the dominant cluster in the whole CrA cloud complex. They also observed a radial spread of sources centered at the Coronet Cluster, with younger objects populating the center while older sources are dispersed throughout the surrounding field. One of the brightest stars in the CrA SFR, R CrA is at the center of the Coronet Cluster and, as such, this region is also referred to in some papers as the *R CrA Cluster*.

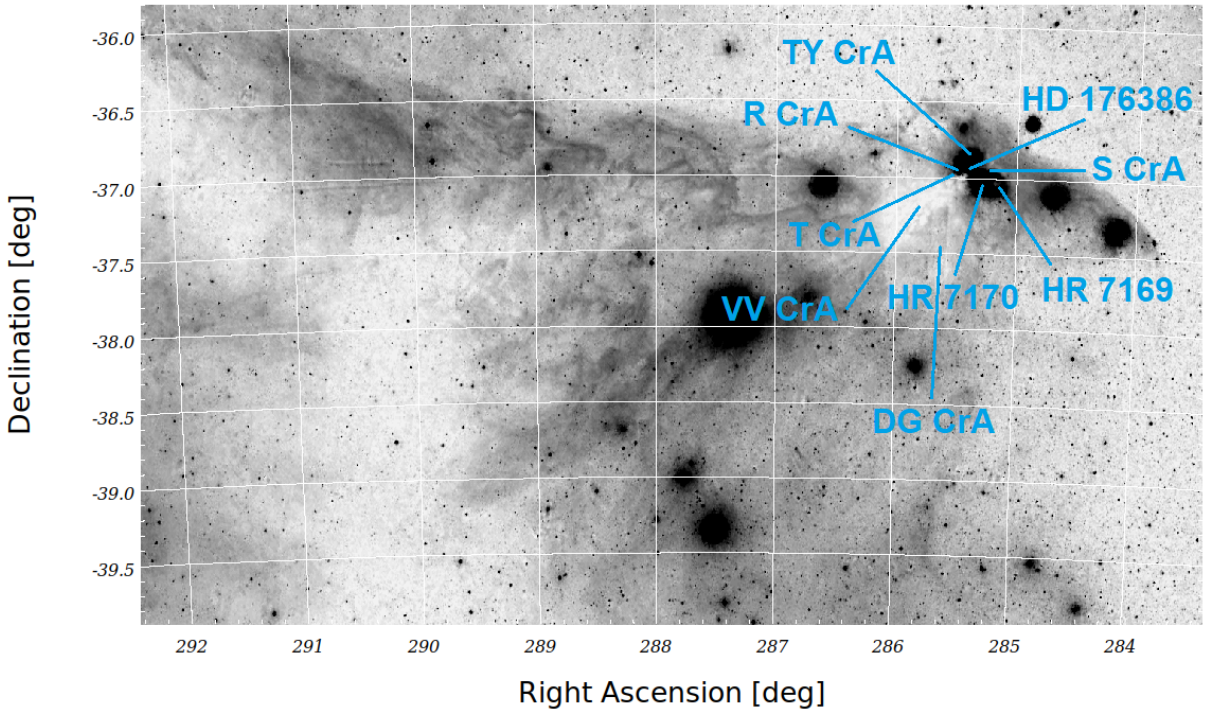

Figure 1.6: *CrA in its full length. At the northwest part of the region, a dark molecular cloud with many embedded reflection nebulae is expected to be a nest for the birth and development of new stars. It is also here that the majority of the members of the cloud can be found. Image taken using the* Aladdin *software (Bonnarel et al., 2000).*

Chapter 2

Datasets

In this chapter, we describe all the different datasets (both catalogs and compilations) produced during this thesis, as well as those taken from the literature which were used for calibration, candidate selection and comparison to our results.

The work of this thesis revolves around observations made of the CrA cloud by Bo Reipurth and his team in 2017. We want to stress that these observations were not made by our group, nor were they intended for the work we present here. We merely saw an opportunity for improving our knowledge of the substellar regime of CrA which these observations provided, and we express our full appreciation to the people involved in the collection of these observations. These observations were made using the Suprime-Cam instrument present at the Subaru telescope (Section 3.1), and we retrieved this dataset from the SMOKA (Enoki et al. 2007) system (the data archive of the National Astronomical Observatory of Japan).

The CrA region was observed through the nights of 24th - 28th of May in 2017 with an image quality of 0.7 arc-seconds on average. Our dataset contains images taken using two filters: one narrow-band H_α filter (N-A-L656) and one broad-band filter covering the optical I-band (W-S-I+; details are given in Table 2.1). Photometry calibration was performed on the latter to ascertain probable low-mass members of the SFR. This was done by calibrating the data against the DENIS catalog (Epchtein et al., 1999), since it has a filter response curve for the I-band similar to that of the W-S-I+ filter. The I-band corresponds to the reddest region of the optical, allowing the detection of very faint and/or embedded sources in the observed field. The narrow-band filter - N-A-L656 - is a custom-made filter with an effective width $W_{eff} = 143.91$ (Rodrigo et al., 2012), and it was used to measure the H_α emission from the sources in the CrA region. Strong H_α emission is a signature for accretion which, in turn, implies the presence of a circumstellar disk at the observed source. This helps consolidate the case that an object is a probable members of a young SFR such as CrA, since young objects are expected to show strong H_α emission (Luhman et al., 2005; White and Basri, 2003; Muzerolle et al., 2000a,b, 2003; Jayawardhana et al., 2002, 2003; Whelan et al., 2005; Joy, 1945). Other important data assets to this work were the numerous publicly available catalogs, which are discussed more in-depth in Section 2.1. These are:

- *Gaia* (Gaia Collaboration et al., 2018, 2021);
- DANCe (Galli et al., 2020);
- DENIS (Epchtein et al., 1999);

- VHS (McMahon et al., 2013);
- USNO-B1 (Monet et al., 2003);

Table 2.1: *The bands used during the Suprime-Cam exposures and the DENIS I-band to which the W-S-I+ filter was calibrated to.*

Filter	Type	λ_{min} (nm)	Peak (nm)	λ_{max} (nm)	Features
N-A-L656	Narrow-band	641.722	656.681	672.071	H_α
W-S-I+	Broad-band	672.082	763.5	865.545	Optical I-band
DENIS I-band	Broad-band	700.728	789.712	914.000	Optical I-band

2.1 Catalogs of Corona Australis

To help with candidate selection for follow-up spectroscopy, a number of other publicly available catalogs were used during the work of this thesis. These catalogs complement the dataset produced during the Suprime-Cam observations, providing the photometric calibration, colours and kinematic information of the observed sources. A catalog of the spectroscopically confirmed members of CrA was also built during this thesis. This compilation of sources helped characterize the CrA SFR, which is crucial when selecting sources for our final list of candidates. In this section, we give an overview of these catalogs explaining how they were produced and in which way they contributed to our work.

2.1.1 The Suprime-Cam Catalog

During our work, we constructed two catalogs (one for each filter) from the dataset produced during the Suprime-Cam observations. This dataset resulted from observations centered at ($\alpha \sim 285.47$, $\delta \sim -36.95$) for a ~ 0.255 deg^2 field-of-view. We catalog a total of 21 133 sources for the W-S-I+ filter, and 22 969 sources for the N-A-L656 filter. In Chapter 3, we present the steps taken during data reduction which detail how these catalogs were produced.

2.1.2 DENIS

The Deep Near Infrared Survey of the Southern Sky (DENIS; Epchtein et al. 1999) was conducted between 1995 and 2001. It observed the southern sky in three different bands (Gunn-i, J and Ks bands). The sources detected by the survey have positions with errors below 1 arc-second, and magnitude measurements with accuracies better than 0.1 magnitudes. We use the I-band information provided by the DENIS catalogue to calibrate our W-S-I+ source catalog because of the similar response curves of both the DENIS and Suprime-Cam I-band filters. There are 4 542 sources from the DENIS catalog in the region observed by the Suprime-Cam, with 2 311 also featuring in the W-S-I+ catalog.

2.1.3 VHS

The Visible and Infrared Survey Telescope for Astronomy (VISTA) Hemisphere Survey (VHS; McMahon et al. 2013) is ongoing and will image almost all of the southern sky. One of the scientific motivations for this survey is the detection of low-mass stars, and its catalog reaches

4 magnitudes deeper than both the DENIS and Two Micron All-Sky Survey (2MASS, another major NIR all-sky survey) catalogues. This is why we chose the latest VHS data release (VHS Data Release 6, hereafter VHSDR6) to aid both in the photometric calibration step as well as the candidate member selection from our dataset. We matched our catalog with VHSDR6 to obtain J- and K-band magnitudes for our sources. There are 43 151 VHSDR6 sources in the field observed by the Suprime-Cam, and 21 129 sources have a counterpart in the W-S-I+ catalog.

2.1.4 Gaia

The *Gaia* mission aims to create a 3D map of our galaxy around the Solar system. It can achieve this due to the unprecedented precision of positional measurements provided by the *Gaia* spacecraft. *Gaia* will perform 70 different observations of a total of 1 billion sources throughout its five-year lifetime. This, in turn, will result in very accurate kinematic information about these sources, since their movement across multiple observations will be recorded with high precision. Because of this, we use *Gaia*-published PMs and parallaxes for sources in our dataset (when available) when selecting candidates based on their kinematic properties. We use the most recent release from the *Gaia* survey − Gaia eDR3 (Gaia Collaboration et al., 2021). There are 8 994 *Gaia* objects in the region observed by the Suprime-Cam, with 6 888 being present in our W-S-I+ source catalog.

2.1.5 Confirmed Members of Corona Australis

A list of previously spectroscopically confirmed members of CrA was compiled. Because we focus solely on spectroscopically confirmed members of the cloud, this list does not include the photometric candidates from works such as those by e.g. López Martí et al. (2005), Haas et al. (2008), Peterson et al. (2011), among others. Due to their asserted membership to the cloud, the sources in this list help constrain the photometric and kinematic properties of members of the CrA SFR. These constrains are fundamental when selecting a list of sources from our data which constitute probable members of the CrA cloud. Because we use PMs from the *Gaia* catalog (Gaia Collaboration et al., 2021) for candidate selection, we take only the objects from our list of CrA members which are also present in *Gaia* EDR3. Our list of known CrA members can be found in Table B.1. Below, we detail how this compilation was produced.

The oldest confirmed members of CrA are R CrA, T CrA, S CrA, TY CrA, VV CrA, DG CrA and HD 176386. They have been studied spectroscopically multiple times over the past century (e.g. Hubble 1922; Joy 1945; Mendoza et al. 1969; Herbig and Kameswara Rao 1972; Marraco and Rydgren 1981; Bibo et al. 1992; Casey et al. 1995; Reipurth et al. 1996; Valenti et al. 2003; Forbrich and Preibisch 2007) in multiple different bands of the electromagnetic spectrum.

From previous X-ray observations of the CrA region, Walter (1986) selected and performed optical spectroscopy of three sources, which they confirmed as members of the CrA cloud: CrAPMS 1; CrAPMS 2; CrAPMS 3. Later, and using the same method, Walter et al. (1997) further confirmed eight more sources: CrAPMS 4–11. They identified these sources as PMS stars, with many of these objects not presenting the NIR excess associated with the presence of warm circumstellar disks around these sources.

Neuhäuser et al. (2000) also used X-ray data to build a list of sources for follow-up spectroscopy. They then performed low-resolution optical spectroscopy of these sources, and high-resolution optical spectroscopy of sources with detected lithium from their low-resolution

spectroscopy results. They identified 19 young PMS stars which they confirmed as members of the CrA SFR.

Also basing on X-ray emission for source-selection, Sicilia-Aguilar et al. (2008) performed optical spectroscopy of 56 objects in CrA as well as low-resolution IR spectroscopy for 14 of these sources. Sicilia-Aguilar et al. (2008) confirmed 12 new members of the CrA cloud. Three years later, Sicilia-Aguilar et al. (2011) continued this work by making spectroscopic observations of the remaining objects from their X-ray emission selection, confirming the membership of 6 other sources.

Meyer and Wilking (2009) performed optical spectroscopy of a list of objects from Wilking et al. (1997) which were candidate members of the CrA SFR based on their IR photometry. The spectra obtained from these sources encompassed emission lines, photospheric absorption lines and other relevant features, and confirmed or reinforced the membership of 23 objects.

2.1.6 DANCe

The goal of the Dynamical Analysis of Nearby Clusters (DANCe; Bouy et al. 2013) project is to do a thorough kinematic study of associations and clusters near the Solar system ($\leq$ 1 kilo-parsec). This study will help derive the mass functions of these regions as well as provide an insight on the internal dynamics within these young groups. In this context, Galli et al. (2020) utilized *Gaia* DR2 data to identify new members of the CrA cloud based on their PMs, parallaxes and colours. They used a Bayesian inference method to produce a catalogue of probable members of CrA, which resulted in a list of 313 objects. 36 of these objects are inside the field observed by the Suprime-Cam, with 10 of them showing up in the W-S-I+ catalog (21 of them show saturation in our images and were removed from our catalog, and one other had a de-blending flag associated). Still, these objects were not observed spectroscopically to confirm their youth and membership status. Because of this, we do not include them in our list of CrA members. Instead, we compare our candidate selection results with the DANCe catalog at the end of Chapter 4 to see which objects pass both our selection methods, and which do not.

We also cross-matched the DANCe catalog to *Gaia* EDR3 to check if there was a significant difference between the PMs values from the *Gaia* DR2 and *Gaia* EDR3 catalogs. There was a mean difference of $\overline{\Delta\mu_\alpha} \sim 0.1266$ (mas/yr) and $\overline{\Delta\mu_\delta} \sim -0.1266$ (mas/yr). They differ slightly but still reside in the CrA PMs space.

2.1.7 USNO-B1

The United States Naval Observatory B1 catalog (USNO-B1; Monet et al. 2003) is a sky survey using photographic plates of both the Northern and Southern sky. The catalog contains information on positions, photometric and kinematic properties, star-galaxy classification and respective errors for over 1 billion sources. Positions were recorded with an accuracy of 0.2 arc-seconds. The catalog is complete down to 21 magnitudes in the V-band of the optical. For each source, it provides measurements of up to five colours with a photometric accuracy of 0.3 magnitudes. There are 9 180 sources from the USNO-B1 catalog in the field observed by the Suprime-Cam and 4 629 of these sources feature in our W-S-I+ catalog. We use the USNO-B1 catalog to produce a list of available guide stars to be used during the follow-up spectroscopy observations, selecting those with brightness R $<$ 12 magnitudes.

Chapter 3

Data Reduction & Photometry

3.1 Suprime-Cam at the Subaru Telescope

The Subaru is a Japanese telescope located in Mauna Kea standing 4 139 meters above sea level on top of a dormant volcano on the Big Island of Hawaii (Figure 3.1). The summit is high enough that it extends beyond the weather systems, and since Hawaii is devoid of any nearby landmass, light pollution is minimal. These are pristine conditions for celestial observations since they minimize contamination effects that need to be corrected during data reduction.

The telescope operates in the visible and IR light and it was designed to deliver the highest resolving power available upon the time of its construction. A digitally-assisted support system carries the single piece primary mirror characterized by a small error of only 0.012 μm, with the involving cylindrical-shaped enclosure guaranteeing minimum air turbulence. It has an 8.2-meter diameter mirror with two Nasmyth Focus, one Cassegrain Focus and one Prime Focus (Fig. 3.1), and is widely renowned for obtaining high-quality images from its observations.

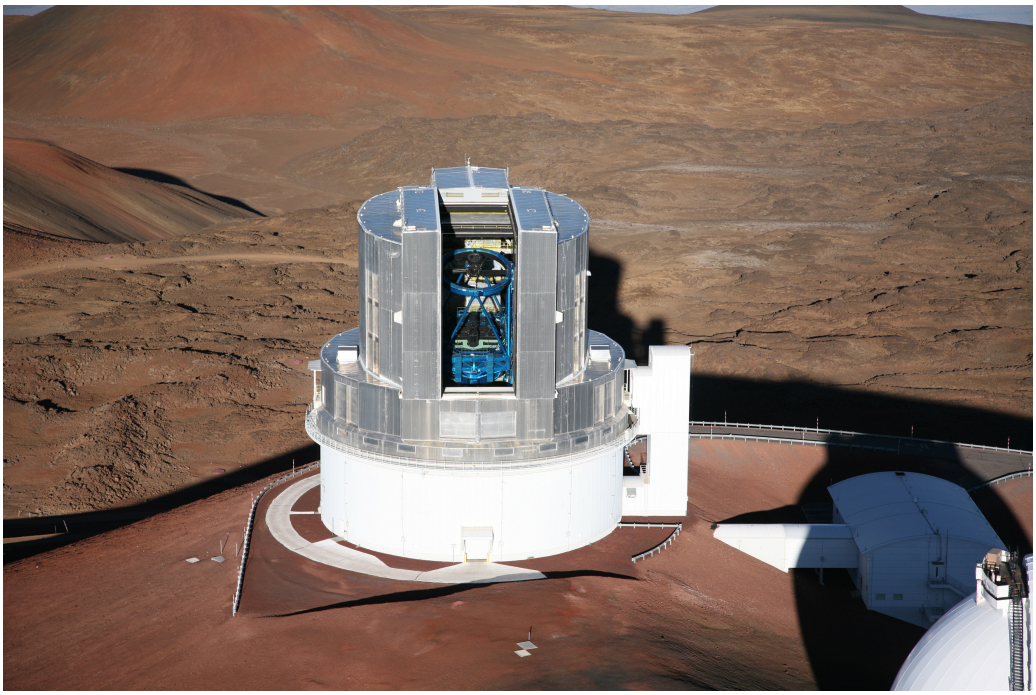

Figure 3.1: *On the summit of Mauna Kea stands the Subaru telescope, located four kilometers above sea level. Credit:* https://subarutelescope.org/en/gallery/facility/1998/11/11/1962.html.

The dataset relevant to our work was acquired using the Suprime-Cam instrument present at the Subaru telescope. This instrument was discontinued days after these observations were made (by the end of May, 2017), having been replaced by its new generation successor - the Hyper Suprime-Cam.

The Suprime-Cam instrument (Miyazaki et al., 2002) operated in the visible (447.8 nm − 905.4 nm; Miyazaki et al. 2002). It supported both broad-band and narrow-band filters, as well as custom-made user filters. It was composed of ten charge-coupled devices (CCDs) with physical separations (35.56 − 40.64 cm[1]) present between them. This disconnection is visible in the science images produced by the Suprime-Cam, and at least three dithered observations must be made in order to obtain a contiguous region of the sky. Each one of the CCDs in the Suprime-Cam is divided into four different channels horizontally, with each channel delivering its respective charge distribution to the overall electronic configuration of the CCD. This division of each CCD into four different channels is pertinent to the overscan reduction step of the dataset (Section 3.2.1).

The Suprime-Cam was capable of imaging a wide field-of-view while also detecting very faint objects with high levels of detail and contrast in a single exposure. For this reason, it was an optimal choice when looking for BDs since these are low temperature, faint bodies, and a wide-field approach allows for more of these objects to be detected in one single observation. Some of the more important camera specifications are listed below (Miyazaki et al. 2002[2]):

- Field-of-view: 34 x 27 square arc-minutes;
- Ten 2048 x 4096 pixel CCDs in a 5x2 configuration (a total of 80 megapixels);
- Pixel size: 15 μm;
- Angular pixel size: 0.20";
- Gain: 2.5 − 3.7 e^- per Analog-to-Digital Units;
- Read noise: 10 e^-;
- Saturation level: 150 000 e^-;

The CrA field was observed by the Suprime-Cam in 5 individual exposures for each filter. The time of exposure for the W-S-I+ filter was 30 seconds, while for the N-A-L656 filter exposures of 180 seconds were made. This results in a total of 150 and 900 seconds of integration time for the W-S-I+ and N-A-L656 filter, respectively.

3.2 Data Reduction

Every dataset produced during observations must first have a number of instrumental effects corrected before it can be studied and analyzed - this process is called *data reduction*. The data reduction for the images taken using the Suprime-Cam was done using our own Python routines. During this data reduction process numerous steps were taken, which are represented schematically in Figure 3.2. Here, images used for calibration are shown in a yellow background,

[1] https://www.naoj.org/Observing/Instruments/SCam/ccd.html
[2] https://www.naoj.org/Observing/Instruments/SCam/parameters.html

while science images are shown in blue. Purple-boxed objects correspond to Python packages or external software used during the data reduction routines. Images which have undergone data reduction steps are flagged accordingly (OS - Overscan reduction; FF - Flatfield; BP - Bad Pixel reduction). Master flatfield images were used both for the flatfield step (Section 3.2.2) as well as to identify bad pixels in each CCD (see Section 3.2.3). The Cosmics Python module by Malte Tewes (based on the LACosmics package by van Dokkum 2001) was used to clean the cosmic rays present in our images (Section 3.2.4). The *AstroAlign* package (Beroiz et al., 2020) was used during the geometry correction step (Section 3.2.5). The *Astrometry* software (Lang et al., 2010) was used to perform coordinate calibration (Section 3.2.6). The data reduction was done in the same way for each CCD and our Python scripts can be found in our GitHub repository[3]. Here, the README-file has information on the different scripts and what they do. After the data reduction, we produced a mosaic of the field observed by the Suprime-Cam (Section 3.2.7), although this mosaic was not used to perform photometry.

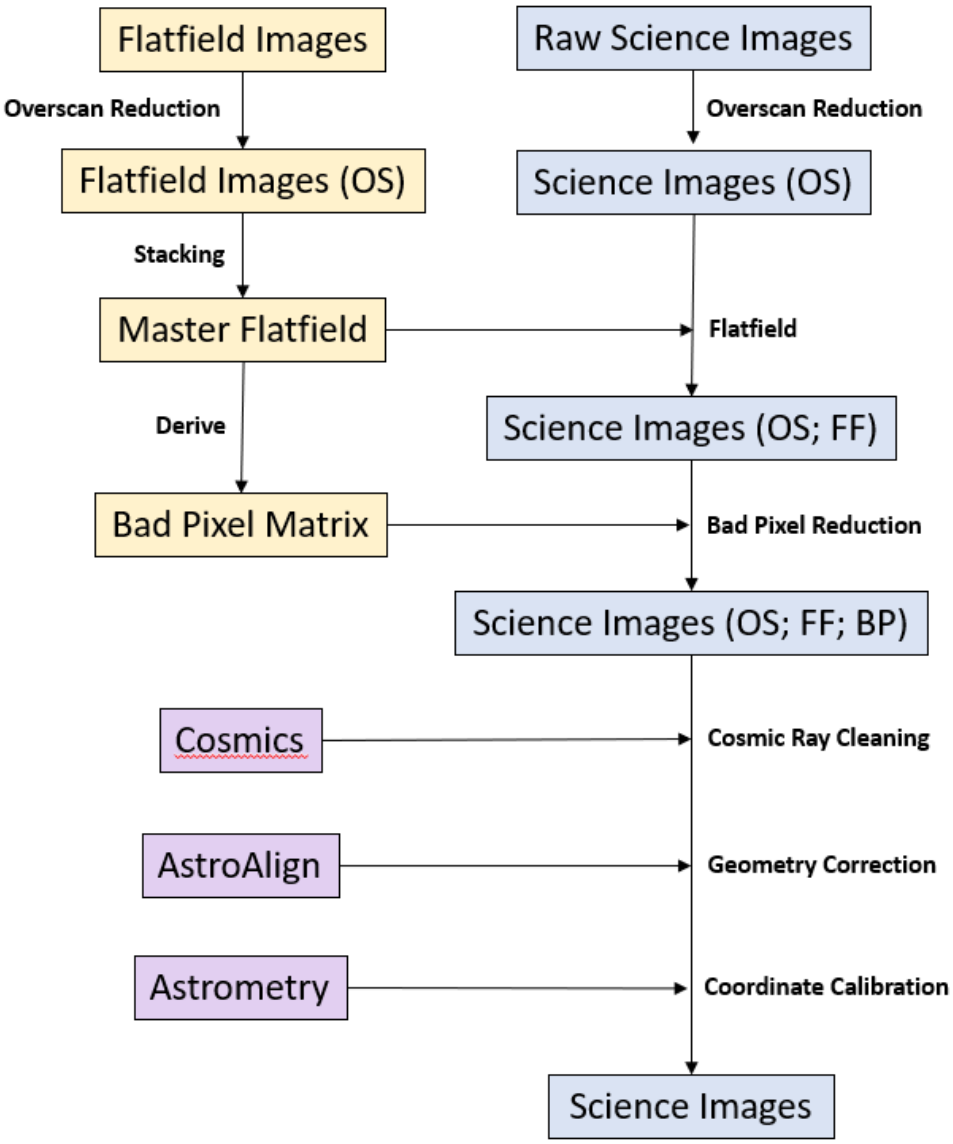

Figure 3.2: *Mapping of the steps taken during the reduction of the Suprime-Cam dataset. OS: Overscan reduced; FF: Post-Flatfield; BP: Post-Bad Pixel reduction.*

[3]https://github.com/codeman-andy/YOBD_CrA

3.2.1 Overscan Reduction

There is a bias intrinsic to every CCD - a voltage applied to avoid negative counts. In order to correct for the extra number of counts generated by this effect, a bias reduction is performed to the images. To know the values we have to subtract from the images, an instrument must have a way to record this bias effect so it can later be subtracted. For the Suprime-Cam, an overscan is generated after the exposure through a continued read of the CCD after the shutter has been closed and there is no light going through the system. These dark regions, highlighted in Figure 3.5, correspond to the overscan regions. There is a dedicated overscan region for each of the four channels in a CCD. The values registered in these overscan regions correspond to the bias of their respective channel. The reduction is applied by calculating the mean value for every overscan row. Some of the values recorded by the pixels in the overscan were not realistic (i.e. had extremely high values due to spillage from a source in the science image which was close to the border), producing a mean value for their row which was also unreasonable (i.e. a bias count $> 50\,000$). These rows had their means set to NaN. A 5-degree polynomial-fit function was then generated using the mean values of rows which were not set to NaN. The polynomial function then reproduced values for the rows with NaN means. Then, the rows in the object image were subtracted by the polynomial. This process was repeated for the horizontal part of the overscan region, but this time by averaging the columns rather than the rows.

In Figure 3.3, the bias recorded along the overscan region for one of the detectors is shown. Bias counts (blue dots) are virtually constant throughout the channel rows. The polynomial-fit (red line) is used to subtract the bias from the channel.

By the end of this reduction step, the overscan regions were removed and the images of all 4 channels were concatenated into a singular final image. This procedure was done on both science and flatfield images.

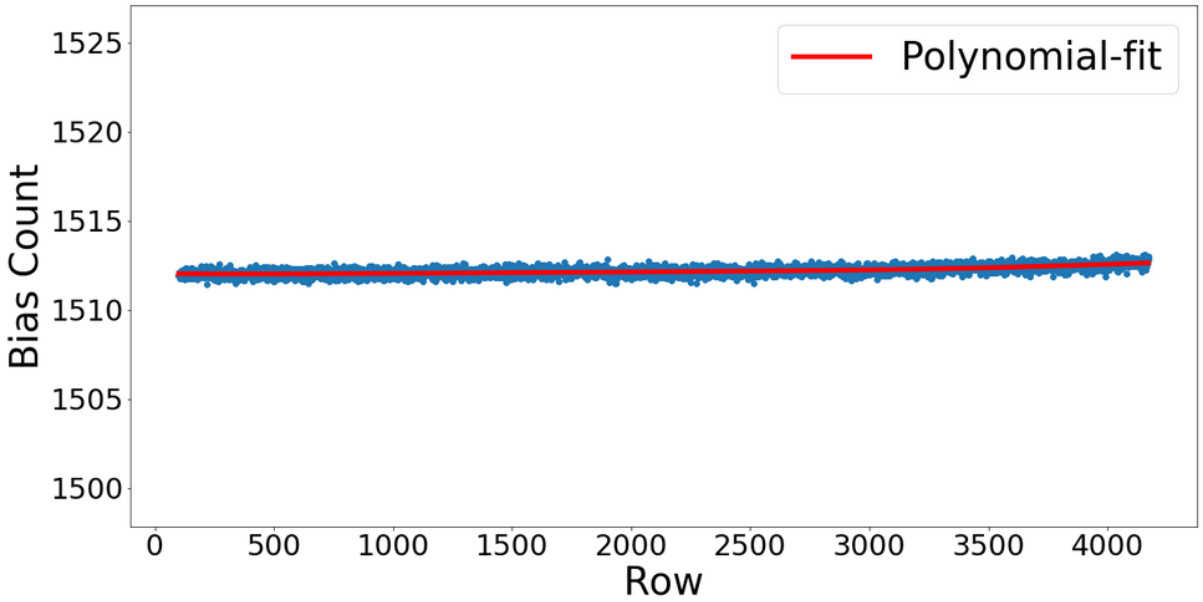

Figure 3.3: *The bias counts (blue dots) characteristic to one of the detectors. The X-axis corresponds to the row positions of the detector. A 5th-degree polynomial (red line) was subtracted from the object image in each channel.*

3.2.2 Flatfield

Another property of CCDs is that their pixels are not sensitive in the same way to the light being received, and some pixels produce different counts for a same amount of received photons. This effect can happen due to intrinsic properties of each pixel, but also due to interference in the optical path of the instrument (i.e. dust grains). All these effects are corrected during the flatfield routine.

To perform this correction, the instrument must take images of uniform surfaces - flatfields - since variations detected in these frames are easier to spot and are due to the different sensitivities of each pixel. Usually, these uniform surfaces flatfield images are taken from either a dome (dome flatfield) or the sky (sky flatfield):

- **Sky Flatfield**: Sky flatfield images must be taken either at sunset or sunrise. At these times, the sky is bright enough to outshine field stars (thus preserving its resemblance to a uniform surface), but also dim enough not to saturate the detector. These images must then be generated with extreme care, since exposures must be optimized not to overexpose the detector;

- **Dome Flatfield**: These are images taken of the inside of the telescope dome. Telescope domes are often diffuse, smooth reflectors. Dome images are also virtually featureless, since the dome is out of focus for the telescope optics. To generate these flatfields, a flat screen inside the dome is illuminated by a broad-band light with no emission lines (i.e. an incandescent lamp). Dome flatfields have the advantage that they can be taken at any time during the day.

For our data, dome flatfield images were taken on the same day-of-observation as the science images. Dome flatfields were created for each filter, since the responsiveness of a pixel is wavelength-dependent. These flatfield images were then divided by their own respective median to obtain values around unity across the image. Flatfield images of the same CCD and filter were stacked, and a median of all images was calculated creating a master flatfield image (Fig. 3.4). Science images were then divided by their corresponding detector and filter master flatfield image, thus correcting the different sensitivities of each pixel in the CCD.

3.2.3 Bad Pixel Reduction

Every CCD has pixels which constantly record low values (cold pixels) or high values (hot pixels). This can happen either due to fault of production, use or due to time in active duty. To correct for cold pixels, matrices of 0s and 1s were created from the master flatfield images where pixels with values of 1 flagged the position of cold pixels on the detector. These matrices were created from the master flatfield images since they have a lot of flux, making it easier to detect cold pixels (in Figure 3.4, pixels with count values smaller than the chip average are easily detected as white dots). Cold pixels were flagged if they registered counts lower than half of the average of the CCD master flatfield image. To correct for these cold pixels, our Python routine run through each pixel on the CCD and, whenever it encountered a pixel flagged as cold in the bad pixel matrix, an interpolation was made using the values of the surrounding pixels in a 9x9 square. Figure 3.5 shows the same science image before and after overscan reduction, flatfield and bad pixel reduction.

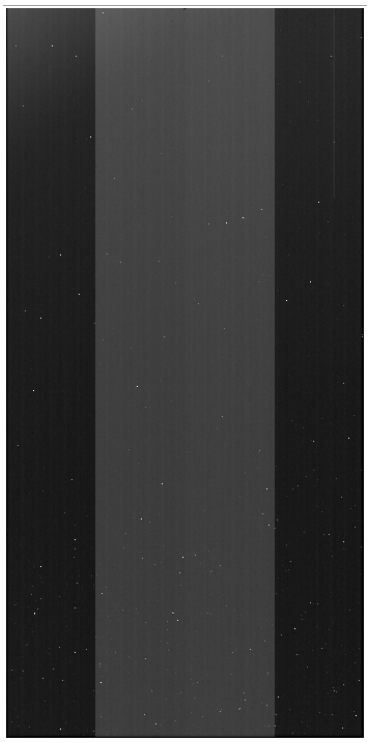

Figure 3.4: *A master flatfield image for one of the detectors using the W-S-I+ filter. Here, colours were reversed. The white dots scattered around the image are pixels which present consistently low counts throughout observations (cold pixels).*

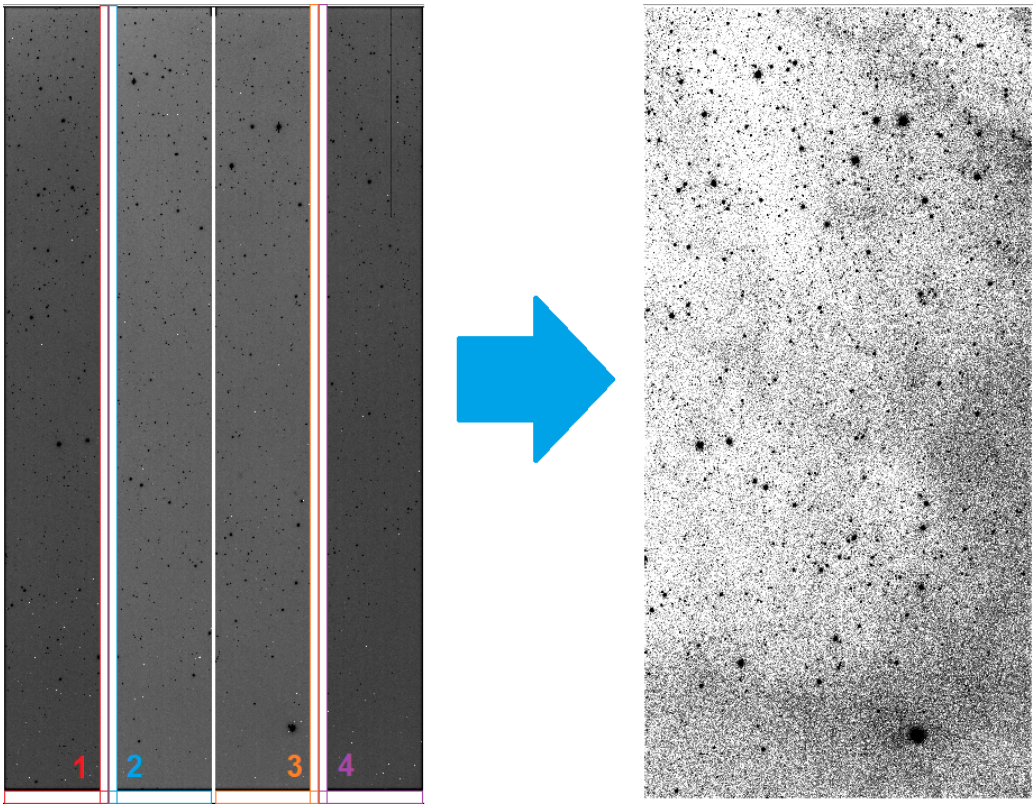

Figure 3.5: ***Left****: A raw broad-band W-S-I+ image taken by one of the detectors before overscan reduction, flatfield and bad pixel reduction. The four channels have been colour-coded along with their respective overscan regions.* ***Right****: The same image after overscan reduction, flatfield and bad pixel reduction.*

3.2.4 Cosmic Ray Cleaning

Cosmic rays are atomic nuclei (protons and neutrons) travelling through space at nearly the speed of light (with energies $\sim$ 0.3 GeV). When they reach our atmosphere, they collide with molecules and atoms producing a cascade of less energetic particles. As such, some of these cosmic rays decay into a stream of photons in the optical and are detected in our images. To clean these contaminants, we used a Python module written by Malte Tewes based on the Laplacian Cosmic Ray Detection (LACosmics) algorithm developed by van Dokkum (2001). This algorithm identifies cosmic rays in images from the sharpness of their edges, allowing the detection of cosmic rays independently of their appearance. The Malte Tewes module has the additional feature of recognizing saturated stars and their trails in the images, so that they are not mistaken for cosmic rays. In Figure 3.6, we show a cut from one of our images where a cosmic ray is present (flagged by the red arrow). The string-like appearance of the cosmic ray distinguishes it from the surrounding sources (black dots).

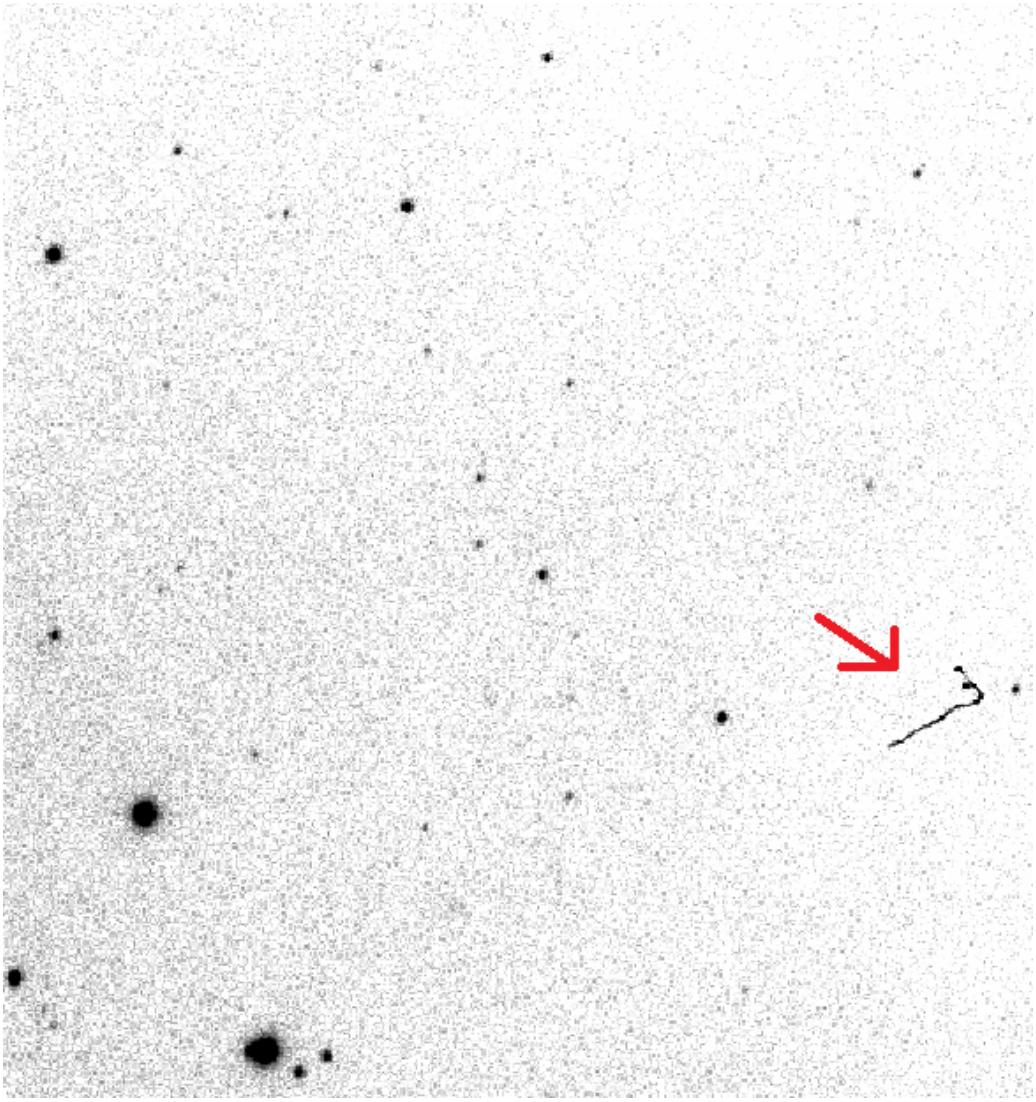

Figure 3.6: *Cut from an image taken by one of the detectors using the W-S-I+ filter. Colours were reversed. A cosmic ray can be seen near the bottom-right. Cosmic rays are usually recorded in images as these irregular lines since they are the result of the decay of primary cosmic rays which collide with matter present in the upper layers of our atmosphere. A shower of less energetic particles is produced from these collisions giving cosmic rays their particular shape in science images.*

3.2.5 Image Stacking and Geometry Correction

Five dithered observations were made when observing the CrA cloud. This means that each detector produced five different images during observations. These dithered images still need to be combined into a single deep exposure. A correction for the geometry of the mirror (the curvature of the telescope lens), as well as for the spherical nature of the sky, also needs to be made (Figure 3.7). Since 5 different observations were made for each filter, it is possible to define this curvature from the different orientation of the sky on each of the observations, along with the different positions of a same source across the various images.

For this step, we used the *AstroAlign* package (Beroiz et al., 2020). It takes all the images taken by a detector and checks for common sources between them to use as reference for its alignment routine. Then, it re-positions the images to correct for the rotation of the sky in between each set of observations. Our routine for image stacking and geometry correction consisted of the following steps: 1) first, we chose one image to be used as a reference to align the other images to; 2) then, we ran *AstroAlign* on a pair composed by the reference image and one of the other images, performing a first-order transformation; 3) we used SExtractor on the resulting transformed image; 4) finally, we ran *AstroAlign* again on the catalog produced by SExtractor, now using the pixel coordinates of the matched sources between the two images, resulting in a more sophisticated transformation. These steps were repeated until all images were aligned to the chosen reference image. The solution is a median-combined aligned image from all five dithered images taken by the detector.

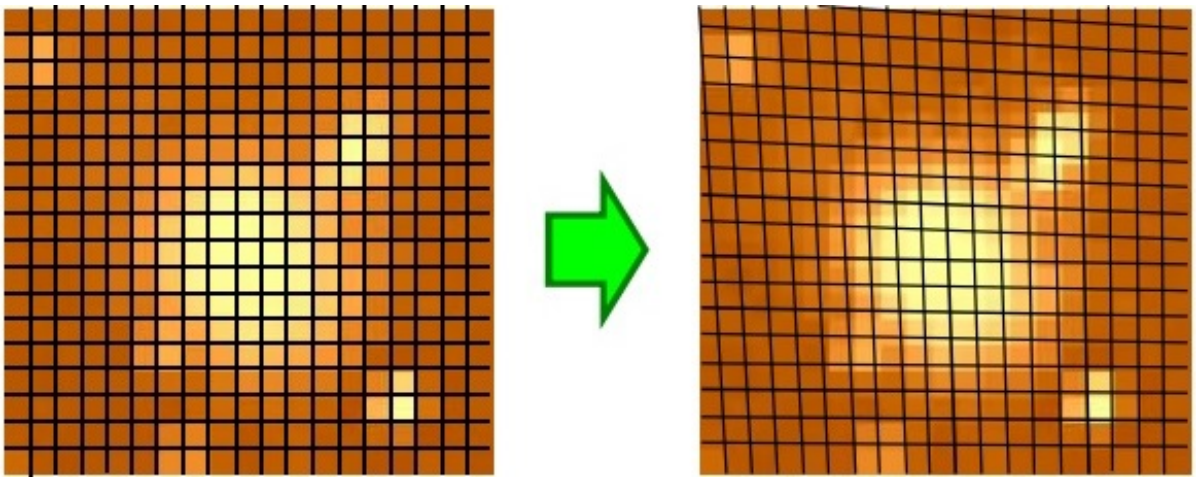

Figure 3.7: *Geometric correction applied to a science image. The grid in the right-side image appears slightly deviated so as to present us with a flat image of the captured source. Credit:* https://subarutelescope.org/Observing/DataReduction/School2014/SubaruSchool2014_introduction_imaging.pdf.

3.2.6 Coordinate Calibration

All sources in our science images have pixel coordinates, but these coordinates still need to be calibrated onto the World Coordinate System (WCS). To do this, a transformation of pixel coordinates into physical coordinates needs to be defined. During this step, we used the local version of the *Astrometry* software (Lang et al., 2010). *Astrometry* performs coordinate calibration by taking a set of sources from an image and then looking for matches in a large, pre-computed library. This is a library of known asterisms - patterns or groups of stars smaller than a constellation. The library was created from a group of public all-sky catalogs, such as

the USNO-B1 (Monet et al., 2003) or the 2MASS (Cutri et al., 2003) catalogs. When querying a set of sources from images, *Astrometry* searches for asterisms in the library which best align with the queried objects. It is this computed alignment which defines the translation of pixel coordinates into WCS coordinates. The quality of the alignment is determined using a Bayesian decision process. For a given alignment, *Astrometry* takes another subset of sources from its library which are close on the sky to the aligned sources, and checks if these sources are also found in the queried image. When this is true, it repeats this process until enough alignments are found to accept a match. If it cannot find a subset of sources from the library in the queried image, it rejects the match and continues the search. We ran *Astrometry* on all of our science images successfully, obtaining physical coordinates for all of our sources. Matching our catalog with *Gaia* EDR3 (Gaia Collaboration et al., 2021), we can measure the quality of our calibration by calculating the mean difference between the WCS coordinates determined for our sources and their respective values in *Gaia* EDR3. For the W-S-I+ catalog, the mean difference in the right-ascension of our sources is $\sim 0.023 \pm 0.216$ arc-seconds and in the declination is $\sim 0.190 \pm 0.171$ arc-seconds. For the N-A-L656 catalog, the values are $\sim 0.020 \pm 0.245$ arc-seconds for the right-ascension and 0.224 ± 0.232 arc-seconds for the declination. These values show a good agreement between our coordinates and those measured by the *Gaia* mission, with the mean differences here presented being smaller than one arc-second.

3.2.7 Mosaicing

We produced a mosaic of the field observed by the Subaru telescope. Because the Suprime-Cam has ten CCDs which are separated physically, as mentioned in Section 3.1, in order to create a continuous image of the sky the images produced by each individual CCD were connected. To do this, we used the *reproject* package in Python (Robitaille et al., 2020). *reproject* calculates the optimal projection for a set of images and collates the images together in this projection. This mosaic was not used to produce the list of candidate objects for follow-up spectroscopy since we decided to perform photometry on each chip individually. Even though we levelled our images to create a more homogeneous view between each detector, the method used is a simple one, and the differences in the background levels, which are hard to correct for precisely, may introduce biases if we were to perform photometry on the entire mosaic. Also, due to residual distortion effects at the edges of the detectors, miscoordinates may arise which would lead to mismatches when calibrating the flux from the sources in our dataset. Instead, the produced mosaic is used just to provide a good view of the field observed by the Suprime-Cam. It is shown in Figure 3.8, where colours have been reversed (bright sources are darker, while regions affected by extinction or with low background emission are whiter).

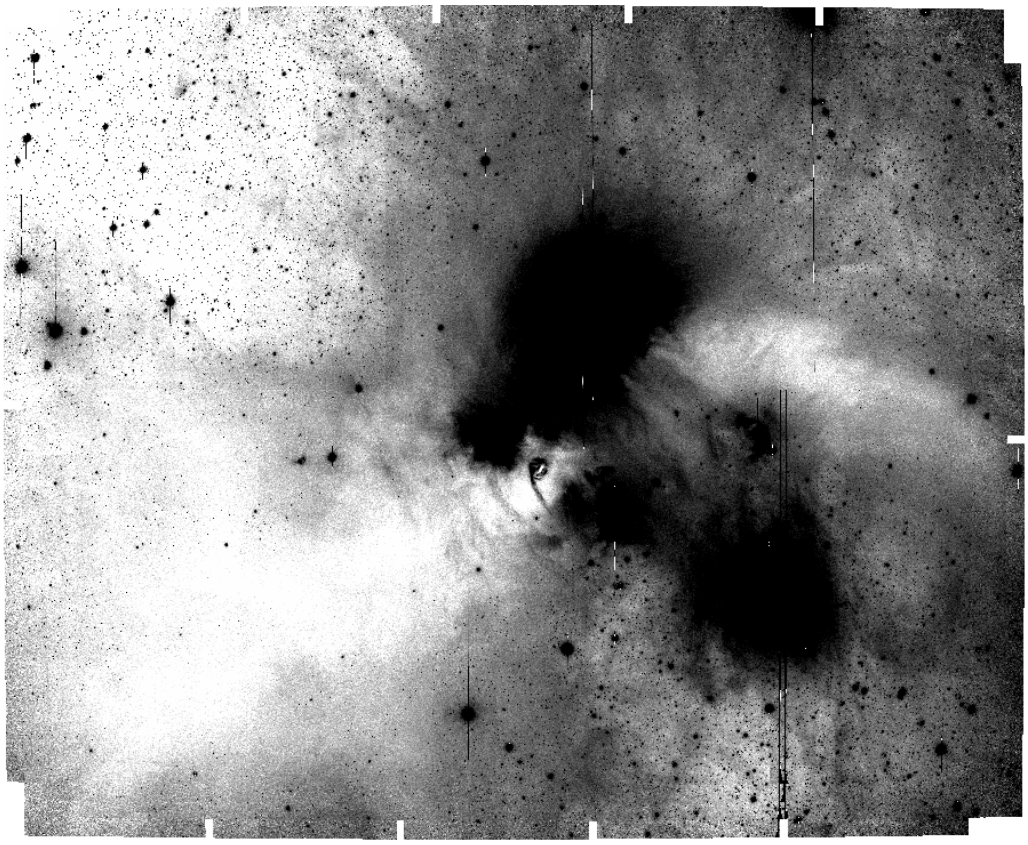

Figure 3.8: *The mosaic of the images taken by the Suprime-Cam using the W-S-I+ filter. We do not perform photometry on the mosaic. It serves only to illustrate the observed field of the CrA cloud.*

3.3 Photometry

The last step before the discussion of candidate sources is performing photometry on the images captured by the Subaru telescope. At this point, the flux values of the sources in these images are given in number counts. These counts need to be converted into pseudo-flux values which are then calibrated onto an existing magnitude system, setting these values on a convenient scale and allowing us to do photometric studies of these objects. In this section, we detail how we determined the flux values for our sources, and how we calibrated these flux values using the DENIS (Epchtein et al., 1999) and VHS (McMahon et al., 2013) public catalogs.

SExtractor & PSFEx

Source Extractor (*SExtractor*; Bertin and Arnouts 1996) is a program used to extract the positions, flux values, ellipticities, along with many other parameters, of sources present in an astronomical image. We used *SExtractor* on our images to obtain pseudo-flux values for our sources, which are used to build the point-spread function (PSF) of each image. The PSF describes how the light from a point source is diffracted onto the image plane of a detector. Sources with counts over 30 000 were considered to be saturated. To build the PSF models, we used the *PSF Extractor* (*PSFEx* ; Bertin 2011). *PSFEx* constructs the PSF models of images which were previously processed by *SExtractor*. In order to run *PSFEx*, the catalog generated by *SExtractor* must be fed into the *PSFEx* program. This catalog must contain certain information related to the image being processed. Namely, it must describe the size of the

vignettes associated to each object. These vignettes are cuts from the original image of suspected point sources. We chose a size of 45 x 45 pixels for the vignettes. The *SExtractor* catalog must also indicate the fixed aperture size which will be used to normalize the amplitude of the PSF models. This aperture must be wide enough to negate the influence of seeing or aberration in different vignettes, but not too wide that it becomes susceptible to pollution from nearby sources. We used an aperture size of 20 pixels. *PSFEx* then looked through the *SExtractor* catalog and selected entries likely to be point sources, based on measurements like their ellipticity. The *SExtractor* catalog must then also provide information about the elongation of the sources. *PSFEx* rejected sources with an ellipticity > 0.1. *PSFEx* will also exclude, if instructed to, sources which present contamination or saturation effects. For this, *SExtractor* uses a system of flags to warn both *PSFEx* and the user of issues found when dealing with some of the sources. They diagnose cases where photometry may be biased by the presence of a nearby source, or when pixels were found to be saturated for a given object (along with other scenarios). *PSFEx* excluded all sources with *SExtractor* flags, with the exception of sources flagged for being in crowded environments. For the selected sample of vignettes, *PSFEx* then began an iterative process of modelling the image PSF from the vignettes of the sample. In each iteration, the modelled PSF is compared to the data from the image, producing a more accurate PSF model with each iteration. Neighbouring sources present in the vignettes are also filtered during this time. After this process is over, the PSF model is stored into a file along with relevant diagnostics. Then, a second run of the *SExtractor* software is made on our images, but this time it estimates the flux from our sources using the generated PSF models. For this second run, extracted sources had to present at least a 2.7 σ flux variation across 4 pixels from the background. Sources with counts over 44 000 were considered to be saturated. This is a higher value than the one used during the first *SExtractor* run because we wanted to exclude extremely bright sources from the samples used to produce the PSF model, since these sources would sometimes generate an artificial halo around them in the images which would become an extra source of contamination. In Table B.2, we list the most relevant *SExtractor* configuration parameters used during our routines. Parameters not shown here were used with their default values. Various configurations were tested out and its products visually inspected to minimize the number of false detections and missed point-sources. In Table B.3, we list the parameters calculated for each source by *SExtractor*. The configuration used during our *PSFEx* run is shown in Table B.4. These parameters were also used when performing our routine for the N-A-L656 catalog, with the exception that we set the SATUR_LEVEL to 42 000. These parameters were selected by visually inspecting the samples of vignettes used during the *PSFEx* run and the residuals outputs of each configuration. The residuals are images which result from the subtraction of the PSF model from the original image. The smoother this subtraction is the better, and the photometry is more reliable. The bright sources will always leave some residuals, in particular those that are saturated (their PSF is distorted). The fainter sources should, however, be nicely subtracted. As such, in order to construct a good PSF, we looked for a configuration which avoided bright sources whilst making sure there was a considerable number of vignettes for the detectors that observed the darker regions of the cloud. So, a comparison of the original sample of vignettes with the residuals serves as a quality control for the photometry. In Figure A.2, we show the sample of vignettes used and the residuals output of a *PSFEx* run for the Clarisse detector for demonstration purposes. The overall sample selection of vignettes is suitable for modelling the PSF, which is also reflected on

the overall smoothness of the residuals image.

Our full *SExtractor* + *PSFEx* routine then took three steps:

- a) On the first step, the sets of sources from the images are extracted and recorded by *SExtractor*. A fixed photometric aperture 20 pixels wide was used to measure the flux from the sources. We defined the SATUR_LEVEL at 30 000;
- b) The catalog produced during the first step is then used to build the PSF models of each image. Here, we used the *PSFEx* program to generate these models. Different configurations were tested (i.e. by examining different values for the SAMPLE_VARIABILITY and SAMPLE_MAXELLIP parameters) to produce the most reliable PSF models possible;
- c) The *SExtractor* software then performed model-fitting photometry on the sources in a given image by utilizing the respective PSF model generated during the previous step. This provides much more reliable measurements since it takes into account the way each detector records the photons being received.

As mentioned before, while *SExtractor* compiled the sources in each image, it attributed flags to these objects. We removed all flagged sources from the final catalog. For the W-S-I+ filter, we catalogue a total of 46 898 sources, and for the N-A-L656 narrow-band filter 32 166 sources.

Calibrating to DENIS

The catalogs created during the *SExtractor* + *PSFEx* routines now have pseudo-flux values for all sources, but these values are not in physical units yet. To do this, the catalogs must be calibrated to an existing photometric system. This calibration can be achieved by matching our catalogs against public catalogs of CrA which use the magnitude system we desire. The public catalogs must also possess magnitude measurements in the bands at which our observations were made in order to calibrate the flux from our sources in these bands. There are not any publicly available catalogs of CrA with H_α measurements, so we cannot calibrate the catalog of the N-A-L656 filter. For the W-S-I+ filter, we cross-match our data against the DENIS catalog (Epchtein et al., 1999) which uses Vega magnitudes. But first, the flux values of our sources are converted onto instrumental magnitudes by using the equation:

$$m_{instr} = -2.5 \log(f/t_{exp}) \tag{3.1}$$

where m_{instr} is the instrumental magnitude of a source, f is the calculated flux value of the source, and t_{exp} is the exposure time of the images collected using the W-S-I+ filter ($t_{exp} = 30$ seconds).

Because our catalog is not yet calibrated, the calculated instrumental magnitudes (m_{instr}) of our sources differ from those reported by the DENIS catalog by an offset - the *zero-point* (ZP). The ZP is the magnitude required to produce one count on the detector per second (in other words, $\log(f/t_{exp}) = 0$). Hence, it is different for each of the 10 detectors in the Suprime-Cam. Because the response curve of the W-S-I+ filter inevitably differs from the DENIS I-filter, there can also be a non-negligible wavelength-dependent correction - the *colour-term*. The colour-term correction was calculated using both the I-band from DENIS (Epchtein et al., 1999) and the J-band from the VHSDR6 (McMahon et al., 2013) catalog. The catalogs of each detector were

cross-matched to the DENIS and VHSDR6 catalogs with matches requiring a separation < 1". Both ZP and colour-term corrections were calculated through a linear fit shown in the right panel of Figure 3.9, where the ZP corresponds to the intersection of the fit and the colour-term to the slope:

$$m_{calib} = m_{instr} + ZP + CT(I_{DENIS} - J_{VHS}) \tag{3.2}$$

where m_{calib} is the calibrated magnitude of each source and I_{DENIS} and J_{VHS} are the magnitude of each source in the I- and J-band taken from the DENIS and VHSDR6 catalogues, respectively. The calibrated I-band magnitude for each source is obtained by applying the calculated ZP and colour-term of their respective detector. Magnitude errors were calculated using standard error propagation formulae.

In Figure 3.9, we show the photometric calibration performed for one of the detectors. We also show the errors as a function of magnitude for the same detector in Figure 3.10. This process was made individually for each chip, since each detector has its own ZP and colour-term. When calibrating the sources observed by a detector (blue dots), not all of them were used to calculate the linear fit of some of the chips. This is because the faintest sources in these chips present a lot of scatter (i.e. the difference between the Suprime-Cam and DENIS magnitudes has a high variation for fainter magnitudes). The brightest sources in some of the detectors were also left out from the fit, since they displayed a non-linear relationship to the DENIS catalog for brighter magnitudes. A cut was then made in four of the chips selecting only sources with a determined instrumental magnitude $-10.7 < m_{instr} < -9.6$, and $-10.5 < m_{instr} < -9.6$ for one other detector. Some of the selected sources still constituted outliers in the colour-colour diagram, and would influence the fit. To remove these outliers from the list of sources used to calculate the fit, sources outside a 3-σ deviation were removed from the pool. The remaining sources used to calculate the linear-fit are shown as orange dots. For two of the detectors, no cuts were made since the sample was already small to begin with. The distribution of the detectors on the Suprime-Cam can be found in Annex A, along with all the calibration and error versus magnitude plots for each of the detectors.

At the end of the photometry calibration process, all catalogs from the different chips were joined into a single one. Some sources would feature twice (sometimes thrice) in this final catalog since they were detected on edges adjacent to different chips. These sources had their sky position, elongation, ellipticity, signal-to-noise ratio (SNR), fluxes, magnitudes and associated errors averaged. Our final W-S-I+ catalog has 21 133 sources and contains I-, J- and K-band measurements for each source (some sources do not have K-band measurements since these were not provided by the VHSDR6 catalog), along with astrometry positions and the associated errors to all of these parameters. From now on, this final catalog will be addressed as *our IJKs catalog*. We also average the duplicate and triplicate sources in our N-A-L656 catalog, leading to a final list of 22 969 sources with H_α measurements.

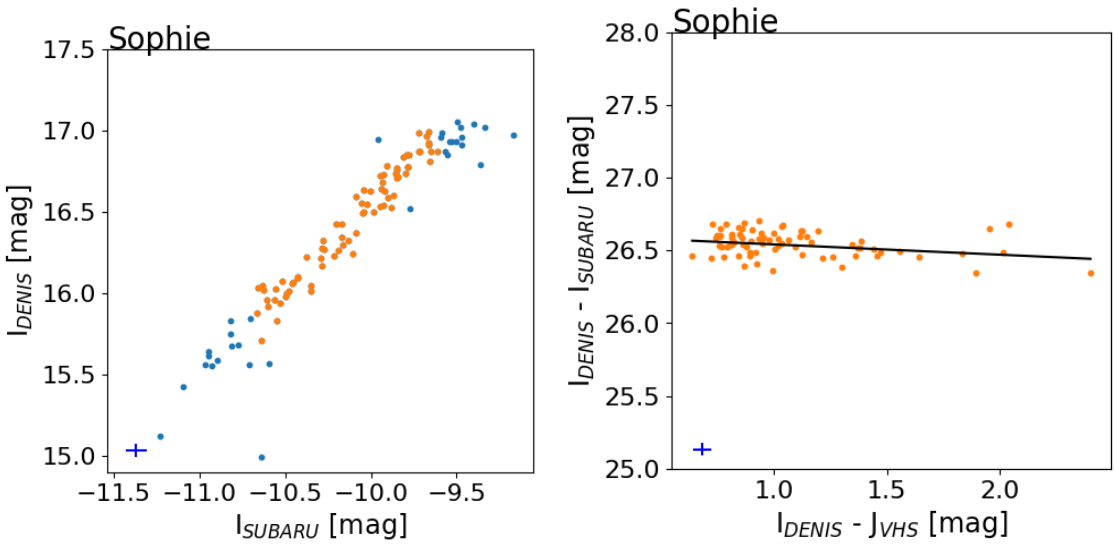

Figure 3.9: ***Left Panel****: The instrumental magnitudes of sources from one of the detectors (Sophie) matched against their DENIS catalog magnitudes. A cut was made at* $-10.7 < I_{SUBARU} < -9.6$ *magnitudes when selecting sources for the linear-fit. This is because fainter sources present high dispersion and a non-linear relationship between the two catalogs is seen at brighter magnitudes.* ***Right Panel****: The colour-colour diagram of the same detector where sources were matched against the VHSDR6 catalog to obtain* $I - J$ *colours. The orange dots correspond to the sources used to calculate the linear-fit presented on the plot.*

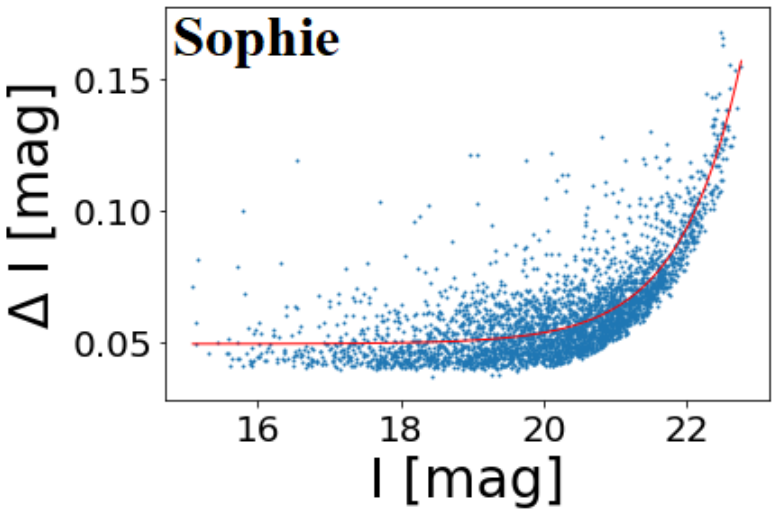

Figure 3.10: *The errors as a function of magnitude for the Sophie chip.*

Chapter 4

Candidate Selection

At this stage of our work, we aim to determine which of the objects in our catalog are most probable to belong to the CrA cloud. In this chapter, we detail our selection methods to determine the most probable young, low-mass members of CrA based on their kinematic and/or photometric properties. This selection will constitute the list of candidate objects for follow-up spectroscopy. Here, we list the results from the different steps taken:

- The starting point of our selection is the IJKs catalog produced by the Suprime-Cam observations which consists of 21 133 sources;
- $(I,\ I-J)$ photometric selection produces a list of 650 sources (Section 4.1);
- By performing a PMs study of these sources, we narrow down the sample from 650 to 19 objects. This new list is then further reduced to 15 sources by applying our parallax selection criterion. This list of photometrically and kinematically selected candidates will be referred to as the *Gaia*-selected sample (Section 4.2);
- For sources without *Gaia* kinematic information, we select a list of 313 sources which range from the magnitude limit of *Gaia* (I $\sim$ 19 mag) to 22 magnitudes in the I-band and that also pass our $(I,\ I-J)$ selection (Section 4.3). From the isochrone tracks these objects, if confirmed as members of CrA, have masses down to $\sim$ 4 M_{Jup}. This list is added to the *Gaia*-selected sample (the total number of selected sources now being 328) and becomes our final list of candidate objects for follow-up spectroscopy (Section 4.4);
- Using the H_α data from the Suprime-Cam observations, we look for bright emitters of this emission line (Section 4.5). We find a total of 24 bright H_α emitters with 3 featuring in our list of candidates for follow-up spectroscopy;
- Adopting a similar method to Pearson et al. (2020), we use empirical intrinsic stellar colours from Pecaut and Mamajek (2013) to estimate the extinction in the region observed by the Suprime-Cam. Using these extinction estimates, we build an extinction map of the observed field in Section 4.6;
- By complementing the *Besançon* galaxy model[1] with our extinction map, we are able to estimate the number of contaminants in our list of candidate sources. We determine an

[1] https://model.obs-besancon.fr/modele_home.php

expected contamination rate of $\sim 90\%$, which means we may confirm ~ 30 new planetary mass BDs with follow-up spectroscopy observations (Section 4.7).

4.1 Colour-Magnitude Diagrams

We started by creating CMDs of the sources in our IJKs catalog. In Figure 4.1, the (I, $I - J$) CMD of this catalog is shown. Since what we are interested in are PMS objects, these sources are redder in the CMD when compared with older objects already in the main sequence stage of their lives (blue dots). Although young objects are more luminous than their main-sequence counterparts (since they are still contracting, so their radii is larger), they show brighter emission at longer wavelengths due to their lower temperatures. Their optical emission is also absorbed by the surrounding environment (envelope + cloud) making the source appear redder. We therefore select only the sources (orange dots) with colours redder than a provided selection line (black line), similarly to other works from the SONYC group. This selection line was drawn manually, making the fit roughly follow the sequence of the known CrA members (green stars). The equation for the selection line is:

$$y = 4x + 8.6 \tag{4.1}$$

Our selection encompasses previously known members of CrA and also keeps in mind the very cool candidates whose sequence, according to the models, may shift slightly towards the blue. In our diagrams, we also plot the isochrone tracks for 3 Myr from the BT-Settl (Allard et al. 2011; dashed line) and AMES-COND (Allard et al. 2001; Baraffe et al. 2003; sparsely dashed line) models. The BT-Settl model is an evolutionary model with masses ranging $0.01 - 1.4$ $M_\odot$. It was computed using the atmosphere code *Phoenix* which is more up to date than the AMES-COND model, having revised solar abundances from Asplund et al. (2009), an upgraded cloud model, and also including the BT2 water opacity line list from Barber et al. (2006). The AMES-COND evolutionary model reaches masses down to 0.0005 $M_\odot$ (or 0.5 Jupiter-masses). It simulates the presence of dust in the atmosphere while ignoring its opacity. These models are plotted in the same photometric filters used for our IJKs catalog (DENIS and VHSDR6), and adapted to the distance of CrA (150 pc; Galli et al. 2020). The tracks built from these models provide estimates for the mass range of our selection. As shown in the CMDs, our catalog reaches masses below 0.005 $M_\odot$ (~ 5 Jupiter masses). We also plot the reddening vector (black arrow) constructed using the extinction law from Cardelli et al. (1989).

From our original IJKs catalog of 21 133 sources, a list of 650 objects is produced from this CMD-selection method (hereafter, called CMD-selected). Although these sources have been photometrically selected, many of them are contaminants. These may be embedded giant stars, reddened background M-type stars which do not belong to the CrA SFR or, less likely, foreground objects. Background galaxies have also been mistaken for YSOs in CrA (see e.g. Peterson et al. 2011). As the next step, *Gaia* EDR3 data (Gaia Collaboration et al., 2021) is cross-matched with the CMD-selected sample in order to establish probable members of the CrA cloud.

Completeness Limit

When plotting the distribution of sources across a range of magnitudes, a higher number of sources are expected to be detected at fainter magnitudes. This is because, in whichever direction we observe the sky, the number of sources increases with the distance to Earth. Because they

are more distant, they will also appear fainter. But, because exposure time is limited, there is a completeness limit up from which an instrument cannot detect fainter sources. Calculating the completeness limit of a catalog lets us know that all sources up until the completeness limit were detected during the observations. To determine the completeness limit of our catalog in different bands, we plotted histograms in the I-, J- and K-bands, and defined the completeness limit as the half-measure of the bin before the peak in each histogram (Figures 4.2 and 4.3). Our catalog is complete down to 20.7 mag in the I-band, 19.5 mag in the J-band and 17.8 mag in the K-band. Adjusting the AMES-COND model (Allard et al., 2001; Baraffe et al., 2003) to the distance of CrA ($\sim$ 150 pc; Galli et al. 2020), at 3 Myr and with $A_V = 0$, these magnitudes correspond to objects with masses around 5 M_{Jup}, 2 M_{Jup} and 3 M_{Jup}, respectively. The completeness limit of our catalog is also plotted in Figure 4.1 (dashed line).

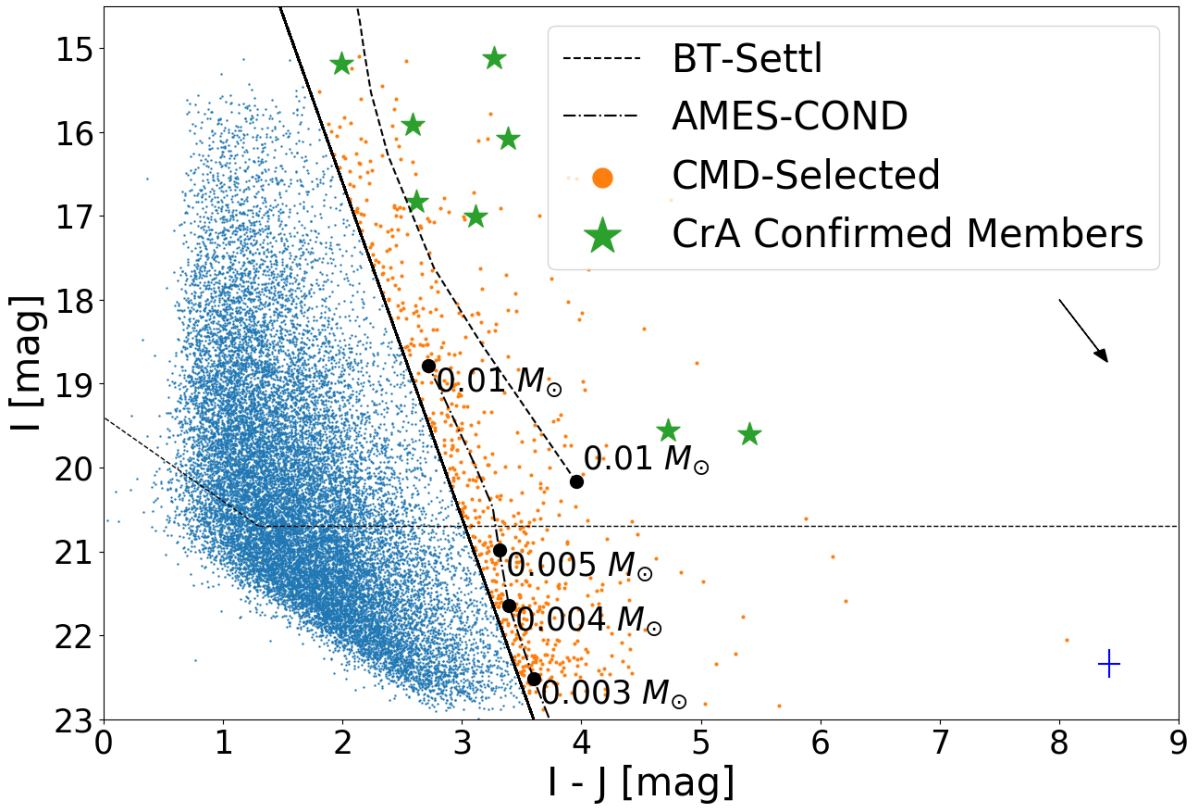

Figure 4.1: *The CMD of our IJKs catalog (blue and orange dots). Overplotted are the spectroscopically confirmed members of CrA (green stars) which feature in the magnitude range of our dataset. The black arrow is showing the extinction vector for $A_V = 1$ mag. The average errors for each axis are shown on the bottom right (blue lines). Errors for the I-band axis were enlarged by a factor of 5. When members did not have a match to our catalog (i.e. they are outside the observed field), they were matched to the DENIS catalog. A selection line was constructed manually following the sequence of known CrA members. The dashed line corresponds to the completeness limit of our sample. Objects bluer than the selection line are assumed to be field stars. Young objects, due to their lower temperatures, possess redder colours. We then select sources redder than the selection line, which will be subject to the kinematic selection step.*

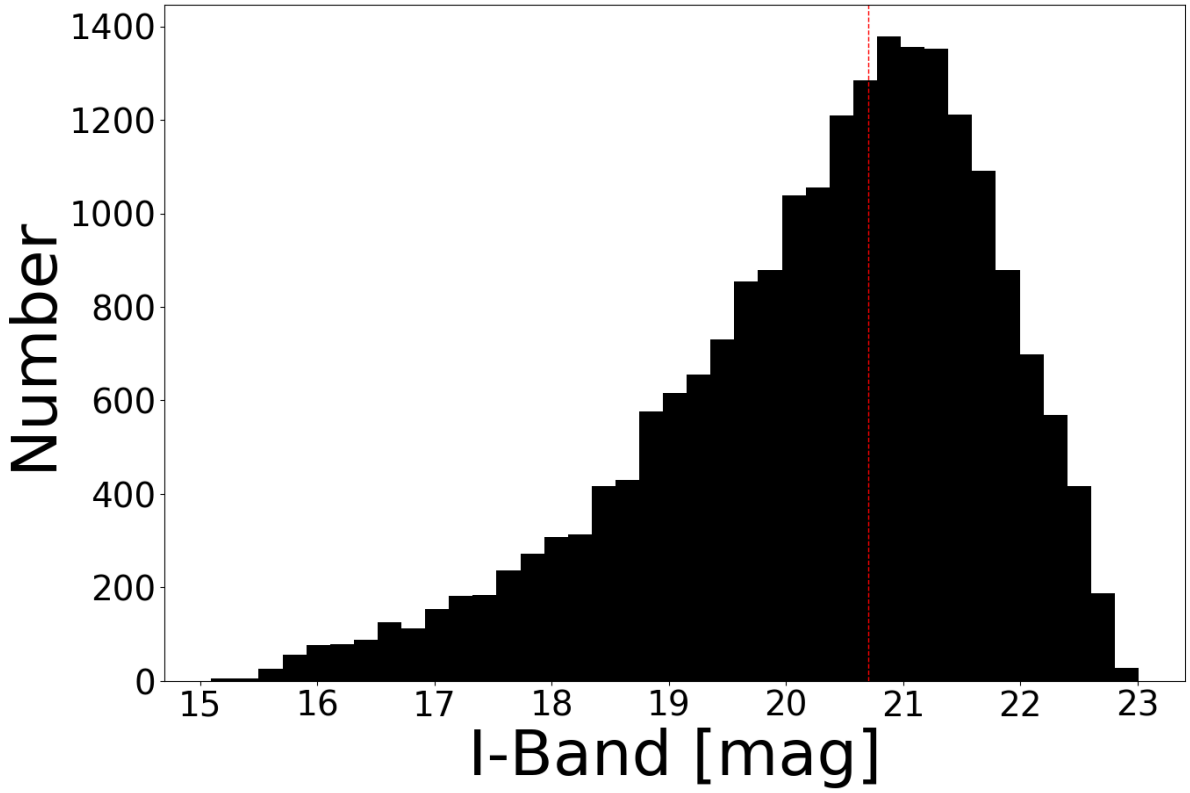

Figure 4.2: *Histogram of our IJKs catalog and the I-band magnitudes. The limiting magnitude for the data is $I = 20.7$ mag (dotted vertical line). This corresponds to $\sim 5\ M_{Jup}$ at 3 Myr and $A_V = 0$ in the AMES-COND isochrone.*

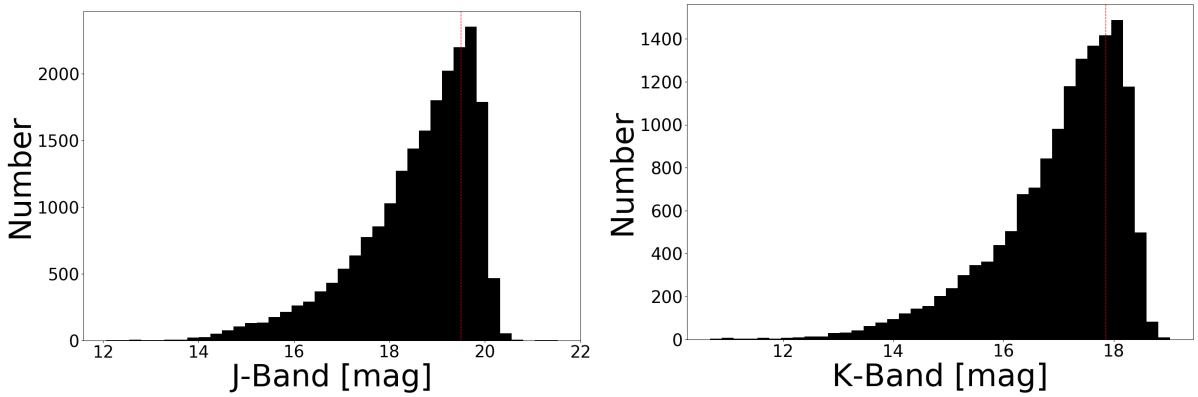

Figure 4.3: ***Left**: Histogram of our IJKs catalog and the J-band magnitudes. The limiting magnitude for the J-band is $J = 19.5$ mag (dotted vertical line). This corresponds to 2 M_{Jup} at 3 Myr and $A_V = 0$ in the AMES-COND isochrone. **Right**: Histogram of our IJKs catalog and the K-band magnitudes. The limiting magnitude for the K-band is $K = 17.8$ mag (dotted vertical line). This corresponds to 3 M_{Jup} at 3 Myr and $A_V = 0$ in the AMES-COND isochrone.*

4.2 Kinematic Selection

While in other SONYC surveys this was not the case, here we also use the data from the *Gaia* mission to perform a kinematic study of our CMD-selected sample, helping us assert which constitute probable members of the CrA cloud. As discussed in Section 4.1, complementary methods to the CMD-selection step are needed since contaminants may occupy the same colour-

magnitude space as young low-mass stars and BDs (for example, reddened by the gas and dust present in the SFR). The *Gaia* survey, then, allows us to determine which objects likely belong to the SFR since they will show kinematic properties similar to those of known CrA members. In this section, we first select objects from our CMD-selected sample with *Gaia* EDR3 PMs close to those of spectroscopically confirmed members of CrA. We then take this catalog of PMs-selected sources and reject those with parallaxes which stray from the values usually associated with CrA members. We also want to highlight that not all sources from the CMD-selected sample have *Gaia* measurements, and we make an additional selection of low-mass sources in Section 4.3. Figure 4.4 shows the PMs plot of the CMD-selected catalog and of the spectroscopically confirmed members of CrA. We are looking for objects in the CrA cloud, which will exhibit similar kinematic properties since they were born in the same region. As such, they will share PMs - the projection of their movement on our night sky - and will cluster in the PMs plot. By plotting the PMs of our CMD-selected sample (see Section 4.1; blue and orange dots), we are able to identify objects with PMs close to those of known CrA members. To know the PMs of CrA members, we cross-matched our list of spectroscopically confirmed members of CrA (see Section 2.1.5) with the *Gaia* EDR3 (Gaia Collaboration et al., 2021) catalog. CrA members with a RUWE value > 1.4 (a *Gaia* flag indicating binarity in the source, the presence of a disk, or otherwise resulting in an inaccurate astrometric solution) were removed. The cloud members (green stars) have mean PMs of $\mu_\alpha = 4.24 \pm 1.49$ mas yr^{-1} and $\mu_\delta = -27.74 \pm 0.86$ mas yr^{-1}. A circle was drawn at (4.43, -27.68) mas yr^{-1} (the median PMs of the confirmed members) with a 5.5 mas yr^{-1} radius to encompass all known members of the region. CMD-selected sources inside this region are selected (orange dots), and redirected to the parallax selection. This list (hereafter called CMD+PM-selected) comprises of 19 sources from our IJKs catalog.

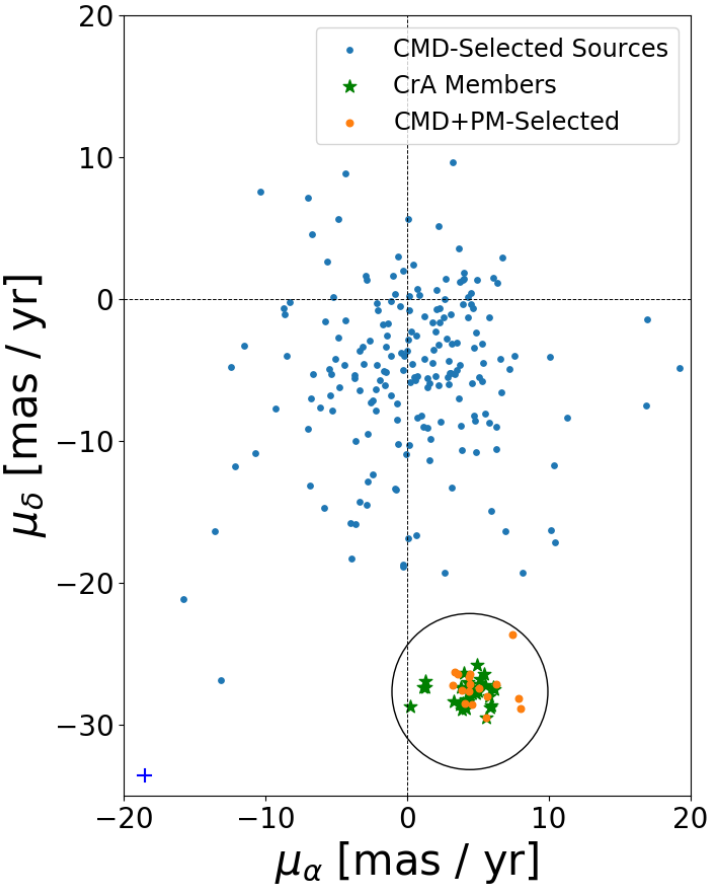

Figure 4.4: *The PMs plot of the CMD-selected sample (blue and orange dots) and of the CrA members (green stars). Members confirmed spectroscopically were used to determine the parameter space pertaining to the CrA cloud. Sources from the CMD-selected sample inside this region (orange dots; the region is delimited by the circle) are selected and redirected to the parallax-selection step. On the bottom-left, the* Gaia *EDR3 average PMs errors for the CMD-selected sample are shown. These errors were enlarged by a factor of 10 for readability.*

In Figure 4.5, the parallaxes of the CMD+PM-selected sample are shown. With this list of CMD+PM-selected sources, the last step is to remove objects which are at a distance from us different from those of CrA members. Spectroscopically confirmed members of CrA are again used to perform the selection (green bars in the left panel). CrA members have a mean parallax of 6.53 ± 0.23 mas (here, the member with a parallax value ∼ 12.5 mas was not taken into account). CMD+PM-selected sources (black bars in the left panel; black dots in the right panel) within a 3 σ deviation (vertical dashed lines) were selected, while sources outside this range were rejected. From the CMD+PM-selected sample, 4 sources were rejected. The end result is a list of sources with colours indicating low-mass and youth, and PMs and parallaxes suggesting cloud membership. This list is made up of 15 sources from the total IJKs catalog of 21 133 objects, and we call it the *Gaia*-selected list since this was the survey used for kinematic selection (Table B.5).

As seen in the left panel of Figure 4.5, one of the objects in our list of confirmed CrA members presents a parallax very deviated from the other members of this region. This source is RXJ1901.4-3422 which was observed spectroscopically and attributed as a member by Neuhäuser et al. (2000). They identify it as a late-F star and comment that the weak lithium strength in its spectra makes it hard to classify the source between a PMS or a ZAMS star. At the time, using parallax measurements from the *Hipparcos* mission (a predecessor to the *Gaia* survey),

they calculated a distance to RXJ1901.4-3422 of 65 pc. This is almost a 100 pc difference from the distance to CrA recently proposed by Galli et al. (2020) (150 pc). Using *Gaia* EDR3 data, we calculate a distance to this source of $\sim$ 80 pc. As it stands, RXJ1901.4-3422 seems to be a foreground star and its membership status should be revisited.

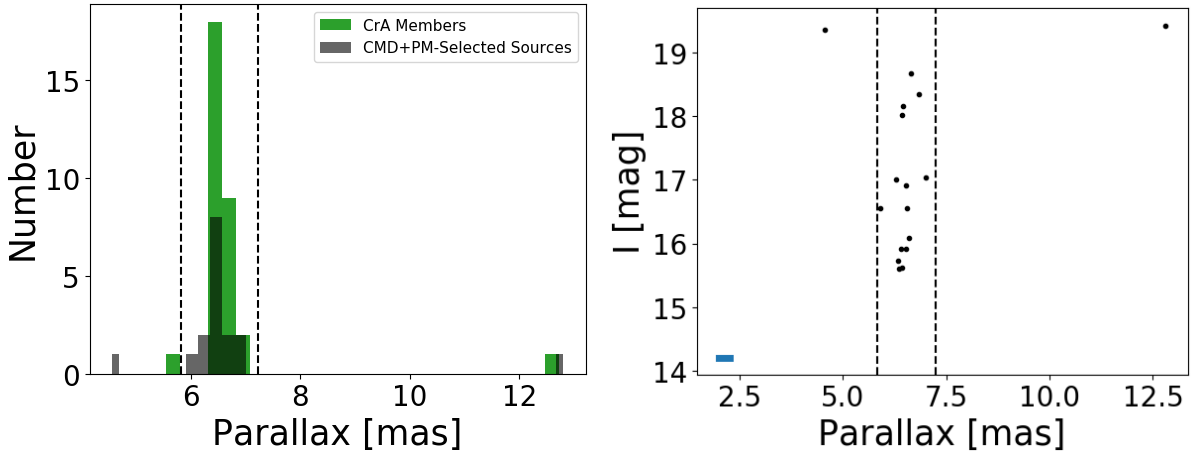

Figure 4.5: ***Left Panel****: The parallaxes histogram of the CMD+PM-selected sources (gray bars) and of the spectroscopically confirmed members of CrA (green bars). CrA members were used to determine the parameter space pertaining to the cloud. Sources from the CMD+PM-selected sample inside this range are selected as probable members of the SFR, while sources outside of it are rejected. One member of the star-forming cloud has a parallax value outside of the space defined by the other CrA members (RXJ1901.4-3422).* ***Right Panel****: A scatter plot of the parallaxes of the CMD+PM-selected sample. The range defined for the parallax selection is delimited by the dotted vertical bars. The mean error for the parallaxes of the CMD+PM-selected sample is shown on the bottom left (blue line).*

Figure 4.6 shows the same (I, $I - J$) CMD of our IJKs catalog (blue, green and orange dots), but this time we overplot the *Gaia* EDR3 catalog to show that our catalog is significantly deeper. *Gaia* sources with both PMs and parallaxes (green dots), as well as those with only PMs measurements (orange dots), only reach up to I $\sim$ 19 magnitudes. This means that only a subset of the CMD-selected sample has PMs measurements.

As mentioned in Section 2.1.6, Galli et al. (2020) determined a list of 313 probable members of the CrA SFR based on their *Gaia* photometry (using the G- and G_{RP}- filter from *Gaia*), PMs and parallaxes. They used a Bayesian inference method using these parameters to infer probable members of the CrA cloud. We check our selection for how many of the DANCe sources also pass our selection methods. In Figure 4.7, we show the same (I, $I - J$) CMD as Figure 4.1, but now we overplot the *Gaia*-selected sources (pink stars) as well as the DANCe sources that pass our selection (or, in other words, that are also present in the *Gaia*-selected list; blue stars). All DANCe sources in our field-of-view pass our selection criteria. A good agreement between our two selection methods makes a great argument for the membership status of these sources. We also note that our selection produces 5 candidates which do not feature in the DANCe catalog.

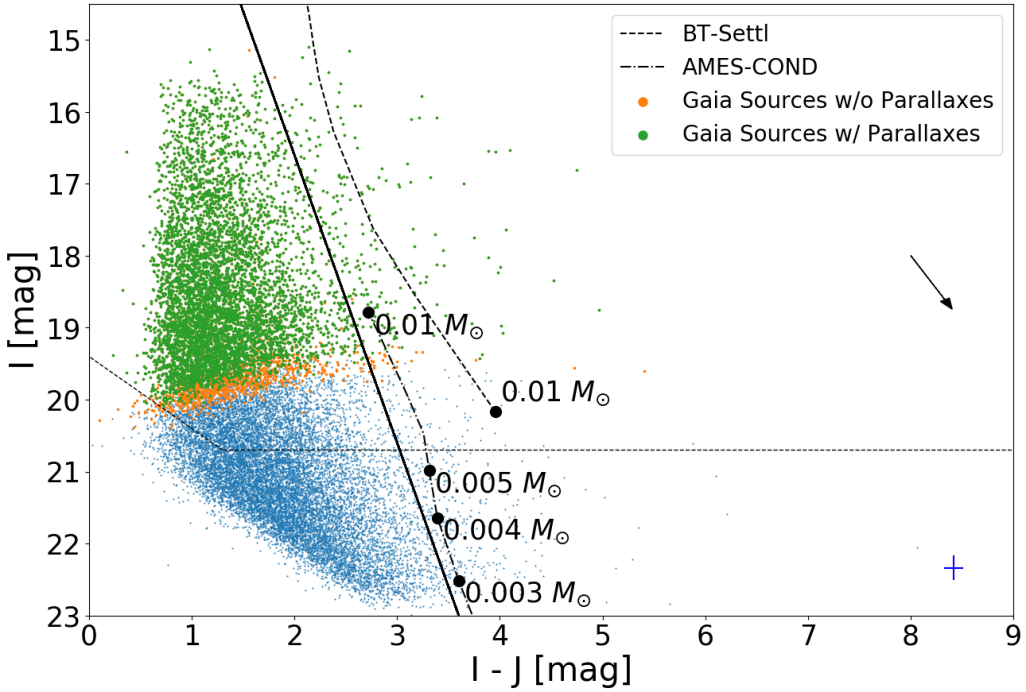

Figure 4.6: *The CMD of our IJKs catalog (blue, green and orange) with their respective* Gaia *cross-matches overplotted (green). The faintest* Gaia *sources do not possess parallax measurements (orange). The black arrow is showing the extinction vector for $A_V = 1$ mag. Our IJKs catalog goes much deeper than* Gaia*, so not all of our sources have PMs measurements. The average errors for each axis are shown on the bottom right (blue lines). Errors for the I-band axis were enlarged by a factor of 5.*

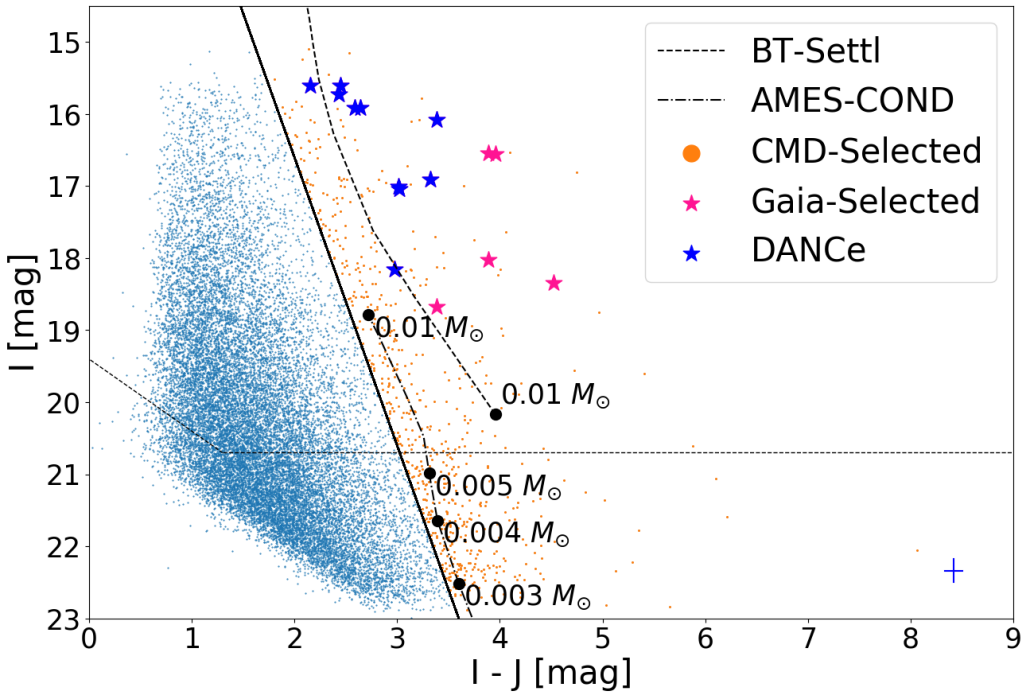

Figure 4.7: *The CMD of our IJKs catalog (blue and orange). Sources redder than the selection line are shown in orange. Sources from our* Gaia*-selected list are shown as pink stars. Sources from the DANCe catalog (Galli et al., 2020) that pass our selection method are shown as blue stars. All DANCe sources in our IJKs catalog pass our selection method. The average errors for each axis are shown on the bottom right (blue lines). Errors for the I-band axis were enlarged by a factor of 5.*

4.3 Faint Sources

In Figure 4.8, we make an additional selection of sources from our IJKs catalog (blue, orange and red dots) with no *Gaia* kinematics from the (I, $I-J$) CMD. Here, sources fainter than the *Gaia* completeness limit (I $\sim$ 19 mag) and above 22 magnitudes in the I-band from our CMD-selected list (orange dots) are selected (red dots). Although we do not know the kinematic properties of these sources, we add them to the final list of candidate sources for follow-up spectroscopy since they show photometry expected for young objects, with masses down to around 4 M_{Jup}. Having a bigger sample of sources to choose from also allows us to observe the maximum number of targets possible during spectroscopy observations. This list contains a total of 313 sources from the CMD-selected sample. Adding to the *Gaia*-selected list, we produce a catalog of 328 candidate sources for follow-up spectroscopy (Table B.6).

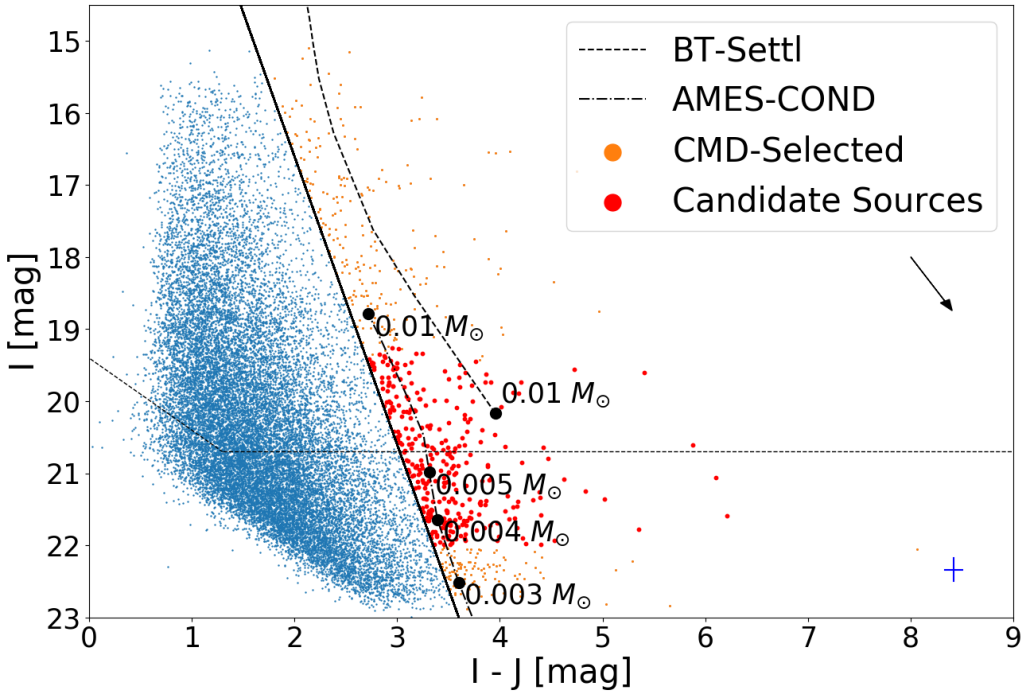

Figure 4.8: *The CMD of our IJKs catalog (blue, orange and red). Sources redder than the selection line are shown in orange. The CMD-selected sources without PMs measurements provided by* Gaia *above I = 22 magnitudes and below the reach of the* Gaia *mission (I $\sim$ 19 mag) were selected for the final list of candidates (red). The black arrow is showing the extinction vector for A_V = 1 mag. The average errors for each axis are shown on the bottom right (blue lines). Errors for the I-band axis were enlarged by a factor of 5.*

4.4 The Final Candidate List

As a result of CMD- and kinematic-selection, a final list of candidates for spectroscopical observations was defined. In Figure 4.9, the distribution of our list of candidates is shown on the CrA field observed by the Suprime-Cam. This list consists of 328 sources with 4 of them being spectroscopically confirmed members of the CrA cloud (confirmed in Sicilia-Aguilar et al. 2008), 10 being part of the Galli et al. (2020) catalog (2 of them being confirmed members of the CrA region) and 15 of them having been selected through *Gaia* PMs and parallaxes. The fainter end of the selection (green), which composes the majority of the list of candidates, are spread throughout the dark cloud of the Coronet Cluster, while the *Gaia*-selected sources

appear around the outskirts of the dark patch (pink). This is because objects embedded in the cloud are too faint to be detected by the *Gaia* spacecraft. The produced list of candidates reaches magnitudes fainter than previous observation efforts, resulting in the deepest look into the CrA region to date with 145 of the candidate sources presenting masses below 5 M_{Jup}, if indeed confirmed as members of CrA.

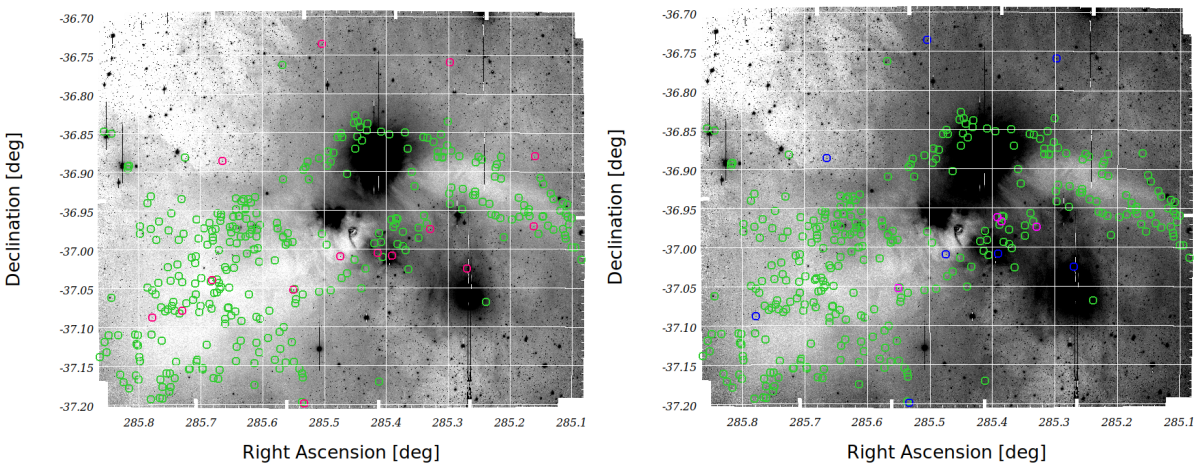

Figure 4.9: ***Left****: The distribution of the candidates for follow-up spectroscopy.* Gaia*-selected sources (pink) are seen in the outskirts of the dark cloud of the Coronet cluster. This is because objects embedded in the cloud are too faint to be detected by the* Gaia *mission due to the high extinction values in these regions. Meanwhile, our selection of faint sources (green) includes objects found in the inner regions of the cloud and constitute the bulk of our list of candidates.* ***Right****: The distribution of the candidates for follow-up spectroscopy. Highlighted here are the candidates which also feature in the DANCe catalog (blue) and those which are previously spectroscopically confirmed members of the CrA SFR (magenta).*

In Figure 4.10, we show the histogram of our list of candidates (black) with two subsets overplotted. We draw the completeness limit of our catalog as well (red dashed line). In the left panel, we highlight the sources from our *Gaia*-selected list (pink) to show just how deep this selection reaches when compared to the overall list of candidates. In the right panel, we plot our list of CrA spectroscopically confirmed members (green). Most of our list of candidates is comprised by the faint sources selected in Section 4.3, and the spectroscopy of these sources will confirm the membership of some of the lowest-mass objects in the CrA region to date. As judged from the previous efforts by the SONYC team, a large fraction of the faint, optically-selected candidates are expected to be contaminants, stressing the importance of additional selection methods, such as the kinematics and follow-up spectroscopy, before reaching any conclusions on the overall population of substellar objects in young clusters and SFRs.

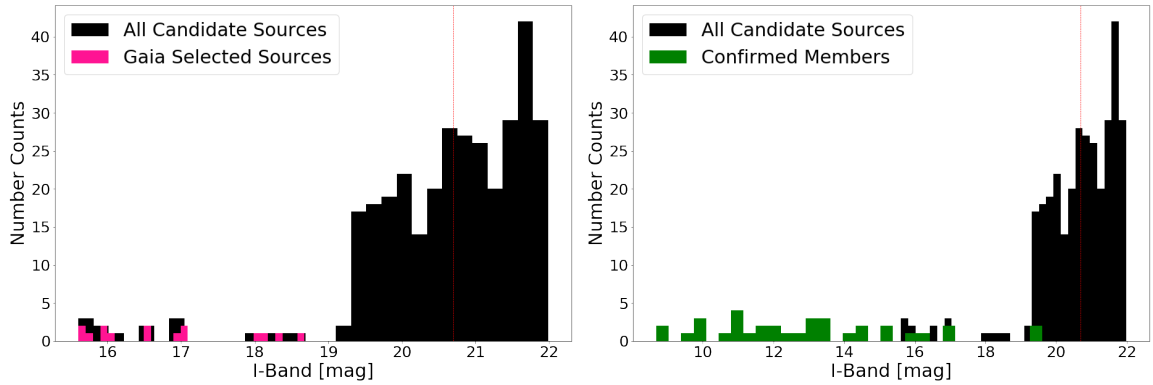

Figure 4.10: *Histogram of our list of candidates (black) with different relevant subsets highlighted on each panel.* ***Left Panel:*** *The* Gaia*-selected sample (pink).* ***Right Panel:*** *The spectroscopically confirmed members of CrA (green).*

4.5 H-Alpha Emission

The Suprime-Cam also observed the CrA molecular cloud using an H_α filter (the N-A-L656 filter, see Table 2.1 in Chapter 2) to look for emission due to accretion from these sources. As discussed in Chapter 2, strong H_α emission is expected from young sources with accreting circumstellar disks (Luhman et al., 2005; White and Basri, 2003; Muzerolle et al., 2000a,b, 2003; Jayawardhana et al., 2002, 2003; Whelan et al., 2005; Joy, 1945). This emission can then be considered a sign of youth, so we look for sources in our list of candidates with bright H_α emission.

In Figure 4.11, we show the $(I - H_\alpha,\ I - J)$ colour-colour diagram of our IJKs catalog (blue and orange dots). H_α measurements were obtained by cross-matching our IJKs catalog with the one produced using the H_α filter. This way, we were able to identify sources with enhanced emissions of H_α lines. Usually, this requires extinction estimates for the sources but, for our colour configuration, the reddening vector is roughly parallel to the locus of the main-sequence sources. Because of this, objects with bright H_α emission do not need to be corrected for extinction to establish their brightness, since they will always stand out from the bulk of the sources. The criteria for an object to be considered a strong H_α emitter is based on a hand-drawn line which follows the main-sequence sources. This selection line is given by:

$$y = -0.5x - 2.35 \tag{4.2}$$

Sources brighter than this threshold (red line) are considered bright H_α emitters (orange dots). These sources were cross-matched with our list of candidate objects for follow-up spectroscopy to check if any of our candidates show enhanced H_α emission. If so, these can be prioritized during observations since they present an extra indicator of youth. We remind the reader that our H_α catalog is not calibrated, and what is shown in Figure 4.11 is the instrumental magnitude of each source plus the ZP of their respective detector calculated when calibrating the W-S-I+ filter catalog. Figure 4.12 again shows the CMD of our IJKs catalog (blue and orange dots), but this time we overplot the sources with bright H_α emission (green and red stars). Not many bright H_α emitters were detected with only three featuring in our list of candidates (green stars).

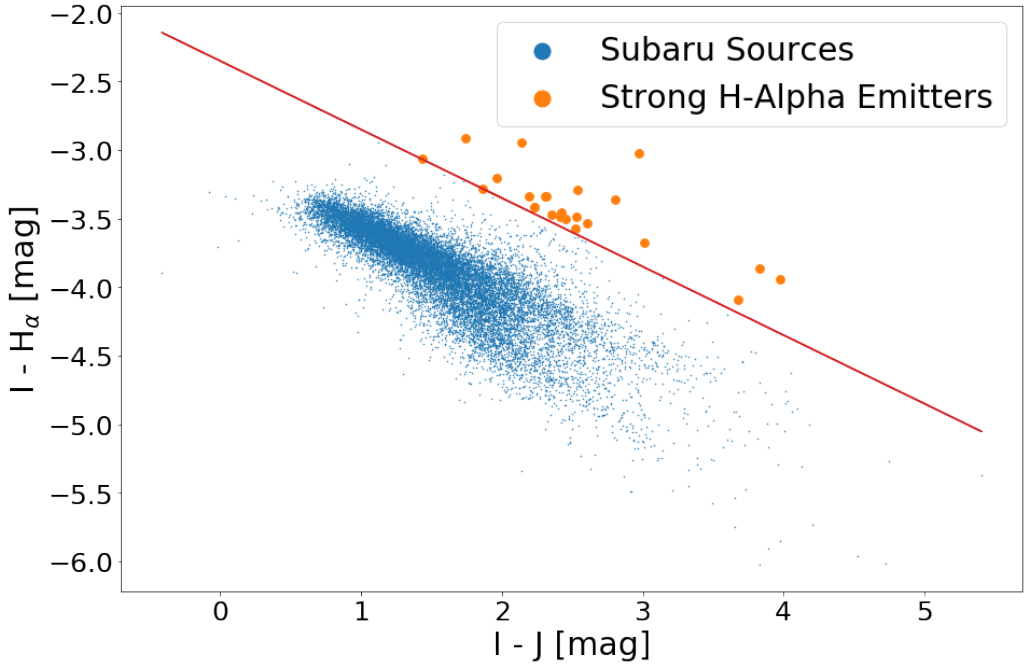

Figure 4.11: *A colour-colour diagram of our IJKs catalog (blue and orange) with H_α measurements from the N-A-L656 filter catalog. Sources with visibly strong H_α emission (orange) are highlighted, as this can indicate youth. The threshold for the selection is based on a hand-drawn (red) line which follows the main-sequence chain.*

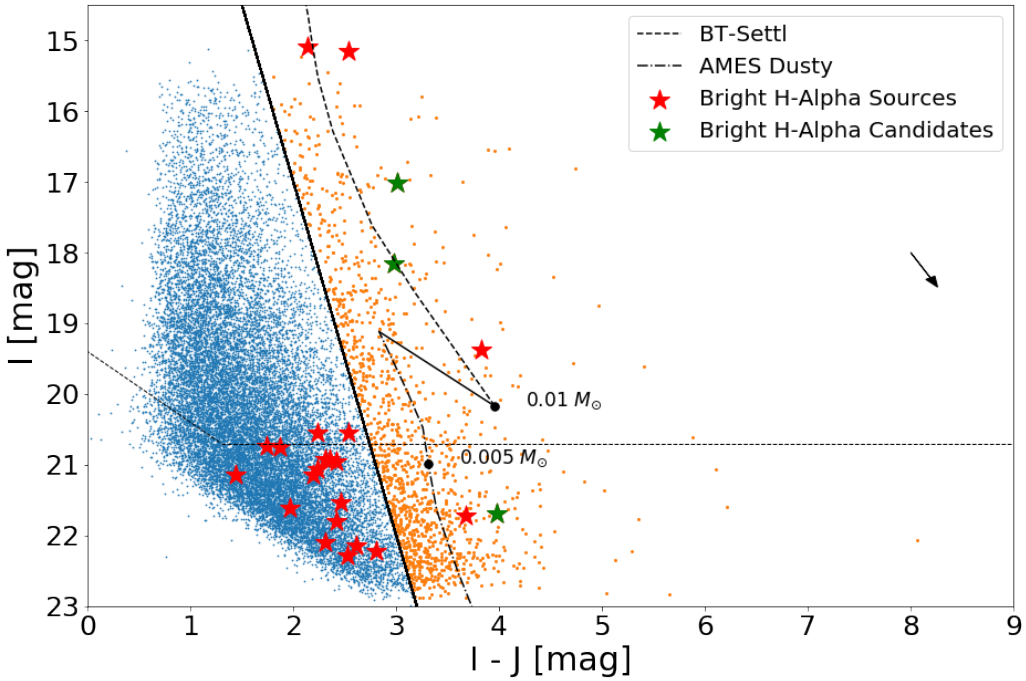

Figure 4.12: *The CMD of our IJKs catalog (blue and orange). Here, sources that present strong H_α emission are highlighted (red stars) along with those that feature in our list of candidates (green stars). The black arrow is showing the extinction vector for $A_V = 1$ mag. The dashed line corresponds to the completeness limit of our sample. The selection line for the CMD-selected sample is shown as a solid black line.*

4.6 Extinction Estimation

Figure 4.13 shows the ($I-J$, $J-Ks$) colour-colour plot of our IJKs catalog (black, green and red dots). In order to estimate the extinction present in the observed CrA field, we use a method similar to that by Pearson et al. (2020). This method is based on using colours with a weak dependence on mass. Since we do not have H-band for our sources, we use a similar colour-colour configuration which preserves the same properties. Two grids of empirical colours were taken from Pecaut and Mamajek (2013) and used to estimate extinctions. These grids provide the expected colours for sources not affected by extinction. One grid provides the expected values for main-sequence objects with spectral types ranging from O9V−M9V (red line). At spectral types $\geqslant$ M0V, a transition sequence can be seen, only plateauing at M8V or greater. An extension of the transition region is also made by fitting a line through the M5V ($I-J=1.774$, $J-Ks=0.891$) and M6V ($I-J=2.243$, $J-Ks=0.957$) spectral types (extended red line). One line is extended by fitting a line parallel to the extinction vector which meets the extended transition line (dot-dashed black line). The second grid gives the expected colours for young sources with ages 5−30 Myr (green line). It was extended by fitting a line through the M4 ($I-J=1.56$, $J-Ks=0.89$) and M5 ($I-J=1.91$, $J-Ks=0.86$) spectral types (dashed green line). Sources from our IJKs catalog were then translated along the de-reddening vector ($R_\nu=3.1$; Cardelli et al. 1989; black arrow) until they would reach the (red dots) main-sequence or (green dots) young grid of empirical colours. The amount of translation needed to move a source until it would meet one of these grids provides the extinction estimate for each individual object. We estimate the extinction for 6 990 sources (143 were de-reddened to the young empirical colours; 6 847 were de-reddened to the main-sequence empirical colours).

Using the produced extinction values for the 6 990 sources, we built an extinction map of the field observed by the Suprime-Cam (Figure 4.14). We divided our field-of-view into a grid of 20 $\times$ 20 to create a colour map of the observed region. An extinction is attributed to each grid cell by averaging the extinction estimates of all sources present within a cell. For cells with $<$ 10 sources, the attributed extinction is the average of the surrounding cells (in the case of a cell outside of the cloud) or a random value ranging $15-30$ mags (in steps of 1 mag) for cells in the innermost part of the cloud. There is a clear extinction gradient towards the inner region of the cloud where extinction values can reach up to $A_V=13$ magnitudes, but a lack of sources in this inner region is consistent with even higher extinction values in the densest cloud regions of CrA.

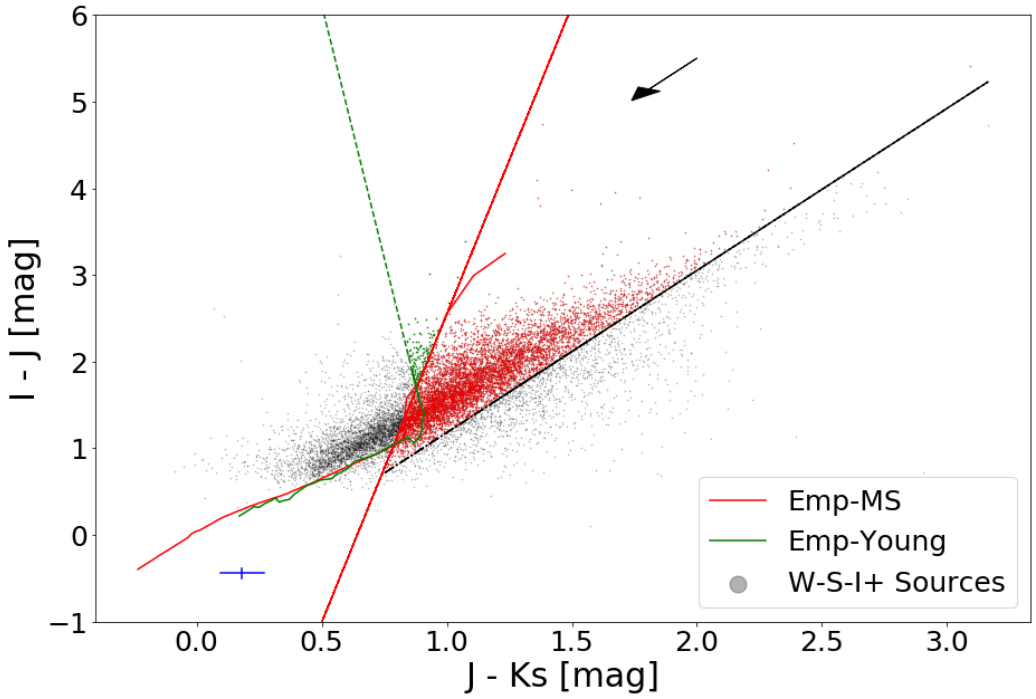

Figure 4.13: *The colour-colour diagram of our IJKs catalog (black, green and red dots) used to estimate extinction. Two grids of empirical colours from Pecaut and Mamajek (2013) are used to estimate the extinction for our sources. One grid depicts the expected photometric values of main-sequence dwarfs (solid red line). This model shows a steep transition at $J - Ks = 0.7 - 1.2$ magnitudes which was extended (dashed red line). Outside this range, we approximated the grid to one line which represents the early-type regime of the grid (up to O9; dot-dashed black line). Another model represents the expected colours for 5 − 30 Myr sources (green line) which was also extended (dashed green line). Extinction was estimated for each source by measuring how much a source needed to move to reach its respective model. Sources deviated to the main-sequence empirical model are shown in red, while sources de-redden towards the model for young objects are shown in green. The arrow shown in the figure represents the direction of the de-reddening vector with $A_V = 1$ magnitude. The average errors for each axis are shown on the bottom left (blue lines).*

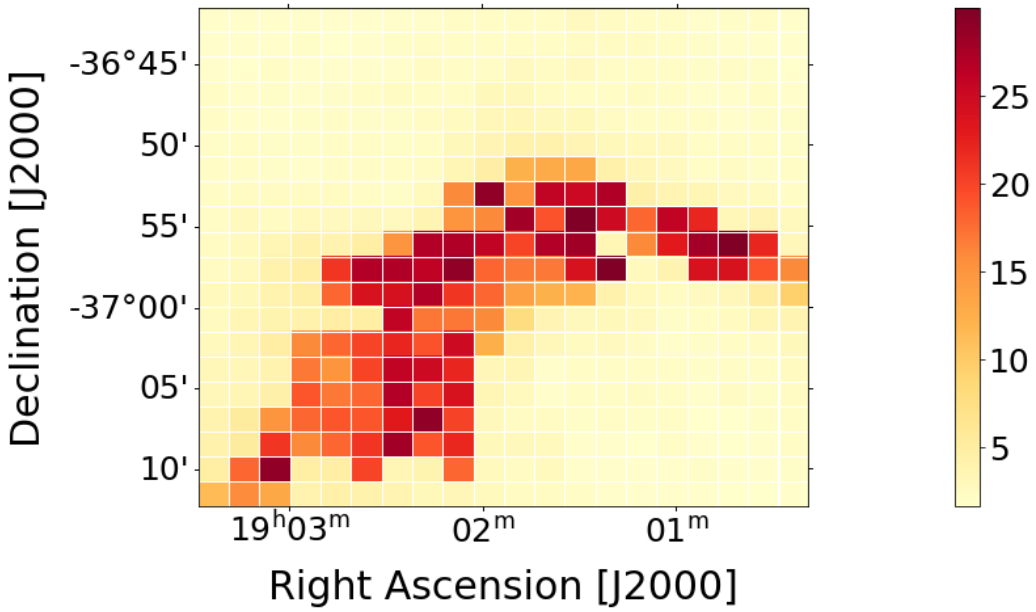

Figure 4.14: *The extinction map of our field-of-view produced by averaging the extinction estimates of the sources in each cell. Undersampled cells were attributed an average extinction of the surrounding cells (for the case of cells outside of the cloud) or a value between 15 and 30 mags (in steps of 1 mag) for cells in the cloud.*

4.7 Contaminants

To predict the number of contaminants in our list of candidates, we use the *Besançon* galaxy model[2] which simulates the Milky Way and provides information about the objects expected to be found on a given direction of the sky. We ran the model using the center of our field-of-view ($\alpha \sim 285.47$, $\delta \sim -36.95$) across an area of ~ 0.55 deg^2. We defined objects with magnitudes $13 < \mathrm{I} < 23$, $10 < \mathrm{J} < 21.5$ and $9 < \mathrm{K} < 19$, and with colours $-0.5 < \mathrm{I} - \mathrm{J} < 0.5$ and $-1 < \mathrm{J} - \mathrm{K} < 2.8$. By plotting the magnitude errors against the magnitude of each source, we constrained the parameters of the error functions. These are exponential functions given by:

$$\Delta I = 0.0534 + exp(1.233I - 30.495) \tag{4.3}$$

$$\Delta J = 0.0039 + exp(0.960J - 20.566) \tag{4.4}$$

$$\Delta K = 0.0002 + exp(0.904K - 17.899) \tag{4.5}$$

The output of the model was a catalog containing the sky position, I, I − J and I − K magnitudes and associated errors of 52 745 simulated objects. Extinction still needs to be applied to the model, so we used our extinction map and the sky positions of the sources in the model to estimate the extinction of each one. In Figure 4.15, we plot the (I, $J - Ks$) CMD of our IJKs catalog (blue dots) and of the *Besançon* galaxy model catalog (orange dots). We divide the CMD into grids of 0.2 × 0.5 mags. Then, we iterate over each grid cell. In each cell, we check if the number of sources from our catalog is higher than the number of sources from the model. When this happens, we randomly select the excess sources from our IJKs catalog in the grid cell (purple dots). By doing this over the entire CMD, we determine the number of contaminants in our list of candidates. From an initial catalog of 313 sources (see Section 4.3), only 30 sources survive the random-rejection process. This means our list of candidates shows a contamination rate of $\sim 90\%$ and that we expect to confirm around 30 new free-floating planetary mass objects. Only ~ 100 of this type of objects are known so far, meaning we may increase this sample by 30%.

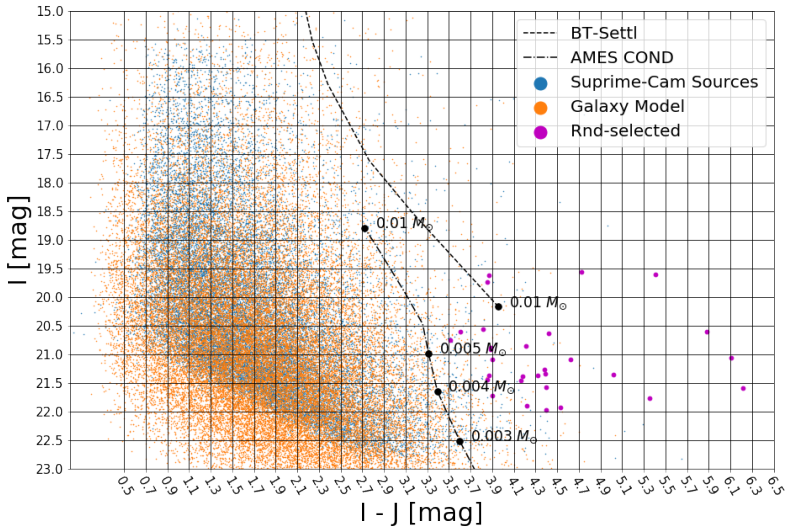

Figure 4.15: *The CMD of our IJKs catalog (blue) and of the* Besançon *galaxy model catalog (orange). Extinction was applied to the galaxy model using our extinction map. Grid cells with more sources from our IJKs catalog than those from the model catalog indicate the presence of probable members (purple). This way, we can predict the contamination rate of our list of candidates.*

[2]https://model.obs-besancon.fr/modele_home.php

Chapter 5

Planning the Follow-up Spectroscopy

In previous SONYC works, it became clear that spectroscopy is the most reliable way to determine the membership and nature of candidate young objects of an SFR (it allows us to estimate effective temperatures from model-fitting, which also gives us an idea of the mass of the object). This is specially true for sources with no kinematic data available (i.e. the faintest objects in our list of candidates). It is in this fainter regime that we expect to detect most of our contaminants, but it is also here that we will find the objects we are most interested in - low-mass and planetary-mass BDs. Having constructed a list of candidate objects for follow-up spectroscopy from a dataset of the CrA cloud, we narrowed down the sample of objects to be considered for future observations. This helps reduce the required time for observations, while at the same time raising the probability of detecting young BD sources belonging to the CrA cloud. Still, observing all of these sources is not a realistic prospect due to time constraints from the observatories. In this chapter, we introduce the instrument with which we will make the spectroscopy observations. We propose 7 field-of-views of follow-up spectroscopy observations on the CrA field observed by the Suprime-Cam. We also determine the exposure time of these observations and make all the necessary preparations using the appropriate software. This allows us to calculate the total amount of telescope time we will need to observe our targets.

5.1 KMOS

The KMOS (Sharples et al. 2013) is an instrument installed at the VLT in the Atacama desert in Chile. It is designed to perform integral field spectroscopy − a technique capable of producing spectra across a given wavelength range for a single pixel in an image. It has twenty-four arms which share three different grating units (Figure 5.1) and make it possible for KMOS to do integral field spectroscopy of up to 24 different objects across a 7.2′ patrol field. Each arm has a 2.8 x 2.8 square arc-second field-of-view. The spectra captured by each arm are divided into fourteen slices. The KMOS instrument operates in the NIR with a full coverage ranging 0.78 − 2.5 μm. KMOS possesses a spectral resolution of R $\sim$ 1500 − 2500 for the combined H + K band and has a low-resolution mode for this band as well. For the work of this thesis, the KMOS is a great choice for follow-up spectroscopy observations since low-mass BDs are brightest in the NIR, and it is also here that the spectra of these objects is easy to distinguish from those of stars (even at low-resolution). Our list of candidates is comprised of a few hundred objects, so the multi-object spectroscopy capabilities of KMOS are very welcomed. The object density fits

the capabilities of KMOS very well, too. We also choose KMOS due to not only its integral field spectroscopy module and moderate-resolution, but also due to the high SNR which is projected to have at the magnitude regime of our candidates (see Section 5.1.2). KMOS allows astronomers to probe embedded regions of star-forming clouds and detect low-mass sources in these regions. Recently, Fiorellino et al. (2021) were able to study young low-mass stars (with masses down to 0.10 $M_{\odot}$) in fields with visual extinction values up to 28 magnitudes in the NGC1333 cloud thanks to observations made using the KMOS instrument. Pearson et al. (2021) also used KMOS when performing observations of the NGC 2264 cluster. Their selection for spectroscopy targets was also (partially) based on optical spectroscopy, with their candidates ranging I = 17.5 − 21 mag. They obtained spectra for 68 sources, confirming 13 BDs in the region and deriving a slope for the substellar mass function of $\alpha = 0.43$, which is consistent with other observed young clusters − suggesting a universal substellar mass function. In Table 5.1, the different bands available for the KMOS instrument can be found along with their specifications. We will make our observations in the H + K band, which has a resolving power $R \sim 2000$. We choose this band since it encompasses important spectral features found in young BDs (see Section 1.5.1).

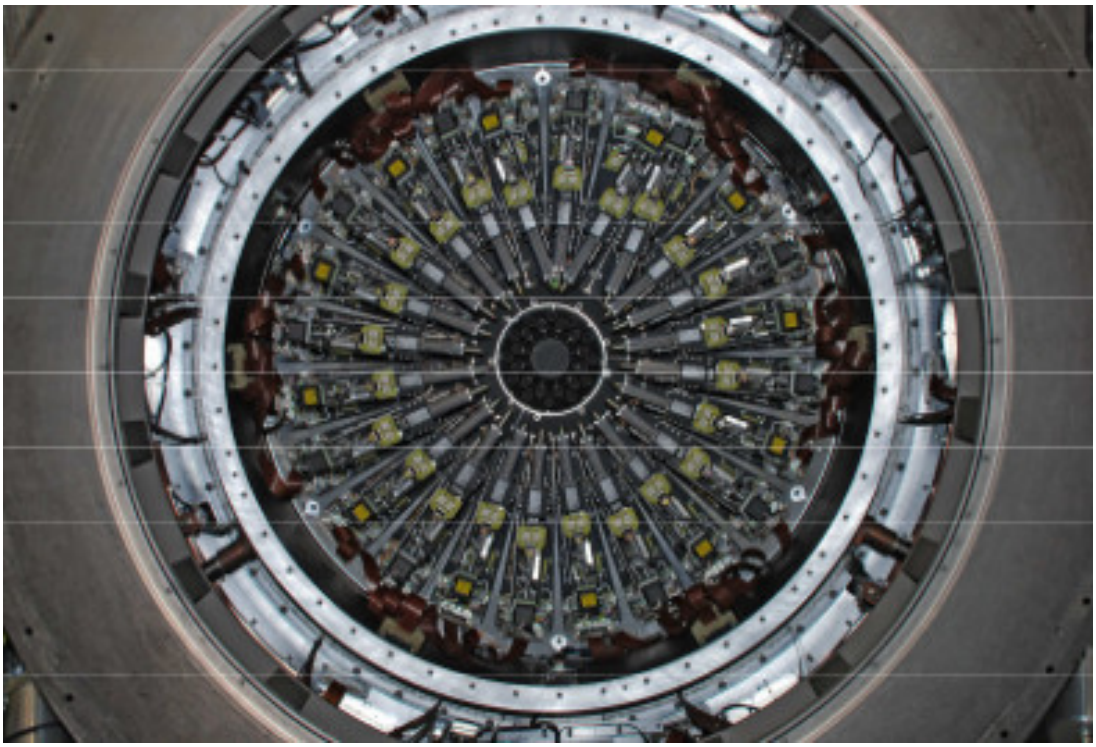

Figure 5.1: *The KMOS instrument is composed of twenty-four different arms, each with its own integral field unit spectrograph. Credit:* https://www.eso.org/sci/facilities/paranal/instruments/kmos.html

Table 5.1: *The bands available at the KMOS instrument and their specifications.*

Bands	Wavelength Coverage (μm)	Pixel Scale (nm/pixel)	Resolving Power (Band Centre)
IZ	0.779 − 1.079	0.143	3406
YJ	1.025 − 1.344	0.165	4045
H	1.456 − 1.846	0.203	3582
K	1.934 − 2.460	0.266	4227
HK	1.484 − 2.442	0.489	1985

5.1.1 KMOS Field Positions

We define 7 different KMOS field configurations for the follow-up spectroscopy observations. The positions of these fields were chosen by prioritizing the observation of the maximum number of targets per exposure while assuring the presence of a nearby telescope guide star. The observation of some regions of the field is not feasible exactly because there are no available telescope guide stars due to the high extinction present in these regions. Across all 7 fields, there are a total of 219 sources from our list of candidates. An overview of the proposed field-of-views can be found in Table B.7. In Figure 5.2, we project these fields (red circles) onto the mosaic of the W-S-I+ filter. They were labelled fields−A through −G, from left to right. They follow the trail of the cloud since here is where the majority of our candidates reside (green circles are candidates from the list of faint sources; pink circles are candidates from the *Gaia*-selected list). Guide stars (yellow circles) in the field-of-view of the Suprime-Cam observations are also shown.

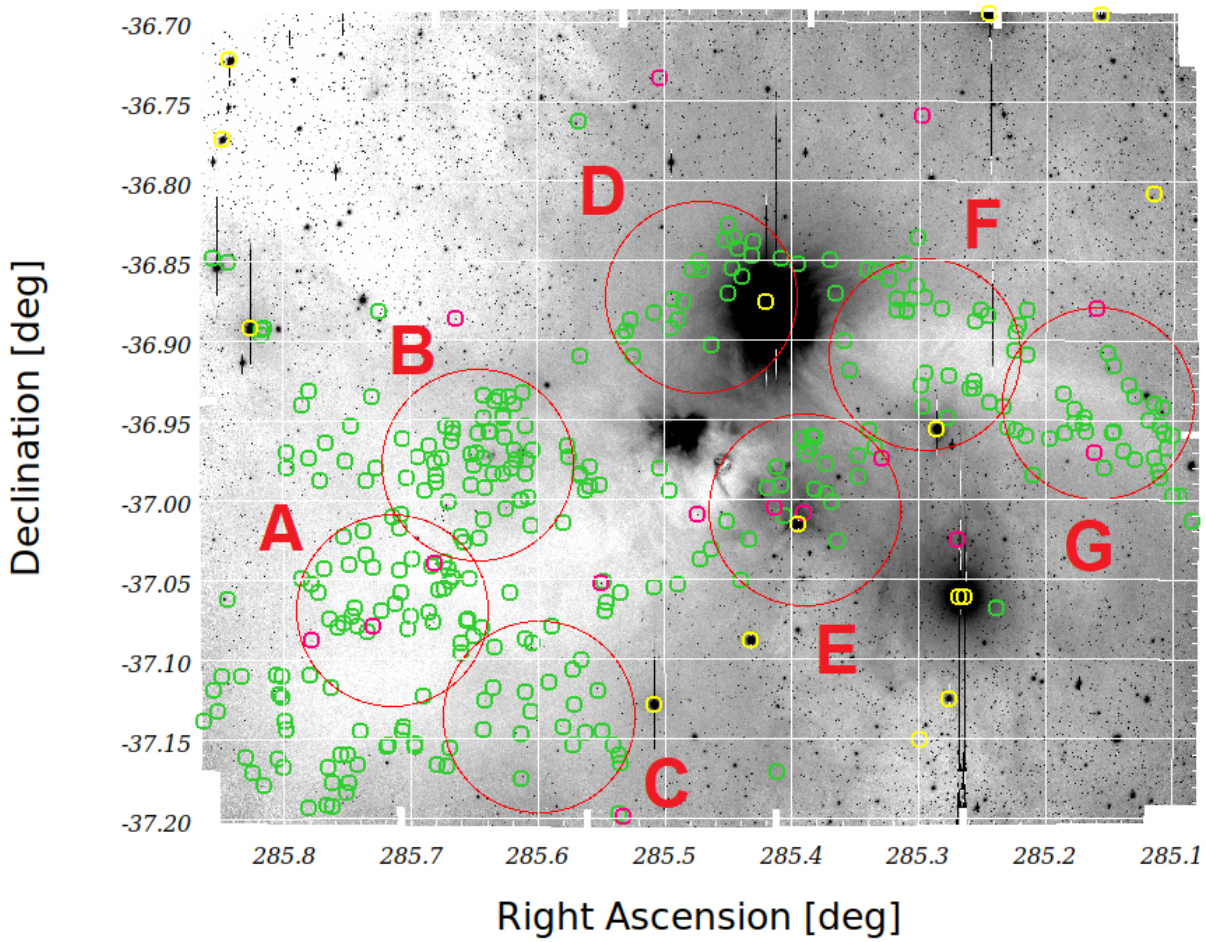

Figure 5.2: *The projected observations of the CrA SFR using the KMOS instrument at the VLT. The red circles projected onto the cloud correspond to the field-of-view of a KMOS observation, with a diameter of 7.22 arc-minutes. Green circles are candidate sources from our list of faint sources. Pink circles correspond to sources from our* Gaia*-selected list of candidates. The yellow circles indicate guide stars available to be used during exposures.*

5.1.2 Estimate of the Exposure Time

To estimate the required observation time for spectroscopy, as well as to build a SNR profile of the KMOS instrument, the Exposure Time Calculator (ETC[1], Version P106.3) provided by the European Space Observatory (ESO) website was used. This tool is able to calculate and plot the expected SNR across a range of magnitudes for a given wavelength band of the KMOS. The SNR profile was built across the range of K-band magnitudes of our list of candidates (Figure 5.3). This simulation assumed an airmass of 1.5. We used the H + K grating and a turbulence of 70% (corresponding to a seeing $\leq$ 1.0"). The SNR profile generated with each simulation was averaged in each band (H-band: 1481 $-$ 1800 μm; K-band: 2000 $-$ 2300 μm) and we plot the results in Figure 5.4. We set one magnitude steps from K = 12 to K = 19 using different configurations for the exposure time and number of exposures. When comparing the predicted SNR with the one obtained from real data, Almendros-Abad (priv. comm.) finds that the ETC predictions are reliable above a certain threshold, determined to be 15 in the H-band and 8 in the K-band (dashed blue line). For the faintest sources in our list of candidates (K $\sim$ 17 mag), the expected SNR is fairly above these values for long exposure times ($t >$ 90 seconds).

We also inspected the results of these simulations to choose an exposure time which gives a good SNR without risking the saturation of the detectors. Sky brightness in the IR changes on minute scales, so sky observations cannot be too spaced from each other. To understand when optical effects start being significant during observations, we set the ETC to also produce the spectra of a given simulation. Figure 5.5 shows the spectrum (object + background; black) produced by one of the simulations, where we found that persistence issues start to come up for objects with K $\leq$ 12 magnitudes for exposure times $t \geqslant$ 70 seconds. Persistence is an effect caused by the prolonged exposure of the instrument to a brighter source, leading to the saturation of the detector which, depending on the brightness of the source, may not fade away before the following exposures are made (orange dashed line). OH emission lines in the H-band of the produced spectra are above this effect and thus would be affected. We could choose exposure times shorter than 70 seconds, which would allow us to keep bright sources in our observations, but then a lot of time would be spent during the readout phase. This means we would not reach the desired SNR which would be specially crucial for the faintest sources in our list of candidates. As such, we removed all sources brighter than 12 magnitudes (red dashed line in Figure 5.3) in the K-band from the list of candidates for spectroscopy observations. These correspond to 10 sources. 5 other sources lack photometry in the K-band and were thus also excluded. The maximum intensity at the central pixel per exposure is also shown in Figure 5.5 (blue dashed line). By the end, we decided to perform observations using ten 120-seconds exposures, which is expected to produce a SNR of $\sim$ 30 in the H-band and of $\sim$ 10 in the K-band for the faintest sources in our list of candidates (K $\sim$ 17 mag) which, at a distance of 150 pc and using the AMES-COND model, corresponds to an object with mass $\sim$ 7 M_{Jup} (not accounting for extinction).

[1] https://www.eso.org/observing/etc/bin/gen/form?INS.NAME=KMOS+INS.MODE=lwspectr

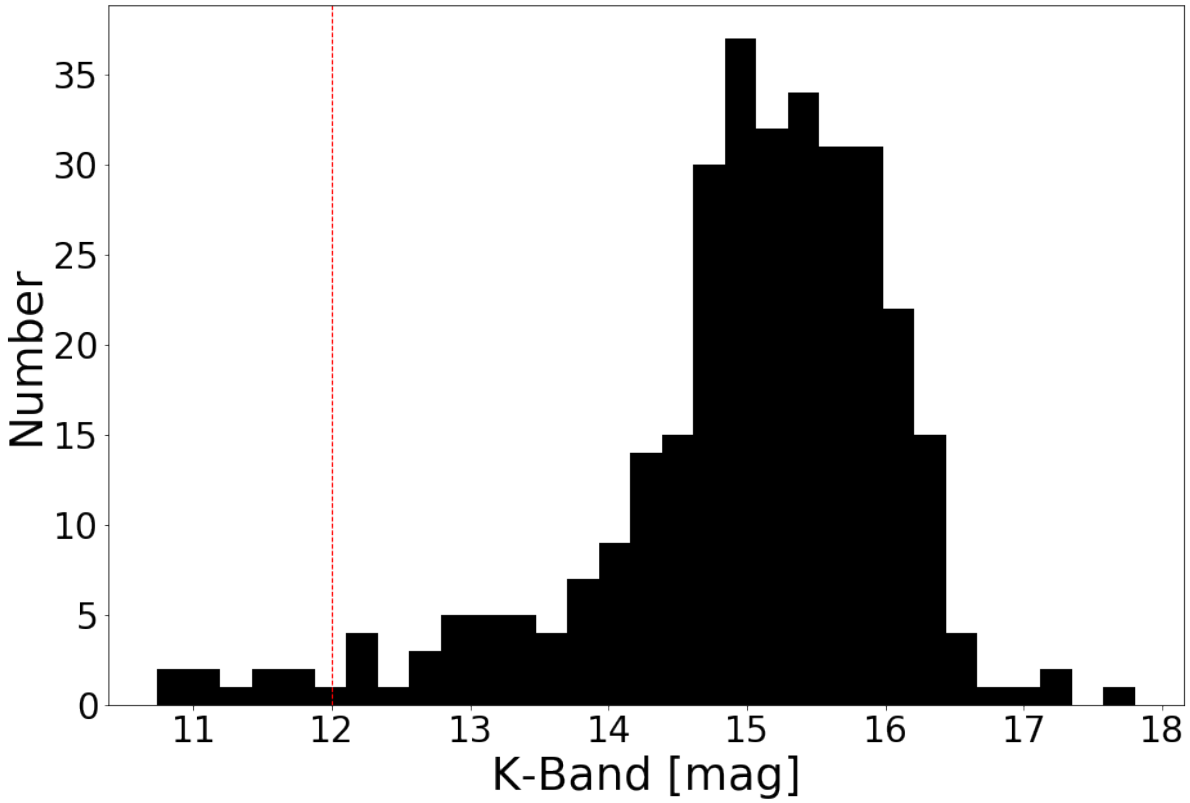

Figure 5.3: *Histogram of the K-band magnitudes of the sources in our list of candidates for follow-up spectroscopy. The red dashed line indicates the cutoff threshold (K = 12 mag) for sources where persistence is expected to become significant.*

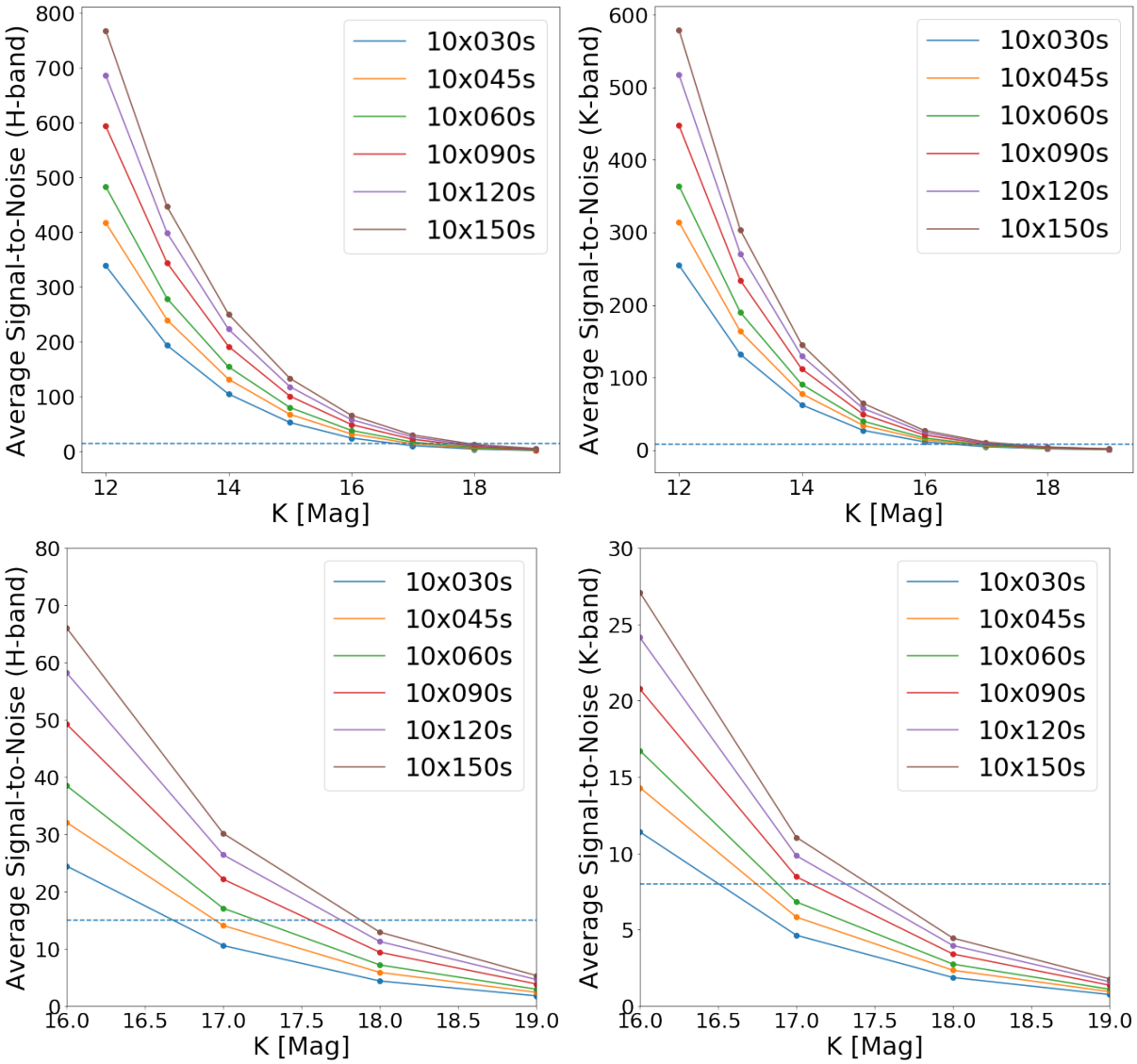

Figure 5.4: ***Top Left Panel****: The expected SNR in the H-band for sources across a range of K-band magnitudes using the KMOS instrument.* ***Top Right Panel****: The expected SNR in the K-band for sources across a range of K-band magnitudes using the KMOS instrument.* ***Bottom Left Panel****: Top left panel zoomed-in at the faintest magnitudes [16−19 mag] of our list of candidates.* ***Bottom Right Panel****: Top right panel zoomed-in at the faintest magnitudes [16−19 mag] of our list of candidates.*

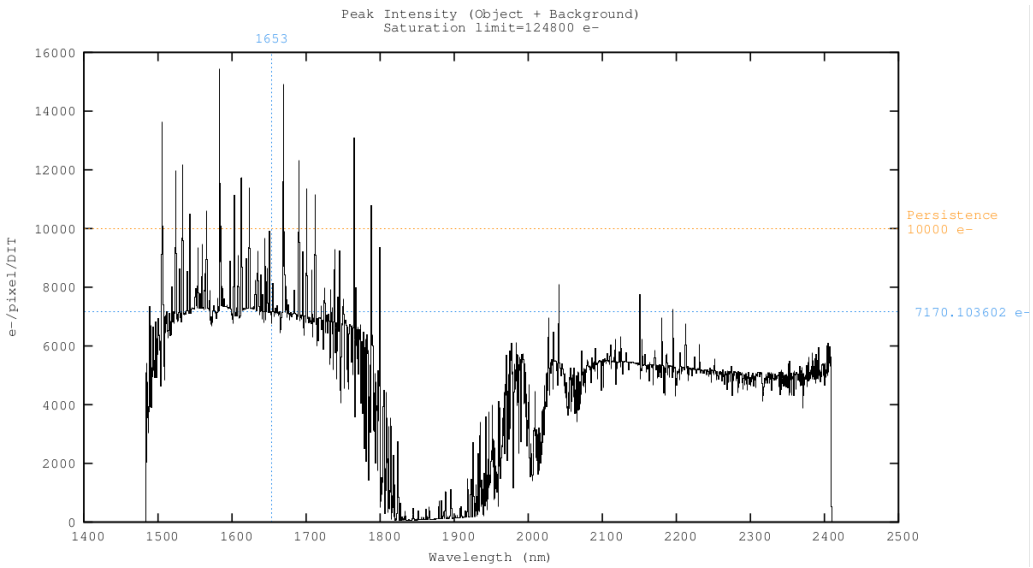

Figure 5.5: *Spectra from one of the simulations using the ETC provided by the ESO website. Persistence shows up for magnitudes 12 or lower in the K-band when using the KMOS instrument. This effect spoils the following exposures and is taken as a reference value to discard bright sources which can lead to its occurrence.*

5.2 KARMA

Observations using the KMOS instrument are prepared using the KARMA software (Wegner and Muschielok, 2008). KARMA is based on the ESO Real Time Display package and aids the user in finding the best configuration for each of the individual arms of the KMOS instrument during observations. It takes into consideration both the targeted sources as well as the mechanical and optical constrains which may arise during observations, and the presence of bright sources and of guide stars in the field (see below). In order to do this, KARMA must be fed a specially prepared catalog with the coordinates of the field-of-view of the observation, the positions of the sources which will be observed, as well as a list of reference targets and guide stars, their magnitudes and bands.

5.2.1 Observing Modes

The KMOS instrument provides three different observing modes: nod-to-sky, stare and mosaic. The first two differ only on the way sky observations are made. The last one allows for a contiguous region of the sky to be captured. We are only interested in particular sources and not the entire region, hence this last method is discarded. For our observations, we chose to use the nod-to-sky mode.

Nod-to-Sky Mode

When using the nod-to-sky mode, two configurations are used for science and sky observations. Sky observations are done by offsetting the instrument in a translational and/or rotational manner, whilst preserving the positional arrangement of the arms. In this mode, arms which start-off observing a science target can then be used for sky observation after performing the offset. KARMA then optimizes the best arm allocation setup possible so that the maximum number of sources are observed during each exposure. Nod-to-sky also has the benefit of the

possibility to allocate two different arms for a same science target (one used during the science and one during the sky observation stage). This will maximize the data that is collected from a target source, making it the preferred mode for observations of less than twelve target sources. One should keep in mind that each arm is different and, thus, there could be a coordinate offset between the two arms and this technique should be used mostly for very bright objects.

Stare Mode

When using the stare mode, rather than performing two individual observations for science and sky, the telescope is set to stay fixed at a target region. Some arms are then allocated for science observations while others are used for sky collection. We did not choose this mode since the sky measured by one of the arms would be affected by the characteristic bias of the integral field unit of that arm and, thus, the sky subtraction performed on the science targets would not be fully accurate because these would have been captured by different arms.

5.2.2 Arm Allocation

The KMOS instrument has 24 arms which need to be allocated during observations. Each arm is delegated for both science and sky observation, since we will be using the nod-to-sky mode. During the KARMA setup, we need to instruct both science and sky configurations, separately. In Figure 5.6, we show our configuration for the science (top panel) and sky (bottom panel) steps for field-A (see Figure 5.2). Sources in our field-of-view are allocated to the arms of KMOS and are shown on the right wing. There is a physical off-set between both observations which guarantees that, during the sky observation, arms are allocated to blank, empty spaces with no interference from a nearby source for the best sky data possible. These empty fields are shown on the right wing of the bottom panel. For field-A, KARMA successfully allocated 23 arms, each targeting a different source.

During this time, we also define the configuration for the *acquisition* step. The acquisition refers to the alignment of the instrument and telescope right before observations. The catalog fed to KARMA possesses reference targets which are briefly observed so the instrument control software can correct the positions of the instrument and the telescope. The reference targets are sources with a J-band brightness of $8 < J < 14$ magnitudes. These can be sources from our list of candidates but, to obtain a higher sample, we also took sources from a cross-match between the VHSDR6 (McMahon et al. 2013; providing magnitude measurements in the J-band) and *Gaia* eDR3 (Gaia Collaboration et al. 2021; providing PMs for these objects) catalogs, allowing a separation between matches < 1". Analogous to the arm allocation process for the main observations, arms are allocated to the reference targets and then offset to sky, separately.

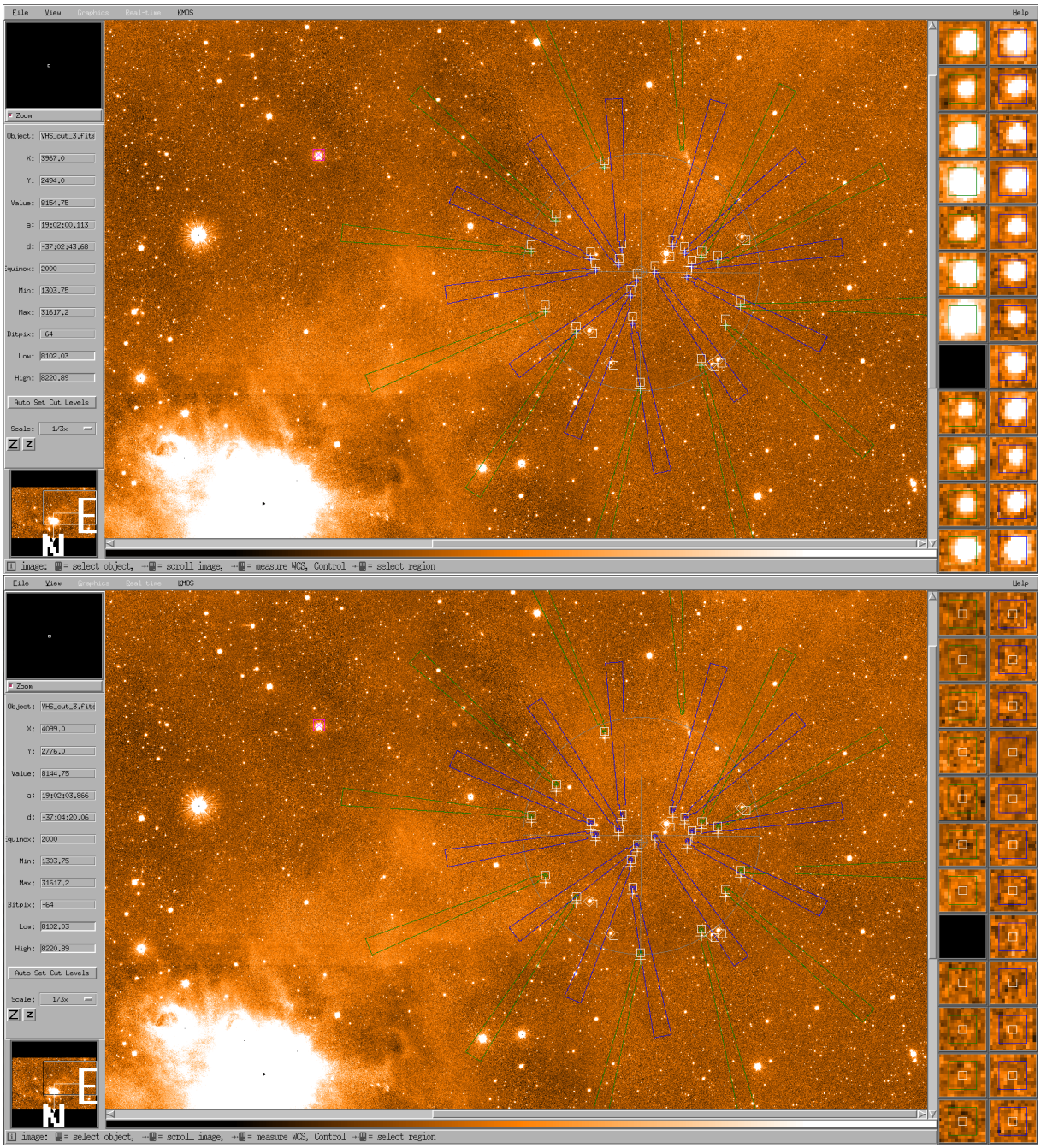

Figure 5.6: ***Top****: Observation setup for the science targets.* ***Bottom****: Observation setup for the sky background. For sky background, we must make sure no nearby sources are possibly contaminating the pixels of the blank, empty spaces on the sky.*

Guide Stars

A list of guide stars is also provided in the catalog fed to the KARMA software. Guide stars are tracked by a guiding system at the telescope to keep track of the target sources it is observing. Because the guiding system can cast a shadow on the telescope during exposures, these guide stars must be at a minimum distance from the field being observed plus a margin. This is why guide star selection is only made at the later stages of the KARMA routine when the science and sky fields have been defined. There is also an upper limit for the distance a guide star can be from the center of the field-of-view. This limit accounts for the wavefront sensing quality

of the guiding system, since this decreases the further away a star is from the telescope optical axis. These limits are calculated by KARMA automatically. As recommended by the KARMA user manual, guide star sources should be brighter than 12 magnitudes in the R-band. By cross-matching the USNO-B1 Catalog (Monet et al. 2003; providing magnitude measurements in the R-band) with the *Gaia* EDR3 catalog (Gaia Collaboration et al. 2021; providing PMs for these objects), allowing a separation between matches < 1", we created a list of candidate guide stars around our proposed fields. KARMA then determines which guide stars can be used during observations, and we can select up to 5 sources to be considered by the telescope operator during observations. Some parts of the cloud are inaccessible due to a lack of guide stars because of the high extinction values present in these regions.

This concludes the KARMA routine. These steps were repeated for each of the 7 proposed fields. The final product (for each field) is a file where all this information is stored - telescope position, arms allocation, reference stars, guide stars, etc. -, which is fed to the *p2 tool* (see below).

5.3 The p2 Tool

The file produced by the KARMA program is used to estimate the total time of observation required. This file is fed to the *p2 tool*[2], provided by the ESO, which allows astronomers to estimate the times for the different exposures as well as for the necessary overheads. Overheads is the total time used to move the telescope and/or its arms between observations, to perform the acquisition of science targets, offsets or readout. We must also decide in what sequence we want to alternate between science (A) and sky (B) positions. We decided to use an ABAABA method. Using this configuration, sky observations are made every two science exposures, reducing the amount of time spent observing sky (thus increasing the amount of time spent observing science targets) while obtaining the same results.

In Figure 5.7, we show the interface of the *p2 tool*. First, we input the target for our observations (a) which is set to the center of the field. We then add templates (b) to the observation description tab. In the acquisition template (c), we specify the integration time as well as the number of integrations during acquisition. We also choose the grating we want to use and upload the file produced by KARMA for a given field-of-view (d), which interacts with the *p2 tool* to provide the details of our observations, as configured during the KARMA simulation. We set up a free-dither observation template (e) using an ABAABA science-sky acquisition setting. Here, we also set the exposure time and number of exposures for our science and sky observations. Lastly, we run the *p2 tool* (f). We did this for each one of our 7 fields-of-view. Each of the proposed observations (see Figure 5.2) is estimated to take around fifty-five minutes, with all seven observations resulting in a total observing time of six hours and twenty-five minutes.

[2]https://www.eso.org/p2

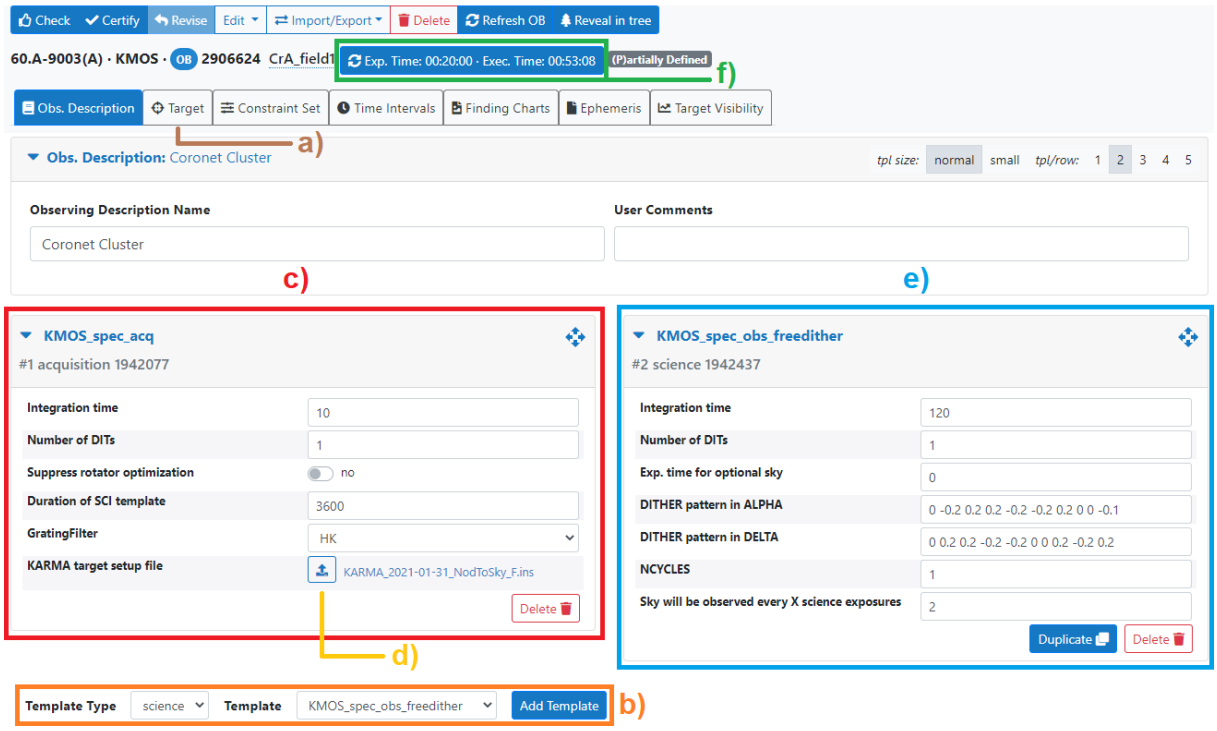

Figure 5.7: *The* p2 tool *calculates the total time of observation required to execute a set of instructions for a given instrument/telescope setup. Highlighted are the relevant sections of the application: a) Sets the target for our observations; b) Adds templates to the simulation; c) Settings for the acquisition step; d) Here, the file produced during the KARMA routine is uploaded; e) Settings for the science and sky exposures; f) Runs the simulation. This was done for each of our 7 proposed fields-of-view, accounting for a total observing time of six hours and twenty-five minutes.*

Chapter 6

Summary

BDs are substellar objects which did not accrete enough matter during their formation to be able to start burning hydrogen in their cores to counteract gravitational collapse, and are instead supported by electron degeneracy. Their masses can reach values in the planetary regime and, thus, the study of these objects is a window for both star- and planet-formation and evolution. Still, little is known about them. Because they have very low masses, they are very faint and, so, harder to detect. Also, in order to observe these sources at the early stages of their lives, attention must be turned to SFRs − stellar nurseries where young objects can be found still in their infancy. Therefore, efforts to map the substellar regime of these star-forming clouds are an important and required step to develop our knowledge of both star- and planet-formation processes, as well as to constrain the substellar IMF. The SONYC survey is working to produce a complete census of substellar objects in nearby SFRs. It has already surveyed five different SFRs (NGC1333, ρ Ophiuchius, Chamaeleon-I, Upper Sco and Lupus-3) cataloguing more than 100 BDs. Their method consists of a photometric selection of sources presenting colours characteristic of young, low-mass objects, complemented by kinematics (when available), which is followed up by spectroscopy observations of the selected sources.

The CrA cloud complex is one of the closest SFRs to the Solar system at only a distance of $\sim$ 150 parsecs, and is reported to have on-going star-formation activity. It was observed in May of 2017 using the Suprime-Cam instrument at the Subaru telescope in Mauna'kea, Hawaii. These observations were made using an I broad-band filter and an H_α narrow-band filter. During this thesis, the dataset produced during the I-band observations was reduced, calibrated and cross-matched with existing publicly available catalogs in order to obtain photometry and colours for these objects. This produced a list of 21 133 sources. Here, we also prepare a list of spectroscopy candidates in the CrA cloud, which was achieved by narrowing down the sources detected near the cloud to those most probable of being young, low-mass members of CrA. This was done by performing a photometric study of the region, using the colours measured from these objects to determine youth, which resulted in a preliminary selection based on their CMD position. Further selection was done by utilizing the PMs and parallax measurements provided by the *Gaia* mission. The *Gaia* mission also provides the kinematic information of already spectroscopically confirmed members of the CrA SFR. These members are used to constrain the parameter space for the kinematic properties of the CrA cloud, and CMD-selected sources with measurements in agreement with those of the known members were selected. From our catalog of 21 133 sources, 15 objects passed both CMD- and *Gaia*-selection. Not all CMD-selected sources had a *Gaia* counterpart due to their faintness. Because of this, a second selection was made for sources

in our CMD-selected sample below the *Gaia* limit (I $\sim$ 19 mag) and above I = 22 mag. This selection resulted in a list of 313 sources, where 145 of them present photometry characteristic of objects with masses below 5 M_J, and with most of them residing in the planetary-mass regime (according to the AMES-COND model) if confirmed as members of CrA. A final list of candidates for follow-up spectroscopy was produced consisting of 328 sources. CrA was also observed using an H_α filter, but this catalog could not be calibrated since there are no publicly available catalogs of CrA with H_α measurements. Still, an arbitrary ZP was applied which allowed us to check for bright emitters. In our list of candidates, only 3 sources present bright H_α emission. An extinction map of the field observed by the Suprime-Cam was built by estimating the extinction of our sources using empirical models. Using this extinction map, we were able to estimate the contamination rate of our list of candidates. These contaminants may be embedded giants, reddened background sources or other such objects which can be mistakenly indexed as low-mass young sources. We calculated a contamination rate of $\sim$ 90%, meaning we expect to confirm $\sim$ 30 new low-mass BDs. The current budget of free-floating planetary mass objects is comprised of $\sim$ 100 objects, including those belonging to nearby moving groups. Our sample therefore promises a significant increase of $\sim$ 30% in the number of known BDs with planetary masses.

The preparatory work for follow-up spectroscopy observations was also developed during this thesis. The KMOS instrument provides integral field unit spectroscopy of multiple objects simultaneously, with great SNR values at IR wavelengths (namely at the H- and K-bands) and was, thus, chosen to perform the spectroscopy observations of the candidate sources produced by this work. These observations will be made using the H + K grating (since in this regime there are spectral features which help astronomers identify BDs). Observations were, then, prepared for the KMOS instrument at the VLT using the KARMA software - a program designed to simulate observations using the KMOS instrument so as to tailor the observations as best as possible, both for the interest of the scientific team as well as that of the operating crew at the VLT. 7 fields were proposed prioritizing the largest number of targets possible for each exposure. Observation times, including the time required to move the telescope and/or instrument around for each observation, were estimated using the *p2 tool* provided by the ESO website, with each observation clocking at around fifty-five minutes resulting in a total observing time of six hours and twenty-five minutes. This work will aid in the characterization of the IMF of the CrA SFR, and should provide insights into the formation processes and early evolution of substellar sources in star-forming clouds.

References

Adams, F. C. and Myers, P. C. (2001). Modes of Multiple Star Formation. , 553(2):744–753.

Allard, F., Hauschildt, P. H., Alexander, D. R., Tamanai, A., and Schweitzer, A. (2001). The Limiting Effects of Dust in Brown Dwarf Model Atmospheres. , 556(1):357–372.

Allard, F., Homeier, D., and Freytag, B. (2011). Model Atmospheres From Very Low Mass Stars to Brown Dwarfs. In Johns-Krull, C., Browning, M. K., and West, A. A., editors, *16th Cambridge Workshop on Cool Stars, Stellar Systems, and the Sun*, volume 448 of *Astronomical Society of the Pacific Conference Series*, page 91.

Almendros-Abad, V., Mužić, K., Moitinho, A., Krone-Martins, A., and Kubiak, K. (2021). Youth analysis of near infrared spectra of young low-mass stars and brown dwarfs. *arXiv e-prints*, page arXiv:2110.06368.

Alves de Oliveira, C., Moraux, E., Bouvier, J., and Bouy, H. (2012). Spectroscopy of new brown dwarf members of ρ Ophiuchi and an updated initial mass function. , 539:A151.

Alves de Oliveira, C., Moraux, E., Bouvier, J., Duchêne, G., Bouy, H., Maschberger, T., and Hudelot, P. (2013). Spectroscopy of brown dwarf candidates in IC 348 and the determination of its substellar IMF down to planetary masses. , 549:A123.

Asplund, M., Grevesse, N., Sauval, A. J., and Scott, P. (2009). The Chemical Composition of the Sun. , 47(1):481–522.

Baraffe, I., Chabrier, G., Barman, T. S., Allard, F., and Hauschildt, P. H. (2003). Evolutionary models for cool brown dwarfs and extrasolar giant planets. The case of HD 209458. , 402:701–712.

Barber, R. J., Tennyson, J., Harris, G. J., and Tolchenov, R. N. (2006). A high-accuracy computed water line list. , 368(3):1087–1094.

Bastian, N., Covey, K. R., and Meyer, M. R. (2010). A Universal Stellar Initial Mass Function? A Critical Look at Variations. , 48:339–389.

Bate, M. R. (2012). Stellar, brown dwarf and multiple star properties from a radiation hydrodynamical simulation of star cluster formation. , 419(4):3115–3146.

Bayo, A., Barrado, D., Stauffer, J., Morales-Calderón, M., Melo, C., Huélamo, N., Bouy, H., Stelzer, B., Tamura, M., and Jayawardhana, R. (2011). Spectroscopy of very low mass stars and brown dwarfs in the Lambda Orionis star forming region. I. Enlarging the census down to the planetary mass domain in Collinder 69. , 536:A63.

Beroiz, M., Cabral, J., and Sanchez, B. (2020). Astroalign: A python module for astronomical image registration. *Astronomy and Computing*, 32:100384.

Bertin, E. (2011). Automated Morphometry with SExtractor and PSFEx. In Evans, I. N., Accomazzi, A., Mink, D. J., and Rots, A. H., editors, *Astronomical Data Analysis Software and Systems XX*, volume 442 of *Astronomical Society of the Pacific Conference Series*, page 435.

Bertin, E. and Arnouts, S. (1996). SExtractor: Software for source extraction. , 117:393–404.

Bibo, E. A., The, P. S., and Dawanas, D. N. (1992). The evolutionary stage of the Herbig Ae/Be stars in the R Coronae Australis star-forming region. , 260:293–302.

Blitz, L. and Shu, F. H. (1980). The origin and lifetime of giant molecular cloud complexes. , 238:148–157.

Bodenheimer, P. (1965). Studies in Stellar Evolution. II. Lithium Depletion during the Pre-Main Contraction. , 142:451.

Bonnarel, F., Fernique, P., Bienaymé, O., Egret, D., Genova, F., Louys, M., Ochsenbein, F., Wenger, M., and Bartlett, J. (2000). The aladin interactive sky atlas. a reference tool for identification of astronomical sources. *Astronomy Astrophysics Supplement Series - ASTRON ASTROPHYS SUPPL SERIES*, 143:33–40.

Bonnell, I. A., Clark, P., and Bate, M. R. (2008). Gravitational fragmentation and the formation of brown dwarfs in stellar clusters. *Monthly Notices of the Royal Astronomical Society*, 389(4):1556–1562.

Bouy, H., Bertin, E., Moraux, E., Cuillandre, J. C., Bouvier, J., Barrado, D., Solano, E., and Bayo, A. (2013). Dynamical analysis of nearby clusters. Automated astrometry from the ground: precision proper motions over a wide field. , 554:A101.

Brown, A. (1987). Radio Emission from Pre–Main-Sequence Stars in Corona Australis. , 322:L31.

Brown, R. L. and Zuckerman, B. (1975). Compact H II regions in the Ophiuchus and R Coronae Austrinae dark clouds. , 202:L125–L128.

Burrows, A., Hubbard, W. B., Lunine, J. I., and Liebert, J. (2001). The theory of brown dwarfs and extrasolar giant planets. *Reviews of Modern Physics*, 73(3):719–765.

Burrows, A., Marley, M., Hubbard, W. B., Lunine, J. I., Guillot, T., Saumon, D., Freedman, R., Sudarsky, D., and Sharp, C. (1997). A Nongray Theory of Extrasolar Giant Planets and Brown Dwarfs. , 491(2):856–875.

Cappa de Nicolau, C. E. and Poppel, W. G. L. (1991). OH- and HI-observations of the CrA dark cloud complex. , 88:615.

Cardelli, J. A., Clayton, G. C., and Mathis, J. S. (1989). The Relationship between Infrared, Optical, and Ultraviolet Extinction. , 345:245.

Casey, B. W., Mathieu, R. D., Suntzeff, N. B., and Walter, F. M. (1995). The Pre-Main-Sequence Triple TY CrA: Spectroscopic Detection of the Secondary and Tertiary Components. , 109:2156.

Chabrier, G. (2003). Galactic Stellar and Substellar Initial Mass Function. , 115(809):763–795.

Chabrier, G., Johansen, A., Janson, M., and Rafikov, R. (2014). Giant Planet and Brown Dwarf Formation. In Beuther, H., Klessen, R. S., Dullemond, C. P., and Henning, T., editors, *Protostars and Planets VI*, page 619.

Chauvin, G., Lagrange, A. M., Beust, H., Fusco, T., Mouillet, D., Lacombe, F., and Pujet, P. e. a. (2003). VLT/NACO adaptive optics imaging of the TY CrA system. A fourth stellar component candidate detected. , 406:L51–L54.

Chen, H., Grenfell, T. G., Myers, P. C., and Hughes, J. D. (1997). Comparison of Star Formation in Five Nearby Molecular Clouds. , 478(1):295–312.

Clarke, C. J., Bonnell, I. A., and Hillenbrand, L. A. (2000). The Formation of Stellar Clusters. In Mannings, V., Boss, A. P., and Russell, S. S., editors, *Protostars and Planets IV*, page 151.

Cushing, M. C., Rayner, J. T., and Vacca, W. D. (2005). An Infrared Spectroscopic Sequence of M, L, and T Dwarfs. , 623(2):1115–1140.

Cutri, R. M., Skrutskie, M. F., van Dyk, S., Beichman, C. A., Carpenter, J. M., Chester, T., and Cambresy, e. a. (2003). VizieR Online Data Catalog: 2MASS All-Sky Catalog of Point Sources (Cutri+ 2003). *VizieR Online Data Catalog*, page II/246.

De Marchi, G., Paresce, F., and Portegies Zwart, S. (2010). On the Temporal Evolution of the Stellar Mass Function in Galactic Clusters. , 718(1):105–111.

Depoy, D. L., Lada, E. A., Gatley, I., and Probst, R. (1990). The Luminosity Function in NGC 2023. , 356:L55.

Elmegreen, B. G. (1989). Gravitational Instabilities in Shearing, Magnetic Galaxies with a Cloudy Interstellar Gas. , 342:L67.

Enoki, M., Nakata, F., Yoshino, A., Yamada, Y., Yagi, M., Takata, T., Ichikawa, S., Ozawa, T., and Horaguchi, T. (2007). New Features of the Subaru Telescope Science Archive System, SMOKA. In Shaw, R. A., Hill, F., and Bell, D. J., editors, *Astronomical Data Analysis Software and Systems XVI*, volume 376 of *Astronomical Society of the Pacific Conference Series*, page 213.

Epchtein, N., Deul, E., Derriere, S., Borsenberger, J., Egret, D., Simon, G., and Alard, C. e. a. (1999). VizieR Online Data Catalog: The DENIS database (Epchtein+, 1999). *VizieR Online Data Catalog*, page B/denis.

Fiorellino, E., Manara, C. F., Nisini, B., Ramsay, S., Antoniucci, S., Giannini, T., Biazzo, K., Alcalà, J., and Fedele, D. (2021). KMOS study of the mass accretion rate from Class I to Class II in NGC 1333⋆. , 650:A43.

Forbrich, J. and Preibisch, T. (2007). Coronae in the Coronet: a very deep X-ray look into a stellar nursery. , 475(3):959–972.

Forbrich, J., Preibisch, T., Menten, K. M., Neuhäuser, R., Walter, F. M., Tamura, M., Matsunaga, N., Kusakabe, N., Nakajima, Y., Brandeker, A., Fornasier, S., Posselt, B., Tachihara, K., and Broeg, C. (2007). Simultaneous X-ray, radio, near-infrared, and optical monitoring of young stellar objects in the Coronet cluster. , 464(3):1003–1013.

Gaia Collaboration, Brown, A. G. A., Vallenari, A., Prusti, T., de Bruijne, J. H. J., Babusiaux, C., and Biermann, M. e. a. (2021). Gaia Early Data Release 3. Summary of the contents and survey properties. , 649:A1.

Gaia Collaboration, Brown, A. G. A., Vallenari, A., Prusti, T., de Bruijne, J. H. J., and Babusiaux, C. e. a. (2018). Gaia Data Release 2. Summary of the contents and survey properties. , 616:A1.

Galli, P. A. B., Bouy, H., Olivares, J., Miret-Roig, N., Sarro, L. M., Barrado, D., Berihuete, A., and Brandner, W. (2020). Corona-Australis DANCe. I. Revisiting the census of stars with Gaia-DR2 data. *arXiv e-prints*, page arXiv:2001.05190.

Garmire, G. P. and Garmire, A. B. (2003). X-ray emission from objects in the CrA dark cloud core. *Astronomische Nachrichten*, 324(1-2):153.

Gaustad, J. E. (1963). The Opacity of Diffuse Cosmic Matter and the Early Stages of Star Formation. , 138:1050.

Geers, V., Scholz, A., Jayawardhana, R., Lee, E., Lafrenière, D., and Tamura, M. (2011). Substellar Objects in Nearby Young Clusters (SONYC). II. The Brown Dwarf Population of ρ Ophiuchi. , 726(1):23.

Glass, I. S. and Penston, M. V. (1975). Infrared photometry in the R CrA association. , 172:227–233.

Goodwin, S. P., Whitworth, A. P., and Ward-Thompson, D. (2004). Simulating star formation in molecular cores. II. The effects of different levels of turbulence. , 423:169–182.

Gould, B. A. (1879). Uranometria Argentina: Brightness and position of every fixed star, down to the seventh magnitude, within one hundred degrees of the South Pole; with atlas. *Resultados del Observatorio Nacional Argentino*, 1:I–387.

Gould, R. J. (1964). The Contraction of Molecular Hydrogen Protostars. , 140:638.

Graham, J. A. (1993). Emission-Line Objects near R CrA. , 105:561.

Haas, M., Heymann, F., Domke, I., Drass, H., Chini, R., and Hoffmeister, V. (2008). A near-infrared survey of the entire R Coronae Australis cloud. , 488(3):987–996.

Haisch, Karl E., J., Lada, E. A., and Lada, C. J. (2001). Disk Frequencies and Lifetimes in Young Clusters. , 553(2):L153–L156.

Harju, J., Haikala, L. K., Mattila, K., Mauersberger, R., Booth, R. S., and Nordh, H. L. (1993). Large scale structure of the R Coronae Australis cloud core. , 278:569–583.

Hennebelle, P. and Chabrier, G. (2009a). Analytical Theory for the Initial Mass Function. II. Properties of the Flow. , 702(2):1428–1442.

Hennebelle, P. and Chabrier, G. (2009b). Analytical Theory for the Initial Mass Function. II. Properties of the Flow. , 702(2):1428–1442.

Henning, T., Launhardt, R., Steinacker, J., and Thamm, E. (1994). Cold dust around southern Herbig Ae/Be stars. , 291:546–556.

Herbig, G. H. and Kameswara Rao, N. (1972). Second Catalog of Emission-Line Stars of the Orion Population. , 174:401.

Herschel, John Frederick William, S. (1847). *Results of astronomical observations made during the years 1834, 5, 6, 7, 8, at the Cape of Good Hope; being the completion of a telescopic survey of the whole surface of the visible heavens, commenced in 1825.*

Hillenbrand, L. A., Strom, S. E., Calvet, N., Merrill, K. M., Gatley, I., Makidon, R. B., Meyer, M. R., and Skrutskie, M. F. (1998). Circumstellar Disks in the Orion Nebula Cluster. , 116(4):1816–1841.

Hollenbach, D. J. and Tielens, A. G. G. M. (1999). Photodissociation regions in the interstellar medium of galaxies. *Reviews of Modern Physics*, 71(1):173–230.

Hubble, E. P. (1922). A general study of diffuse galactic nebulae. , 56:162–199.

Iben, Icko, J. (1965). Stellar Evolution. I. The Approach to the Main Sequence. , 141:993.

James, D. J., Melo, C., Santos, N. C., and Bouvier, J. (2006). Fundamental properties of pre-main sequence stars in young, southern star forming regions: metallicities. , 446(3):971–983.

Jayawardhana, R., Mohanty, S., and Basri, G. (2002). Probing Disk Accretion in Young Brown Dwarfs. , 578(2):L141–L144.

Jayawardhana, R., Mohanty, S., and Basri, G. (2003). Evidence for a T Tauri Phase in Young Brown Dwarfs. , 592(1):282–287.

Jiang, Z., Yao, Y., Yang, J., Baba, D., Kato, D., Kurita, M., Nagashima, C., and Nagata, T. e. a. (2003). A Near-Infrared Study of the Star-forming Region S269. , 596(2):1064–1079.

Joy, A. H. (1945). T Tauri Variable Stars. , 102:168.

Knacke, R. F., Strom, K. M., Strom, S. E., Young, E., and Kunkel, W. (1973). A young stellar group in the vicinity of R Coronae Austrinae. , 179:847–854.

Koyama, K., Hamaguchi, K., Ueno, S., Kobayashi, N., and Feigelson, E. D. (1996). Discovery of Hard X-Rays from a Cluster of Protostars. , 48:L87–L92.

Kroupa, P. (2001). On the variation of the initial mass function. , 322(2):231–246.

Kumar, S. S. (1963). The Structure of Stars of Very Low Mass. , 137:1121.

Lada, C. J. and Lada, E. A. (1991). The nature, origin and evolution of embedded star clusters. In Janes, K., editor, *The Formation and Evolution of Star Clusters*, volume 13 of *Astronomical Society of the Pacific Conference Series*, pages 3–22.

Lada, C. J. and Lada, E. A. (2003). Embedded Clusters in Molecular Clouds. , 41:57–115.

Lang, D., Hogg, D. W., Mierle, K., Blanton, M., and Roweis, S. (2010). Astrometry.net: Blind Astrometric Calibration of Arbitrary Astronomical Images. , 139(5):1782–1800.

López Martí, B., Eislöffel, J., and Mundt, R. (2005). The very low-mass population of the Corona Australis and Chamaeleon II star forming regions. , 444(1):175–186.

Loren, R. B. (1979). The star formation process in molecular clouds associated with Herbig Be/Ae stars. II. The nonhomologous collapse of the CrA cloud. , 227:832–852.

Lucas, P. W., Roche, P. F., Allard, F., and Hauschildt, P. H. (2001). Infrared spectroscopy of substellar objects in Orion. , 326(2):695–721.

Luhman, K. L. (2012). The Formation and Early Evolution of Low-Mass Stars and Brown Dwarfs. , 50:65–106.

Luhman, K. L., D'Alessio, P., Calvet, N., Allen, L. E., Hartmann, L., Megeath, S. T., Myers, P. C., and Fazio, G. G. (2005). Spitzer Identification of the Least Massive Known Brown Dwarf with a Circumstellar Disk. , 620(1):L51–L54.

Marraco, H. G. and Rydgren, A. E. (1981). On the distance and membership of the R CrA T association. , 86:62–68.

Masunaga, H. and Inutsuka, S.-i. (2000). A Radiation Hydrodynamic Model for Protostellar Collapse. II. The Second Collapse and the Birth of a Protostar. , 531(1):350–365.

McMahon, R. G., Banerji, M., Gonzalez, E., Koposov, S. E., Bejar, V. J., Lodieu, N., Rebolo, R., and VHS Collaboration (2013). First Scientific Results from the VISTA Hemisphere Survey (VHS). *The Messenger*, 154:35–37.

Mendoza, E. E., Jaschek, M., and Jaschek, C. (1969). The Spectrum of R Coronae Australis. *Boletin de los Observatorios Tonantzintla y Tacubaya*, 5:107–109.

Meyer, M. R. and Wilking, B. A. (2009). Infrared Spectra of Young Stars Embedded in the R Coronae Australis Cloud. , 121(878):350.

Miyazaki, S., Komiyama, Y., Sekiguchi, M., Okamura, S., Doi, M., Furusawa, H., and Hamabe, M. e. a. (2002). Subaru Prime Focus Camera – Suprime-Cam. , 54:833–853.

Monet, D. G., Levine, S. E., Canzian, B., Ables, H. D., and Bird, A. R. e. a. (2003). The USNO-B Catalog. , 125(2):984–993.

Mužić, K., Scholz, A., Geers, V., Fissel, L., and Jayawardhana, R. (2011). Substellar Objects in Nearby Young Clusters (SONYC). III. Chamaeleon-I. , 732(2):86.

Mužić, K., Scholz, A., Geers, V., Jayawardhana, R., and Tamura, M. (2012). Substellar Objects in Nearby Young Clusters (SONYC). V. New Brown Dwarfs in ρ Ophiuchi. , 744(2):134.

Mužić, K., Scholz, A., Geers, V. C., and Jayawardhana, R. (2015). Substellar Objects in Nearby Young Clusters (SONYC) IX: The Planetary-Mass Domain of Chamaeleon-I and Updated Mass Function in Lupus-3. , 810(2):159.

Mužić, K., Scholz, A., Geers, V. C., Jayawardhana, R., and López Martí, B. (2014). Substellar Objects in Nearby Young Clusters (SONYC). VIII. Substellar Population in Lupus 3. , 785(2):159.

Mužić, K., Scholz, A., Peña Ramírez, K., Jayawardhana, R., Schödel, R., Geers, V. C., Cieza, L. A., and Bayo, A. (2019). Looking Deep into the Rosette Nebula's Heart: The (Sub)stellar Content of the Massive Young Cluster NGC 2244. , 881(1):79.

Muzerolle, J., Briceño, C., Calvet, N., Hartmann, L., Hillenbrand, L., and Gullbring, E. (2000a). Detection of Disk Accretion at the Substellar Limit. , 545(2):L141–L144.

Muzerolle, J., Calvet, N., Briceño, C., Hartmann, L., and Hillenbrand, L. (2000b). Disk Accretion in the 10 MYR Old T Tauri Stars TW Hydrae and Hen 3-600A. , 535(1):L47–L50.

Muzerolle, J., Hillenbrand, L., Calvet, N., Briceño, C., and Hartmann, L. (2003). Accretion in Young Stellar/Substellar Objects. , 592(1):266–281.

Neuhaeuser, R. and Preibisch, T. (1997). ROSAT detection of Class I protostars in the CrA Coronet. , 322:L37–L40.

Neuhäuser, R. and Forbrich, J. (2008). *The Corona Australis Star Forming Region*, volume 5, page 735.

Neuhäuser, R., Walter, F. M., Covino, E., Alcalá, J. M., Wolk, S. J., Frink, S., Guillout, P., Sterzik, M. F., and Comerón, F. (2000). Search for young stars among ROSAT All-Sky Survey X-ray sources in and around the R CrA dark cloud. , 146:323–347.

Nisini, B., Antoniucci, S., Giannini, T., and Lorenzetti, D. (2005). Probing the embedded YSOs of the R CrA region through VLT-ISAAC spectroscopy. , 429:543–557.

Nürnberger, D. E. A., Bronfman, L., Yorke, H. W., and Zinnecker, H. (2002). The molecular environment of NGC 3603. I. Spatial distribution and kinematic structure. , 394:253–269.

Oort, J. H. and Spitzer, Lyman, J. (1955). Acceleration of Interstellar Clouds by O-Type Stars. , 121:6.

Padoan, P. and Nordlund, Å. (2002). The Stellar Initial Mass Function from Turbulent Fragmentation. , 576(2):870–879.

Padoan, P. and Nordlund, Å. (2004). The "Mysterious" Origin of Brown Dwarfs. , 617(1):559–564.

Palla, F. and Stahler, S. W. (1990). The Birthline for Intermediate-Mass Stars. , 360:L47.

Palla, F., Zinnecker, H., Maeder, A., and Meynet, G. (2002). *Physics of Star Formation in Galaxies*, volume 29, pages 9–128.

Patten, B. M. (1998). The Low-Mass Membership of the R CrA T Association. In Donahue, R. A. and Bookbinder, J. A., editors, *Cool Stars, Stellar Systems, and the Sun*, volume 154 of *Astronomical Society of the Pacific Conference Series*, page 1755.

Peña Ramírez, K., Béjar, V. J. S., Zapatero Osorio, M. R., Petr-Gotzens, M. G., and Martín, E. L. (2012). New Isolated Planetary-mass Objects and the Stellar and Substellar Mass Function of the σ Orionis Cluster. , 754(1):30.

Pearson, S., Scholz, A., Teixeira, P. S., Mužić, K., and Almendros-Abad, V. (2021). The first spectroscopically confirmed brown dwarfs in NGC 2264. , 507(3):4074–4085.

Pearson, S., Scholz, A., Teixeira, P. S., Mužić, K., and Eislöffel, J. (2020). The brown dwarf population in the star-forming region NGC 2264. , 499(2):2292–2302.

Pecaut, M. J. and Mamajek, E. E. (2013). Intrinsic Colors, Temperatures, and Bolometric Corrections of Pre-main-sequence Stars. , 208(1):9.

Peterson, D. E., Caratti o Garatti, A., Bourke, T. L., Forbrich, J., Gutermuth, R. A., and Jørgensen, J. K. e. a. (2011). The Spitzer Survey of Interstellar Clouds in the Gould Belt. III. A Multi-wavelength View of Corona Australis. , 194(2):43.

Rayner, J. T., Cushing, M. C., and Vacca, W. D. (2009). The Infrared Telescope Facility (IRTF) Spectral Library: Cool Stars. , 185(2):289–432.

Reid, I. N. and Hawley, S. L. (2005). *New light on dark stars : red dwarfs, low-mass stars, brown dwarfs*.

Reipurth, B., Pedrosa, A., and Lago, M. T. V. T. (1996). Hα emission in pre-main sequence stars. I. an atlas of line profiles. , 120:229–256.

Robitaille, T., Deil, C., and Ginsburg, A. (2020). reproject: Python-based astronomical image reprojection.

Rodrigo, C., Solano, E., and Bayo, A. (2012). SVO Filter Profile Service Version 1.0. IVOA Working Draft 15 October 2012.

Salpeter, E. E. (1955). The Luminosity Function and Stellar Evolution. , 121:161.

Schöier, F. L., Jørgensen, J. K., Pontoppidan, K. M., and Lundgren, A. A. (2006). Low-mass star formation in R Coronae Australis: observations of organic molecules with the APEX telescope. , 454(2):L67–L70.

Scholz, A., Geers, V., Clark, P., Jayawardhana, R., and Muzic, K. (2013). Substellar Objects in Nearby Young Clusters. VII. The Substellar Mass Function Revisited. , 775(2):138.

Scholz, A., Muzic, K., Geers, V., Bonavita, M., Jayawardhana, R., and Tamura, M. (2012a). Substellar Objects in Nearby Young Clusters (SONYC). IV. A Census of Very Low Mass Objects in NGC 1333. , 744(1):6.

Scholz, A., Muzic, K., Geers, V., Bonavita, M., Jayawardhana, R., and Tamura, M. (2012b). VizieR Online Data Catalog: SONYC census of very low-mass objects in NGC1333 (Scholz+, 2012). *VizieR Online Data Catalog*, page J/ApJ/744/6.

Scholz, A., Muzic, K., Geers, V., Jayawardhana, R., Tamura, M., Dawson, P., and Ray, T. P. (2011). The Brown Dwarf Population in Nearby Star-Forming Regions. In *Stellar Clusters & Associations: A RIA Workshop on Gaia*, pages 250–254.

Schulz, A., Guesten, R., Zylka, R., and Serabyn, E. (1991). Dense clumps in NGC 2024 - protostellar condensations? , 246:570.

Schulz, N. S. (2005). *From Dust To Stars Studies of the Formation and Early Evolution of Stars*.

Sharples, R., Bender, R., Agudo Berbel, A., Bezawada, N., Castillo, R., Cirasuolo, M., Davidson, G., and Davies, R. e. a. (2013). First Light for the KMOS Multi-Object Integral-Field Spectrometer. *The Messenger*, 151:21–23.

Shu, F. H. (1977). Self-similar collapse of isothermal spheres and star formation. , 214:488–497.

Shu, F. H., Adams, F. C., and Lizano, S. (1987). Star formation in molecular clouds: observation and theory. , 25:23–81.

Sicilia-Aguilar, A., Henning, T., Juhász, A., Bouwman, J., Garmire, G., and Garmire, A. (2008). Very Low Mass Objects in the Coronet Cluster: The Realm of the Transition Disks. , 687(2):1145–1167.

Sicilia-Aguilar, A., Henning, T., Kainulainen, J., and Roccatagliata, V. (2011). Protostars and Stars in the Coronet Cluster: Age, Evolution, and Cluster Structure. , 736(2):137.

Spitzer, L. (1978). *Physical processes in the interstellar medium*.

Stahler, S. W. (1984). The cyanopolyynes as a chemical clock for molecular clouds. , 281:209–218.

Stahler, S. W., Shu, F. H., and Taam, R. E. (1980a). The evolution of protostars. I - Global formulation and results. , 241:637–654.

Stahler, S. W., Shu, F. H., and Taam, R. E. (1980b). The evolution of protostars. II - The hydrostatic core. , 242:226–241.

Stamatellos, D., Hubber, D. A., and Whitworth, A. P. (2007). Brown dwarf formation by gravitational fragmentation of massive, extended protostellar discs. , 382(1):L30–L34.

Taylor, K. N. R. and Storey, J. W. V. (1984). The coronet, an obscured cluster adjacent to R Corona Austrina. , 209:5P–10.

Thies, I. and Kroupa, P. (2007). A Discontinuity in the Low-Mass Initial Mass Function. , 671(1):767–780.

Trumpler, R. J. (1930). Preliminary results on the distances, dimensions and space distribution of open star clusters. *Lick Observatory Bulletin*, 420:154–188.

Tsuji, T. (1964). Molecular abundance in stellar atmospheres. *Annals of the Tokyo Astronomical Observatory*, 9(1):1–110.

Valenti, J. A., Fallon, A. A., and Johns-Krull, C. M. (2003). An IUE Atlas of Pre-Main-Sequence Stars. III. Co-added Final Archive Spectra from the Long-Wavelength Cameras. , 147(2):305–336.

van Dokkum, P. G. (2001). Cosmic-Ray Rejection by Laplacian Edge Detection. , 113(789):1420–1427.

Ventura, P., Zeppieri, A., Mazzitelli, I., and D'Antona, F. (1998). Pre-main sequence Lithium burning: the quest for a new structural parameter. , 331:1011–1021.

Vrba, F. J., Strom, S. E., and Strom, K. M. (1976). Infrared surveys of dark-cloud complexes. III. The R Corona Austrina dark cloud. , 81:317–319.

Walter, F. M. (1986). X-Ray Sources in Regions of Star Formation. I. The Naked T Tauri Stars. , 306:573.

Walter, F. M., Vrba, F. J., Wolk, S. J., Mathieu, R. D., and Neuhauser, R. (1997). X-Ray Sources in Regions of Star Formation. VI. The R CRA Association as Viewed by Einstein. , 114:1544.

Wegner, M. and Muschielok, B. (2008). Karma: the observation preparation tool for kmos. *Proc SPIE*, 7019.

Whelan, E. T., Ray, T. P., Bacciotti, F., Natta, A., Testi, L., and Randich, S. (2005). A resolved outflow of matter from a brown dwarf. , 435(7042):652–654.

White, R. J. and Basri, G. (2003). Very Low Mass Stars and Brown Dwarfs in Taurus-Auriga. , 582(2):1109–1122.

Whitworth, A. P. and Zinnecker, H. (2004). The formation of free-floating brown dwarves and planetary-mass objects by photo-erosion of prestellar cores. , 427:299–306.

Wilking, B. A., Greene, T. P., Lada, C. J., Meyer, M. R., and Young, E. T. (1992). IRAS Observations of Young Stellar Objects in the Corona Australis Dark Cloud. , 397:520.

Wilking, B. A., Harvey, P. M., Joy, M., Hyland, A. R., and Jones, T. J. (1985). Far-infrared observations of young clusters embedded in the R CoronaeAustralis and rho Ophiuchi dark clouds. , 293:165–177.

Wilking, B. A., McCaughrean, M. J., Burton, M. G., Giblin, T., Rayner, J. T., and Zinnecker, H. (1997). Deep Infrared Imaging of the R Coronae Australis Cloud Core. , 114:2029.

Wilking, B. A., Taylor, K. N. R., and Storey, J. W. V. (1986). The nature of the infrared cluster in the R Coronae Australis cloud core. , 92:103–110.

Williams, J. P. and McKee, C. F. (1997). The Galactic Distribution of OB Associations in Molecular Clouds. , 476(1):166–183.

Appendices

Appendix A

Figures

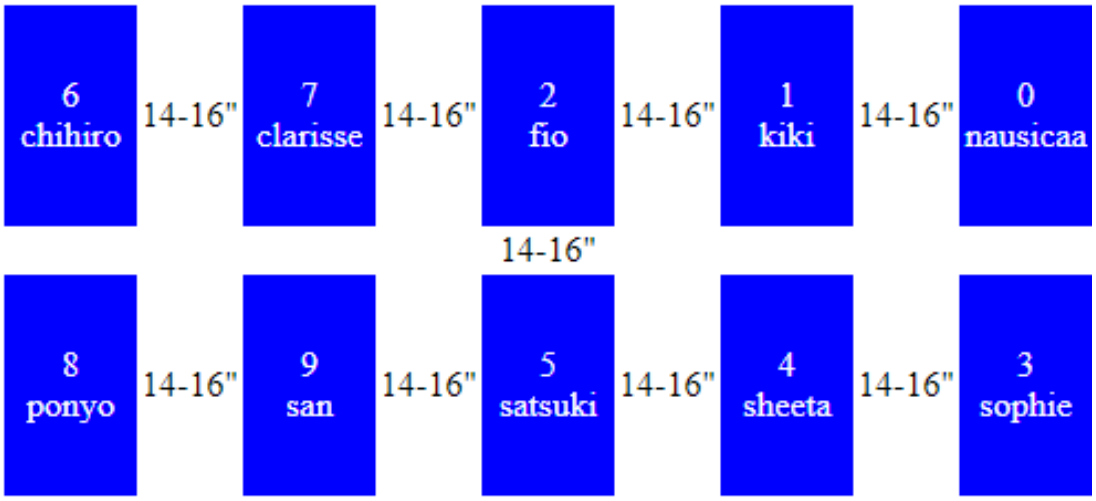

Figure A.1: *The arrangement of the detectors on the Suprime-Cam instrument.*

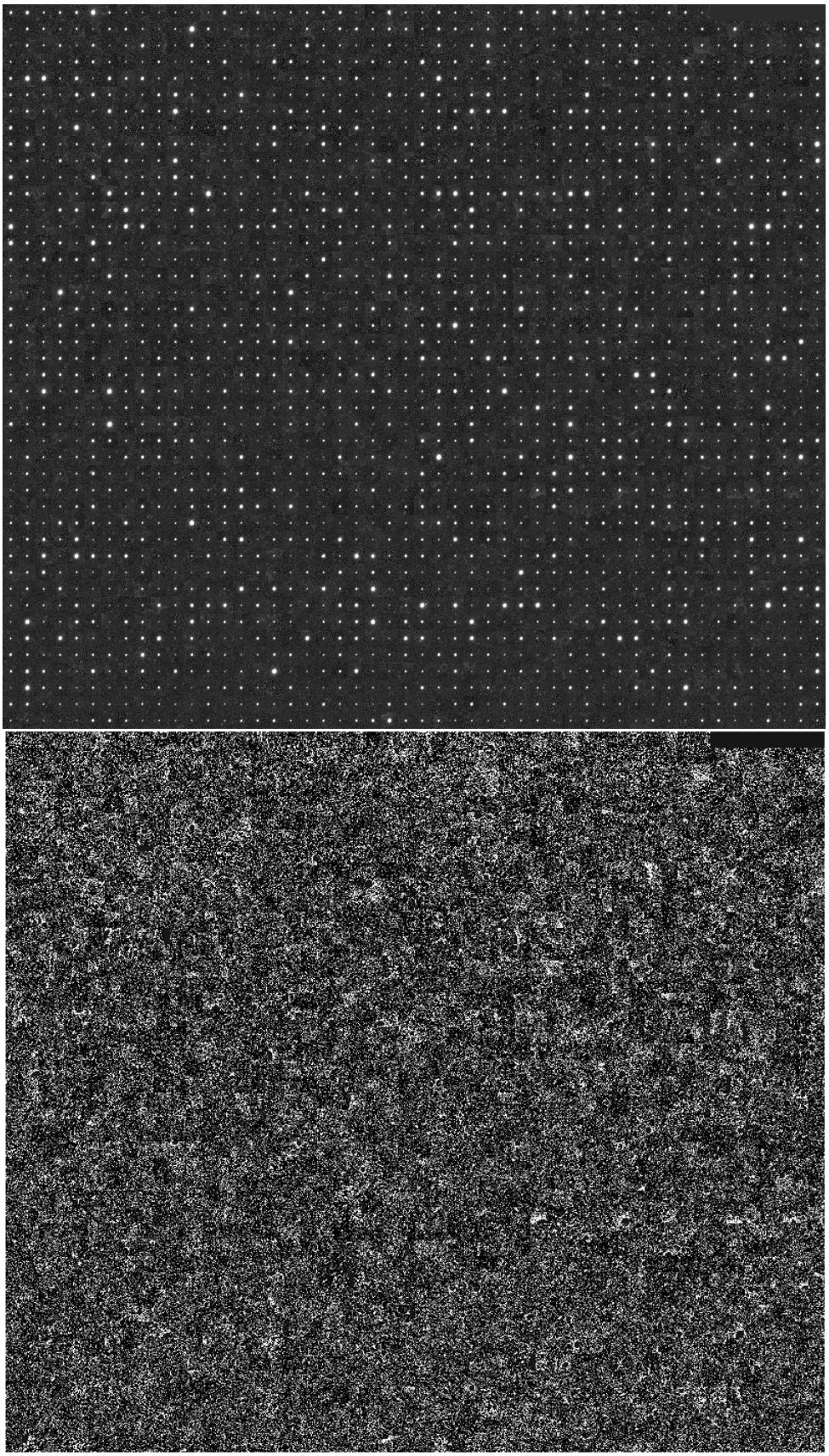

Figure A.2: ***Top Panel****: The sample of vignettes used during the* PSFEx *run on the Clarisse detector.* ***Bottom Panel****: The residuals output of the* PSFEx *run on the Clarisse detector.*

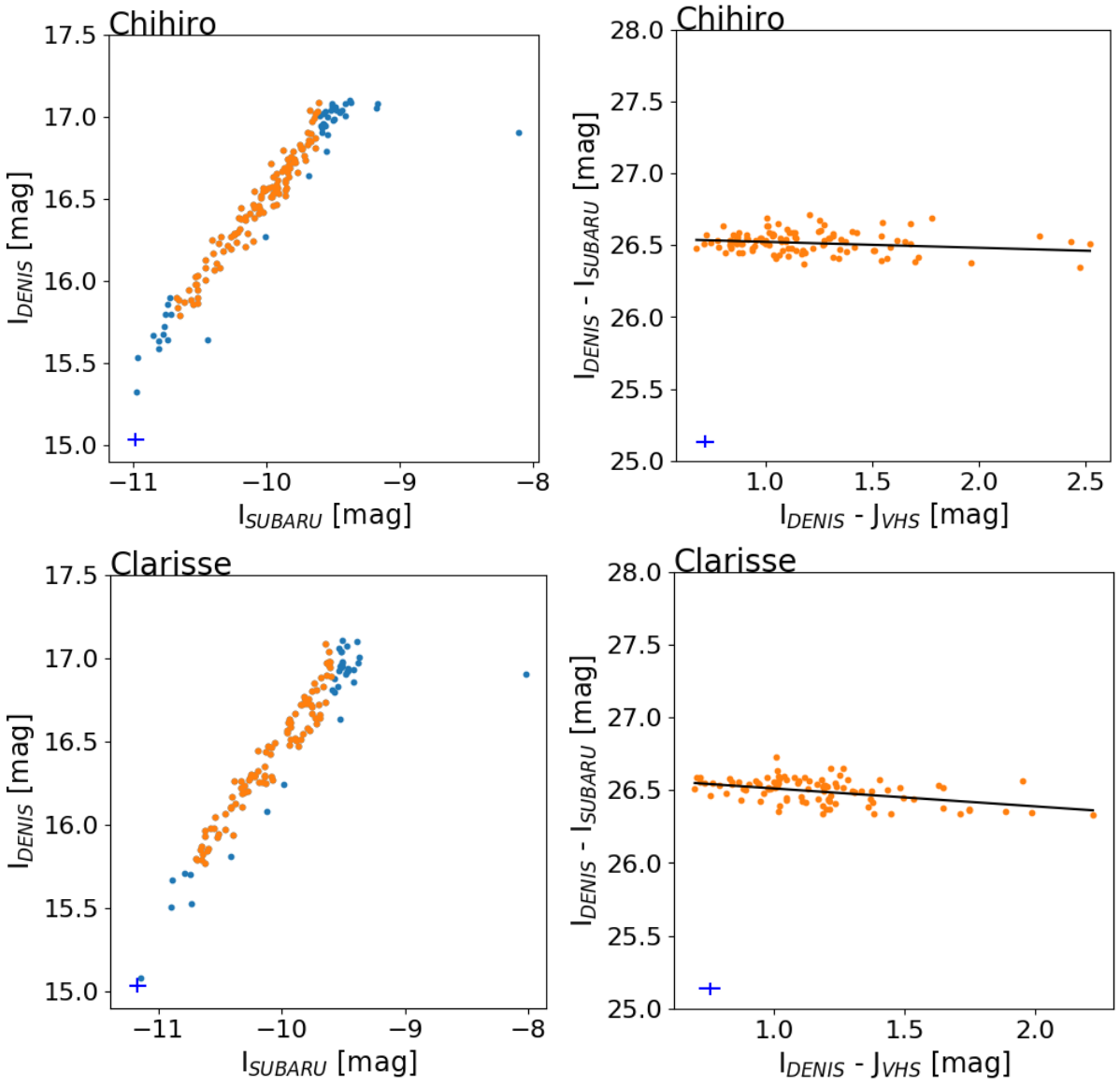

Figure A.3: *Calibration plots for the Chihiro and Clarisse detectors using the DENIS and VHSDR6 catalogs.*

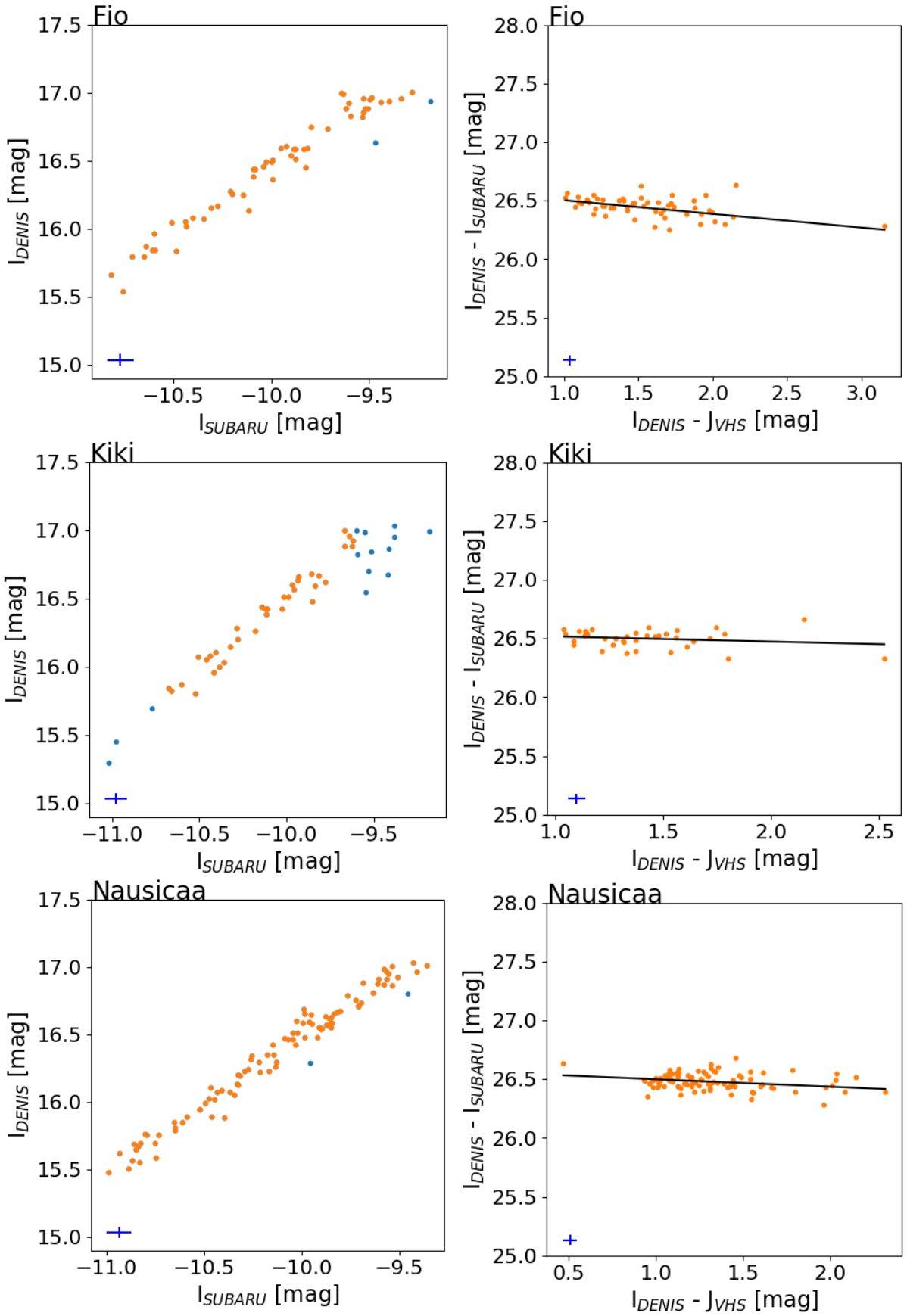

Figure A.4: *Calibration plots for the Fio, Kiki and Nausicaa detectors using the DENIS and VHSDR6 catalogs.*

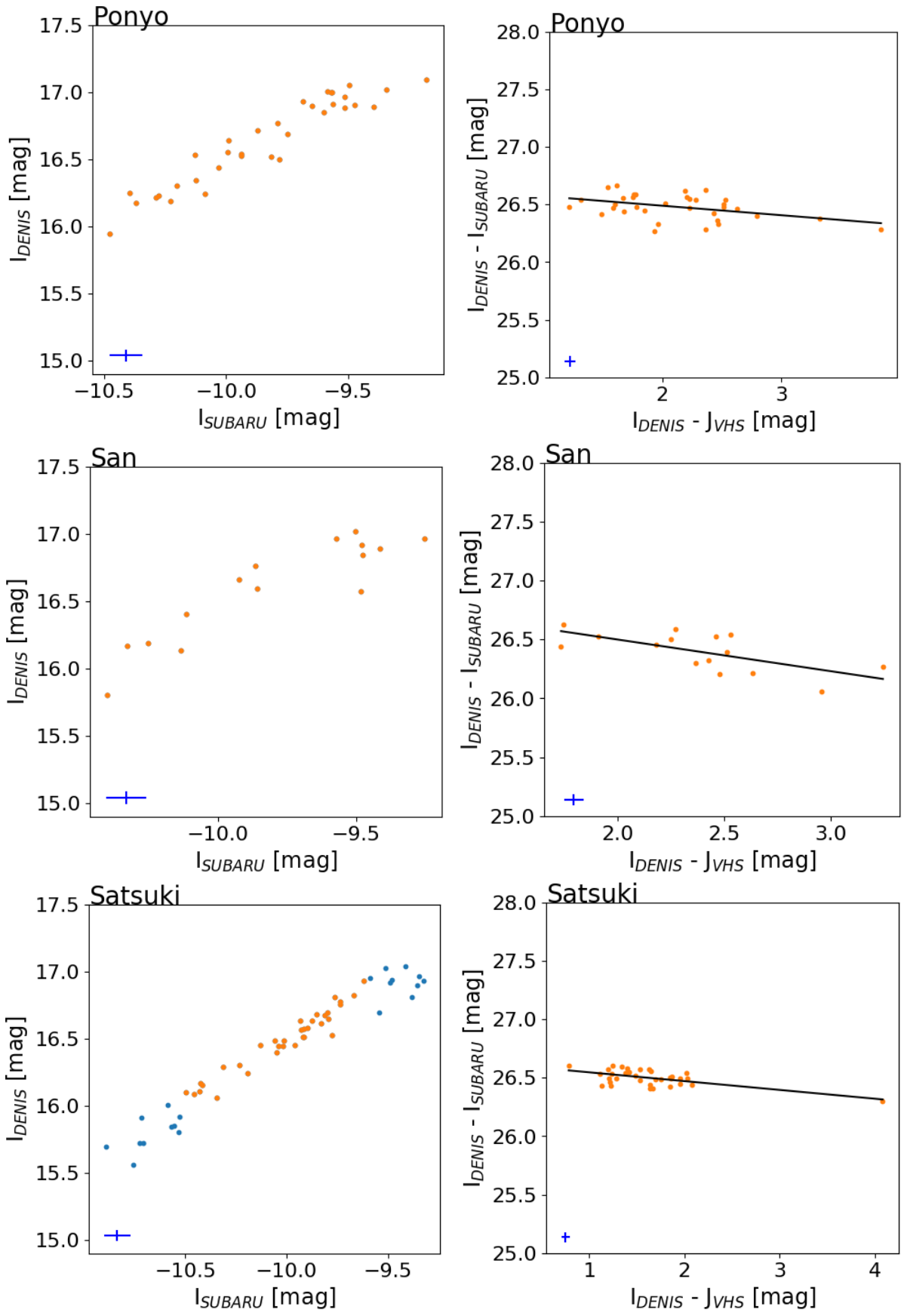

Figure A.5: *Calibration plots for the Ponyo, San and Satsuki detectors using the DENIS and VHSDR6 catalogs.*

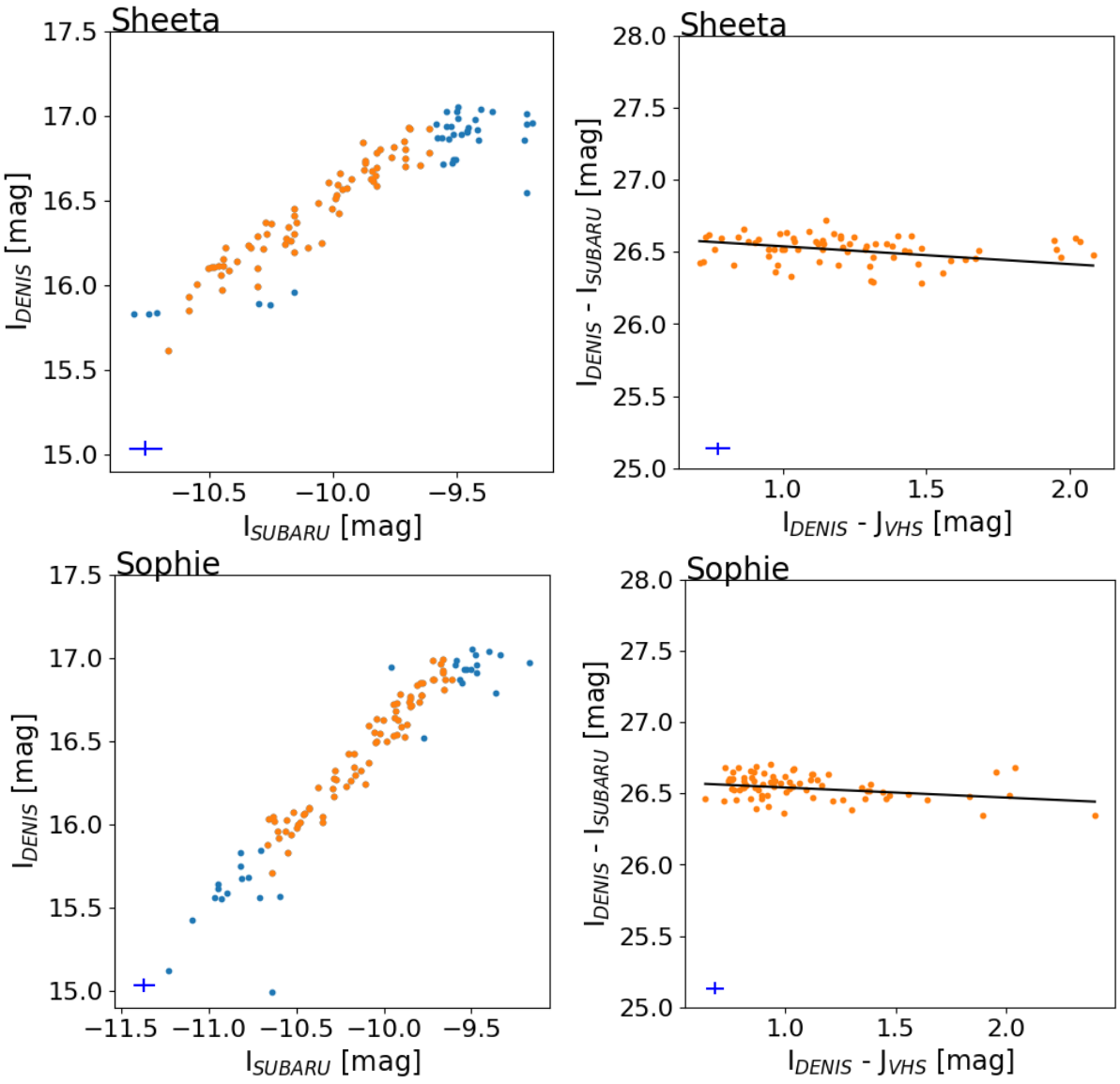

Figure A.6: *Calibration plots for the Sheeta and Sophie detectors using the DENIS and VHSDR6 catalogs.*

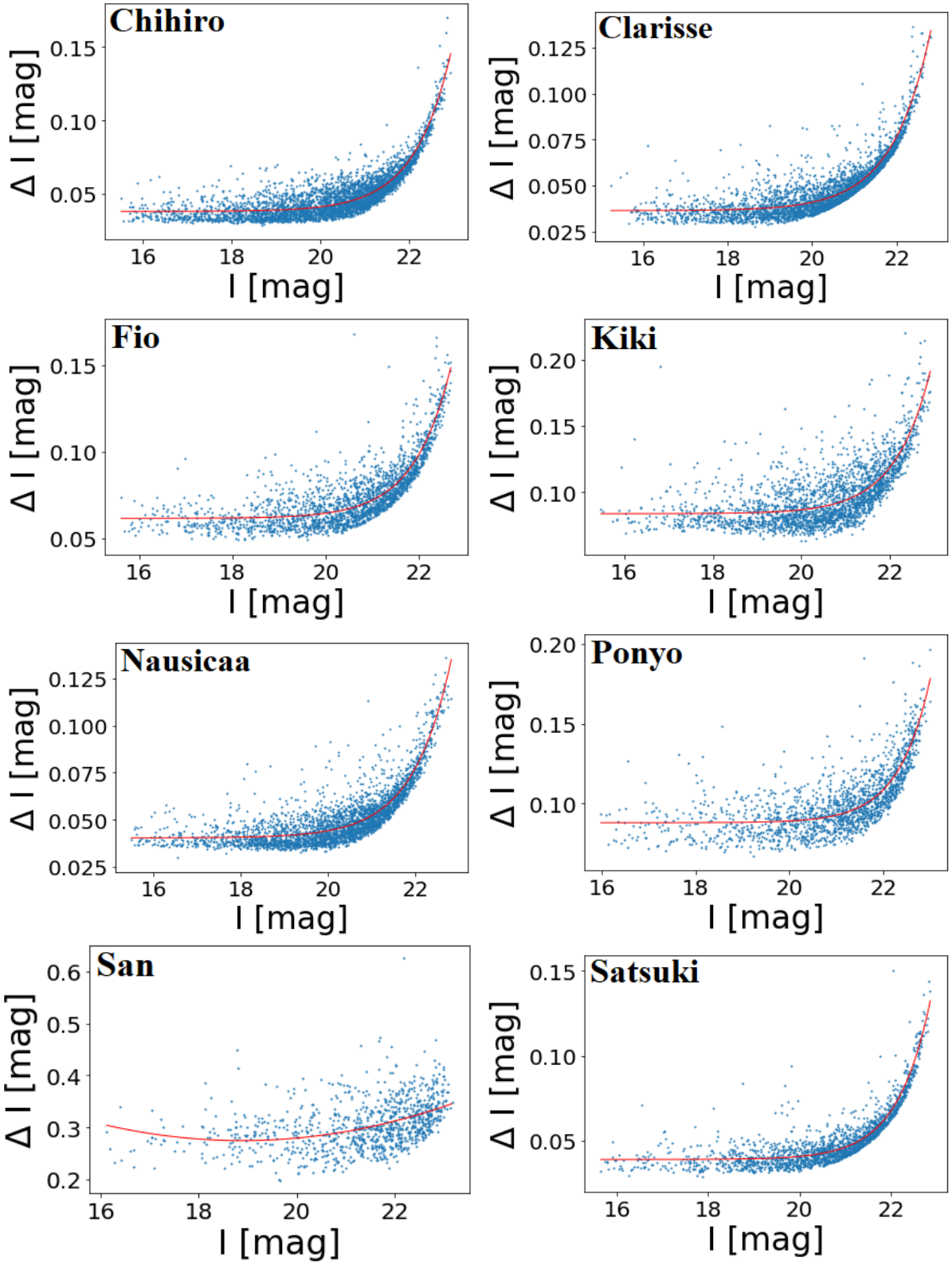

Figure A.7: *The error vs. magnitude plots for the Chihiro, Clarisse, Fio, Kiki, Nausicaa, Ponyo, San and Satsuki detectors.*

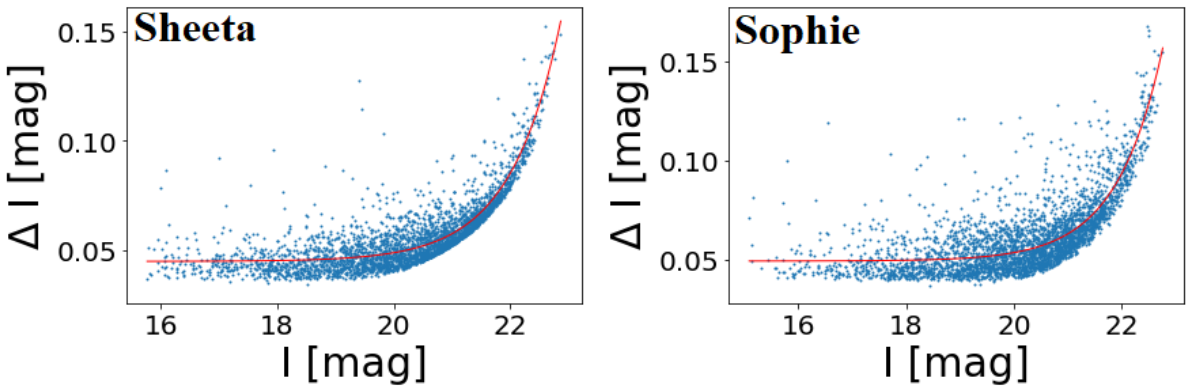

Figure A.8: *The error vs. magnitude plots for the Sheeta and Sophie detectors.*

Appendix B

Tables

Table B.1: *The compilation of spectroscopically confirmed members of CrA along with their on-sky position and* Gaia *kinematic measurements. Some of these sources reside outside the field observed by the Suprime-Cam instrument.*

ID	RA	Dec	μ_α	μ_δ	ϖ	RUWE
1	19:03:06.75	-37:12:50.1	3.28 ± 0.04	-26.01 ± 0.03	6.38 ±0.04	2.42
2	19:02:01.98	-37:07:43.9	4.93 ± 0.02	-25.81 ± 0.01	6.54 ±0.02	1.05
3	18:57:34.22	-37:32:33.7	4.85 ± 0.03	-27.78 ± 0.02	6.40 ±0.03	1.22
4	19:01:25.64	-37:04:54.0	4.31 ± 0.08	-28.37 ± 0.07	6.46 ±0.07	1.00
5	19:01:20.85	-37:03:03.2	4.43 ± 0.10	-27.41 ± 0.08	6.96 ±0.09	1.04
6	18:59:50.95	-37:06:31.9	4.12 ± 0.23	-28.22 ± 0.21	6.36 ±0.24	1.08
7	19:00:44.56	-37:02:11.3	5.48 ± 0.04	-27.25 ± 0.03	6.48 ±0.04	1.22
8	19:00:29.07	-36:56:04.1	3.85 ± 0.13	-28.56 ± 0.10	6.31 ±0.14	5.88
9	18:58:01.83	-36:53:45.7	5.12 ± 0.02	-26.80 ± 0.02	6.56 ±0.02	1.13
10	18:52:17.31	-37:00:12.4	2.94 ± 0.02	-28.32 ± 0.02	6.80 ±0.02	1.58
11	18:57:20.85	-36:43:01.1	4.17 ± 0.02	-28.90 ± 0.02	6.96 ±0.01	0.96
12	18:57:18.00	-36:42:36.5	2.61 ± 0.10	-26.36 ± 0.09	7.29 ±0.10	3.14
13	19:02:00.13	-37:02:22.6	5.40 ± 0.04	-26.45 ± 0.03	6.55 ±0.03	1.22
14	19:01:49.37	-37:00:29.1	5.95 ± 0.06	-28.69 ± 0.05	6.53 ±0.05	1.06
15	19:02:12.03	-37:03:09.9	5.57 ± 0.13	-29.52 ± 0.11	6.41 ±0.12	0.98
16	19:02:27.10	-36:58:13.7	...	...	...	...
17	19:01:58.79	-36:57:50.3	...	...	...	...
18	19:02:22.14	-36:55:41.4	6.13 ± 0.02	-27.50 ± 0.01	6.48 ±0.01	1.25
19	19:01:34.87	-37:00:57.0	5.84 ± 0.02	-28.84 ± 0.01	6.51 ±0.02	1.04
20	19:01:29.04	-37:01:49.0	4.19 ± 0.06	-28.85 ± 0.05	6.50 ±0.06	2.11
21	19:01:41.65	-36:59:53.3	6.03 ± 0.04	-27.34 ± 0.04	6.44 ±0.04	1.28
22	19:01:25.78	-36:59:19.6	...	...	...	...
23	19:01:28.74	-36:59:32.2	4.32 ± 0.06	-28.07 ± 0.05	6.58 ±0.05	2.12
24	19:01:27.18	-36:59:09.0	3.98 ± 0.03	-26.35 ± 0.02	6.59 ±0.02	1.28
25	19:01:18.95	-36:58:28.7	4.40 ± 0.14	-27.16 ± 0.11	6.61 ±0.12	0.99
26	19:01:32.34	-36:58:03.5	...	...	...	...
27	19:01:33.87	-36:57:45.3	...	...	...	...
28	19:01:53.69	-36:57:08.6	7.62 ± 0.54	-20.90 ± 0.50	7.99 ±0.49	3.05

Table B.1 continued from previous page

ID	RA	Dec	μ_α	μ_δ	ϖ	RUWE
29	19:01:39.17	-36:53:30.0	3.70 ± 0.04	-28.56 ± 0.03	6.40 ±0.04	1.18
30	19:01:38.94	-36:53:27.0	3.93 ± 0.03	-28.50 ± 0.03	6.45 ±0.03	1.01
31	19:01:40.83	-36:52:34.3	4.31 ± 0.16	-31.80 ± 0.14	6.29 ±0.17	8.16
32	19:01:40.43	-36:51:42.8	5.79 ± 1.26	-27.99 ± 1.24	5.56 ±0.90	1.13
33	19:02:09.68	-36:46:34.9	4.46 ± 0.06	-27.15 ± 0.05	6.50 ±0.05	0.91
34	19:01:08.60	-36:57:20.2	7.05 ± 0.06	-26.51 ± 0.06	6.23 ±0.07	2.10
35	19:01:09.72	-36:47:53.3	3.28 ± 0.02	-28.35 ± 0.02	6.46 ±0.02	1.24
36	19:00:59.75	-36:47:11.5	3.86 ± 0.21	-28.94 ± 0.17	6.59 ±0.19	0.99
37	19:00:39.31	-36:48:12.7	5.03 ± 0.03	-27.68 ± 0.02	6.49 ±0.03	1.19
38	19:01:40.60	-36:44:32.0	...	...	...	...
39	19:17:23.83	-37:56:51.0	5.71 ± 0.10	-31.76 ± 0.08	7.12 ±0.10	6.68
40	19:01:55.25	-37:23:41.2	6.35 ± 0.16	-24.63 ± 0.14	6.62 ±0.17	6.13
41	18:39:05.29	-37:26:22.3	0.22 ± 0.02	-28.76 ± 0.02	6.82 ±0.02	0.86
42	18:45:34.84	-37:50:20.1	3.89 ± 0.06	-26.32 ± 0.05	6.61 ±0.06	2.81
43	18:44:31.17	-37:23:35.2	3.61 ± 0.11	-27.71 ± 0.08	6.68 ±0.09	6.44
44	18:59:14.97	-37:11:31.2	4.35 ± 0.04	-27.39 ± 0.03	6.59 ±0.03	1.66
45	18:59:14.83	-37:11:32.9	4.58 ± 0.03	-27.79 ± 0.02	6.64 ±0.03	1.30
46	19:00:01.58	-36:37:05.9	3.79 ± 0.03	-27.39 ± 0.02	6.49 ±0.02	1.33
47	18:56:44.01	-35:45:32.7	4.27 ± 0.02	-26.99 ± 0.01	6.62 ±0.01	1.06
48	19:01:28.69	-34:22:36.3	11.44 ± 0.03	-48.07 ± 0.02	12.72 ±0.02	0.98
49	18:44:21.93	-35:41:44.0	1.58 ± 0.08	-35.36 ± 0.06	6.90 ±0.09	4.87
50	18:42:57.98	-35:32:43.3	1.30 ± 0.02	-26.98 ± 0.01	6.62 ±0.02	1.10
51	18:40:52.71	-35:46:41.5	1.31 ± 0.02	-27.37 ± 0.02	6.75 ±0.02	1.19
52	18:41:48.56	-35:25:44.1	1.14 ± 0.02	-27.39 ± 0.01	6.70 ±0.01	0.97
53	18:36:39.56	-34:51:26.1	6.63 ± 0.04	-26.62 ± 0.03	7.10 ±0.03	1.79

Parameter	Value	Description
DETECT_MINAREA	4	Minimum number of pixels an object must feature in to be considered a source
DETECT_THRESH	2.7	The flux deviation from the background mean for an object to be considered a source
PHOT_APERTURES	20	The diameter of the fixed aperture used to calculate the flux of a source
SATUR_LEVEL	30000 / 44000	The minimum number of counts for a pixel to be considered saturated
SEEING_FWHM	0.7	The seeing of the full-width half maximum in arc-seconds

Table B.2: *The configuration parameters used during our* SExtractor *routine. Parameters not shown here were used with their default values. For the SATUR_LEVEL parameter, more than one value is shown (denoted by a forward-slash). We did not want optical effects from extremely bright sources to contaminate the PSF models, so different settings were used for the first (building a catalog to feed into PSFEx) and second (applying the PSF models on our images) run of* SExtractor.

Parameter	Description
NUMBER	The catalog number of the source
X_IMAGE	The x-axis coordinate of the source
Y_IMAGE	The y-axis coordinate of the source
[1]FLUX_APER(1)	The calculated fixed aperture flux of the source
[1]FLUXERR_APER(1)	The root-mean-squared error of the calculated fixed aperture flux of the source
[1]FLUX_RADIUS	The half-light radius of the source
[2]FLUX_MODEL	The PSF-fitted flux of a source
[2]FLUXERR_MODEL	The root-mean-squared error of the PSF-fitted flux of a source
ELONGATION	The calculated elongation of the source. It is determined by dividing the semi-major axis over the semi-minor axis
ELLIPTICITY	The calculated ellipticity of the source. It is determined by subtracting the semi-minor axis over the semi-major axis division from 1
FLAGS	The flags attributed to the source
SNR_WIN	The SNR of the source

Table B.3: *The* SExtractor *parameters calculated during our routine.* [1] *These parameters were taken only during the first* SExtractor *run (building a catalog to feed into PSFEx);* [2] *These parameters were only taken during the second* SExtractor *run (when applying the PSF models to our images).*

Table B.4: *The configuration parameters used during our* PSFEx *routine. Parameters not shown here were used with their default values.*

Parameter	Value	Description
PSF_ACCURACY	0.01	The expected accuracy of PSF pixel values
PSF_SIZE	45, 45	The size of the input vignettes
CENTER_KEYS	X_IMAGE, Y_IMAGE	The columns from the *SExtractor* catalog to use when centering sources during sampling
PHOTFLUX_KEY	FLUX_APER(1)	The column from the *SExtractor* catalog to use for photometric normalization
PHOTFLUXERR_KEY	FLUXERR_APER(1)	The column from the *SExtractor* catalog to use when calculating photometric errors
PSFVAR_KEYS	X_IMAGE, Y_IMAGE	The columns from the *SExtractor* catalog for spatial mapping of the PSF
SAMPLEVAR_TYPE	SEEING	Whether it is expected to be variability between different point sources due to seeing (NONE OR SEEING)
SAMPLE_FWHMRANGE	2.0, 10.0	The allowed full-width at half maximum range for the model
SAMPLE_VARIABILITY	0.02	The allowed full-width at half maximum variability between samples
SAMPLE_MINSN	20	The minimum SNR for a source to be considered for building the PSF model
SAMPLE_MAXELLIP	0.1	The maximum ellipticity (a - b) / (a + b) for a source to be considered for building the PSF model

Table B.5: *The list of our* Gaia*-selected sources along with their PMs, parallaxes, their respective errors, and RUWE values.*

ID	RA	Dec	μ_α	μ_δ	ϖ	RUWE
1	19:02:12.03	-37:03:09.7	5.57 ± 0.13	-29.52 ± 0.11	6.41 ±0.12	0.98
2	19:02:43.45	-37:02:25.1	4.56 ± 0.94	-28.60 ± 0.81	6.84 ±0.69	1.25
3	19:00:38.94	-36:58:14.9	7.89 ± 0.29	-28.15 ± 0.23	5.90 ±0.29	1.42
4	19:03:06.83	-37:05:16.6	3.24 ± 0.24	-27.21 ± 0.21	6.53 ±0.24	1.07
5	19:01:33.58	-37:00:30.7	5.04 ± 0.37	-27.48 ± 0.30	6.46 ±0.30	0.97
6	19:01:53.73	-37:00:34.4	5.63 ± 0.26	-27.99 ± 0.22	6.28 ±0.23	1.14
7	19:02:07.71	-37:11:56.2	3.83 ± 0.27	-27.59 ± 0.22	7.01 ±0.25	1.15
8	19:01:04.63	-37:01:29.9	4.09 ± 0.13	-28.50 ± 0.10	6.34 ±0.12	1.12
9	19:02:39.41	-36:53:11.4	4.32 ± 0.10	-27.69 ± 0.08	6.37 ±0.09	1.01
10	19:01:18.95	-36:58:28.4	4.40 ± 0.14	-27.16 ± 0.11	6.61 ±0.12	0.99
11	19:01:11.51	-36:45:34.1	3.56 ± 0.14	-26.48 ± 0.12	6.53 ±0.11	1.06
12	19:00:38.43	-36:52:47.2	6.29 ± 0.86	-27.13 ± 0.67	6.65 ±0.65	1.04
13	19:02:00.88	-36:44:09.3	4.33 ± 0.09	-26.63 ± 0.08	6.43 ±0.09	0.92
14	19:01:39.14	-37:00:17.6	4.43 ± 0.55	-26.48 ± 0.50	6.43 ±0.49	1.23
15	19:02:55.19	-37:04:45.9	3.33 ± 0.20	-26.30 ± 0.17	6.54 ±0.19	1.06

Table B.6: *Our list of candidates for follow-up spectroscopy along with their on-sky position and photometric measurements.*

ID	RA	Dec	I	J	K
1	19:00:20.24	-37:00:49.1	19.85 ± 0.09	16.95 ± 0.02	15.00 ± 0.01
2	19:00:22.69	-36:59:52.6	20.69 ± 0.11	17.14 ± 0.02	14.89 ± 0.01
3	19:00:24.01	-36:59:51.7	21.35 ± 0.10	18.09 ± 0.04	15.97 ± 0.03
4	19:00:24.07	-36:57:35.3	21.61 ± 0.12	18.00 ± 0.04	15.63 ± 0.02
5	19:00:25.24	-36:58:03.2	21.39 ± 0.12	17.58 ± 0.03	15.07 ± 0.01
6	19:00:25.72	-36:57:29.1	21.72 ± 0.13	17.82 ± 0.04	15.26 ± 0.02
7	19:00:26.44	-36:59:09.3	20.96 ± 0.11	17.53 ± 0.03	15.33 ± 0.02
8	19:00:26.50	-36:57:12.9	21.14 ± 0.06	17.85 ± 0.04	15.80 ± 0.03
9	19:00:26.70	-36:58:56.0	20.29 ± 0.11	16.79 ± 0.01	14.64 ± 0.01
10	19:00:27.44	-36:56:23.6	21.04 ± 0.06	17.90 ± 0.04	16.13 ± 0.04
11	19:00:27.62	-36:58:25.1	21.57 ± 0.12	17.77 ± 0.03	15.16 ± 0.02
12	19:00:28.52	-36:57:01.5	20.63 ± 0.08	16.57 ± 0.01	13.92 ± 0.01
13	19:00:31.10	-36:58:29.9	20.58 ± 0.10	17.44 ± 0.03	15.45 ± 0.02
14	19:00:31.22	-36:56:07.9	20.24 ± 0.07	16.53 ± 0.01	14.03 ± 0.01
15	19:00:32.38	-36:55:43.8	20.06 ± 0.08	16.78 ± 0.01	14.52 ± 0.01
16	19:00:33.21	-36:58:10.0	20.60 ± 0.10	17.35 ± 0.02	14.99 ± 0.01
17	19:00:35.23	-36:57:26.1	21.60 ± 0.07	18.28 ± 0.05	16.00 ± 0.03
18	19:00:35.28	-36:54:57.4	19.43 ± 0.07	16.50 ± 0.01	14.58 ± 0.01
19	19:00:35.44	-36:57:30.4	20.28 ± 0.07	16.60 ± 0.01	13.97 ± 0.01
20	19:00:36.21	-36:54:30.1	21.02 ± 0.08	17.81 ± 0.04	16.08 ± 0.03
21	19:00:37.03	-36:58:50.5	21.48 ± 0.10	18.23 ± 0.05	16.10 ± 0.03
22	19:00:38.43	-36:52:47.2	18.68 ± 0.08	15.29 ± 0.00	14.22 ± 0.01
23	19:00:40.35	-36:57:27.2	20.80 ± 0.07	17.46 ± 0.03	15.13 ± 0.01
24	19:00:40.84	-36:56:56.6	20.09 ± 0.07	16.51 ± 0.01	14.02 ± 0.01
25	19:00:41.05	-36:57:07.1	20.79 ± 0.07	17.26 ± 0.02	14.77 ± 0.01
26	19:00:42.54	-36:57:06.8	21.35 ± 0.07	17.65 ± 0.03	15.10 ± 0.01
27	19:00:42.64	-36:56:36.7	21.12 ± 0.07	17.63 ± 0.03	15.25 ± 0.02
28	19:00:44.35	-36:57:28.9	19.74 ± 0.07	15.82 ± 0.01	13.15 ± 0.00
29	19:00:44.76	-36:56:02.2	20.08 ± 0.08	16.07 ± 0.01	13.32 ± 0.00
30	19:00:47.27	-36:57:43.2	20.01 ± 0.06	17.11 ± 0.02	15.17 ± 0.02
31	19:00:50.53	-36:59:04.4	20.57 ± 0.09	17.57 ± 0.03	16.03 ± 0.03
32	19:00:51.51	-36:54:32.1	21.18 ± 0.08	17.72 ± 0.03	15.59 ± 0.02
33	19:00:51.67	-36:52:53.1	20.38 ± 0.07	17.30 ± 0.02	15.34 ± 0.02
34	19:00:51.73	-36:57:35.7	19.99 ± 0.07	16.63 ± 0.01	14.20 ± 0.01
35	19:00:53.11	-36:53:26.6	21.35 ± 0.08	18.07 ± 0.04	16.10 ± 0.03
36	19:00:53.50	-36:57:24.2	21.69 ± 0.07	18.04 ± 0.04	15.31 ± 0.02
37	19:00:53.66	-36:53:42.3	21.63 ± 0.10	17.54 ± 0.03	15.23 ± 0.02
38	19:00:53.98	-36:54:24.7	21.40 ± 0.09	17.84 ± 0.04	15.39 ± 0.02
39	19:00:55.29	-36:57:16.9	21.10 ± 0.07	17.28 ± 0.02	14.52 ± 0.01
40	19:00:56.02	-36:56:30.9	21.46 ± 0.08	17.29 ± 0.02	14.47 ± 0.01

Table B.6 continued from previous page

ID	RA	Dec	I	J	K
41	19:00:57.19	-37:04:06.1	20.59 ± 0.06	17.55 ± 0.03	16.27 ± 0.04
42	19:00:58.74	-36:56:20.7	20.76 ± 0.06	17.25 ± 0.02	14.83 ± 0.01
43	19:00:59.04	-36:53:03.7	20.95 ± 0.08	17.73 ± 0.03	15.84 ± 0.03
44	19:01:00.34	-36:52:52.5	19.47 ± 0.08	16.48 ± 0.01	14.78 ± 0.01
45	19:01:01.22	-36:53:16.7	21.39 ± 0.10	17.22 ± 0.02	14.54 ± 0.01
46	19:01:01.64	-36:55:33.7	21.94 ± 0.09	18.41 ± 0.06	15.97 ± 0.03
47	19:01:01.65	-36:55:50.3	21.11 ± 0.06	17.80 ± 0.04	15.62 ± 0.02
48	19:01:02.35	-36:55:49.4	19.34 ± 0.06	16.10 ± 0.01	13.84 ± 0.01
49	19:01:04.63	-37:01:29.9	15.73 ± 0.08	13.30 ± 0.00	12.14 ± 0.00
50	19:01:06.40	-36:55:21.7	21.07 ± 0.17	17.16 ± 0.02	14.63 ± 0.01
51	19:01:06.57	-36:56:57.3	21.71 ± 0.10	18.23 ± 0.05	16.17 ± 0.04
52	19:01:07.63	-36:52:50.2	20.71 ± 0.13	17.64 ± 0.03	15.59 ± 0.02
53	19:01:10.69	-36:52:23.9	19.65 ± 0.13	16.68 ± 0.01	14.85 ± 0.01
54	19:01:10.79	-36:55:15.2	21.58 ± 0.19	17.18 ± 0.02	14.36 ± 0.01
55	19:01:11.21	-36:56:31.5	21.39 ± 0.09	17.98 ± 0.04	15.57 ± 0.02
56	19:01:11.47	-36:55:44.9	19.62 ± 0.16	15.75 ± 0.01	13.21 ± 0.00
57	19:01:11.51	-36:45:34.1	15.92 ± 0.12	13.28 ± 0.00	12.12 ± 0.00
58	19:01:12.13	-36:50:09.8	19.47 ± 0.12	16.71 ± 0.01	15.24 ± 0.02
59	19:01:12.49	-36:51:58.4	20.88 ± 0.14	17.73 ± 0.03	15.71 ± 0.02
60	19:01:13.53	-36:52:26.1	21.41 ± 0.16	17.61 ± 0.03	15.07 ± 0.01
61	19:01:14.24	-36:52:53.5	20.34 ± 0.14	17.05 ± 0.02	15.03 ± 0.01
62	19:01:14.34	-36:52:55.3	20.47 ± 0.13	17.45 ± 0.03	15.57 ± 0.02
63	19:01:14.73	-36:51:08.2	21.61 ± 0.15	18.32 ± 0.06	16.33 ± 0.04
64	19:01:15.97	-36:52:26.3	20.74 ± 0.16	17.03 ± 0.02	14.60 ± 0.01
65	19:01:16.11	-36:52:51.5	20.47 ± 0.14	17.25 ± 0.02	15.31 ± 0.02
66	19:01:17.60	-36:51:41.7	21.13 ± 0.14	17.88 ± 0.04	15.71 ± 0.02
67	19:01:19.91	-36:51:25.7	21.65 ± 0.16	18.00 ± 0.04	15.73 ± 0.02
68	19:01:20.16	-36:58:01.4	19.73 ± 0.08	16.88 ± 0.02	14.95 ± 0.01
69	19:01:21.30	-36:57:24.2	21.34 ± 0.09	17.89 ± 0.04	15.44 ± 0.02
70	19:01:21.60	-36:51:19.9	20.93 ± 0.14	17.68 ± 0.03	15.67 ± 0.02
71	19:01:23.34	-36:58:22.8	20.82 ± 0.09	17.59 ± 0.03	15.36 ± 0.02
72	19:01:23.48	-36:59:08.1	21.01 ± 0.09	17.46 ± 0.03	15.17 ± 0.02
73	19:01:25.13	-36:55:07.7	19.56 ± 0.13	16.60 ± 0.01	14.63 ± 0.01
74	19:01:26.02	-36:54:00.9	21.98 ± 0.19	17.58 ± 0.03	14.76 ± 0.01
75	19:01:27.51	-37:01:33.6	19.54 ± 0.08	16.54 ± 0.01	14.87 ± 0.01
76	19:01:27.54	-36:52:14.9	19.99 ± 0.15	16.51 ± 0.01	14.40 ± 0.01
77	19:01:28.35	-37:00:05.6	19.46 ± 0.07	16.71 ± 0.01	14.80 ± 0.01
78	19:01:28.62	-36:50:59.1	21.12 ± 0.15	17.67 ± 0.03	15.51 ± 0.02
79	19:01:29.39	-36:59:47.7	21.84 ± 0.10	18.51 ± 0.07	16.64 ± 0.06
80	19:01:29.40	-36:58:40.8	20.06 ± 0.08	17.19 ± 0.02	15.22 ± 0.02
81	19:01:31.48	-36:57:39.0	19.80 ± 0.08	16.73 ± 0.01	14.72 ± 0.01

Table B.6 continued from previous page

ID	RA	Dec	I	J	K
82	19:01:31.72	-36:59:37.0	20.07 ± 0.05	17.12 ± 0.02	15.15 ± 0.01
83	19:01:32.19	-36:57:36.9	20.98 ± 0.09	17.48 ± 0.03	14.91 ± 0.01
84	19:01:33.19	-36:58:18.8	21.94 ± 0.08	17.40 ± 0.02	14.23 ± 0.01
85	19:01:33.58	-37:00:30.7	18.16 ± 0.05	15.18 ± 0.00	14.14 ± 0.01
86	19:01:34.67	-36:51:10.1	20.05 ± 0.08	17.04 ± 0.02	15.27 ± 0.02
87	19:01:37.46	-37:00:36.3	19.76 ± 0.05	16.84 ± 0.02	14.95 ± 0.01
88	19:01:37.89	-36:50:54.5	20.37 ± 0.09	17.06 ± 0.02	15.07 ± 0.01
89	19:01:37.97	-36:59:27.8	19.89 ± 0.06	15.70 ± 0.01	12.98 ± 0.00
90	19:01:38.80	-36:58:46.0	21.75 ± 0.07	17.90 ± 0.04	15.66 ± 0.02
91	19:01:38.80	-37:10:16.4	21.61 ± 0.06	17.91 ± 0.04	16.22 ± 0.04
92	19:01:39.14	-37:00:17.6	18.02 ± 0.06	14.14 ± 0.00	12.37 ± 0.00
93	19:01:40.58	-36:59:34.8	21.92 ± 0.06	18.35 ± 0.06	16.00 ± 0.03
94	19:01:43.09	-36:50:18.4	19.35 ± 0.09	16.52 ± 0.01	14.82 ± 0.01
95	19:01:43.60	-36:50:49.4	21.64 ± 0.11	18.13 ± 0.05	15.95 ± 0.03
96	19:01:44.06	-37:01:31.6	21.67 ± 0.07	18.22 ± 0.05	16.18 ± 0.04
97	19:01:45.36	-36:51:37.7	21.94 ± 0.13	17.96 ± 0.04	15.06 ± 0.01
98	19:01:45.59	-37:03:03.6	20.59 ± 0.06	17.48 ± 0.03	15.50 ± 0.02
99	19:01:46.02	-36:50:34.6	19.26 ± 0.09	16.31 ± 0.01	14.43 ± 0.01
100	19:01:46.90	-36:50:07.6	21.66 ± 0.11	18.35 ± 0.06	16.55 ± 0.05
101	19:01:47.14	-36:51:19.2	20.93 ± 0.10	17.62 ± 0.03	15.42 ± 0.02
102	19:01:47.93	-36:49:40.1	20.42 ± 0.09	17.41 ± 0.02	15.68 ± 0.02
103	19:01:48.06	-36:52:14.1	21.82 ± 0.12	18.28 ± 0.05	15.91 ± 0.03
104	19:01:48.35	-37:00:50.2	21.72 ± 0.07	18.21 ± 0.05	16.01 ± 0.03
105	19:01:48.47	-36:50:14.3	21.20 ± 0.10	17.99 ± 0.04	15.90 ± 0.03
106	19:01:51.11	-37:01:52.3	21.22 ± 0.07	17.65 ± 0.03	15.19 ± 0.02
107	19:01:52.84	-36:51:20.0	20.91 ± 0.12	17.02 ± 0.02	14.18 ± 0.01
108	19:01:53.27	-37:02:14.2	20.83 ± 0.06	17.73 ± 0.03	15.59 ± 0.02
109	19:01:53.48	-36:51:00.8	19.78 ± 0.09	16.87 ± 0.02	14.99 ± 0.01
110	19:01:53.73	-37:00:34.4	17.01 ± 0.06	14.00 ± 0.00	13.07 ± 0.00
111	19:01:54.74	-36:51:19.8	21.89 ± 0.12	18.24 ± 0.05	16.17 ± 0.04
112	19:01:56.51	-36:52:35.2	20.82 ± 0.10	17.73 ± 0.03	15.54 ± 0.02
113	19:01:57.41	-37:03:12.2	19.74 ± 0.07	15.53 ± 0.01	13.25 ± 0.00
114	19:01:57.55	-36:53:15.8	21.66 ± 0.12	17.98 ± 0.04	15.47 ± 0.02
115	19:01:58.48	-36:52:27.2	19.67 ± 0.09	16.82 ± 0.01	14.78 ± 0.01
116	19:01:58.70	-36:53:35.3	21.36 ± 0.15	16.34 ± 0.01	12.63 ± 0.00
117	19:01:58.92	-36:59:41.3	21.77 ± 0.10	16.42 ± 0.01	12.81 ± 0.00
118	19:02:00.78	-36:58:51.5	19.45 ± 0.07	15.68 ± 0.01	13.34 ± 0.00
119	19:02:00.88	-36:44:09.3	15.61 ± 0.07	13.46 ± 0.00	12.67 ± 0.00
120	19:02:02.01	-36:52:58.2	21.66 ± 0.11	18.36 ± 0.06	16.30 ± 0.04
121	19:02:02.09	-37:03:17.8	21.39 ± 0.07	17.89 ± 0.04	15.62 ± 0.02
122	19:02:05.76	-36:54:36.9	19.93 ± 0.06	16.94 ± 0.02	16.06 ± 0.03

Table B.6 continued from previous page

ID	RA	Dec	I	J	K
123	19:02:06.52	-36:53:14.1	21.79 ± 0.08	18.01 ± 0.04	15.51 ± 0.02
124	19:02:07.16	-36:53:39.6	20.89 ± 0.06	17.71 ± 0.03	15.50 ± 0.02
125	19:02:07.71	-37:11:56.2	17.04 ± 0.06	14.02 ± 0.00	12.57 ± 0.00
126	19:02:07.90	-36:53:54.4	19.77 ± 0.07	16.05 ± 0.01	13.42 ± 0.00
127	19:02:08.33	-37:03:30.7	21.12 ± 0.14	17.65 ± 0.03	15.37 ± 0.02
128	19:02:08.33	-37:09:56.3	20.52 ± 0.13	17.34 ± 0.02	15.43 ± 0.02
129	19:02:08.49	-37:11:51.6	19.88 ± 0.06	16.68 ± 0.01	14.96 ± 0.01
130	19:02:08.57	-37:09:38.3	21.10 ± 0.13	17.85 ± 0.04	15.89 ± 0.03
131	19:02:09.74	-37:09:14.4	19.61 ± 0.14	15.94 ± 0.01	13.63 ± 0.00
132	19:02:10.89	-37:03:54.0	20.89 ± 0.14	17.35 ± 0.02	14.83 ± 0.01
133	19:02:11.34	-37:04:13.2	21.06 ± 0.14	17.60 ± 0.03	15.08 ± 0.02
134	19:02:11.57	-37:03:06.2	19.74 ± 0.15	15.88 ± 0.01	13.34 ± 0.00
135	19:02:11.70	-37:08:45.8	20.85 ± 0.14	17.18 ± 0.02	14.89 ± 0.01
136	19:02:12.03	-37:03:09.7	15.91 ± 0.12	13.32 ± 0.00	12.22 ± 0.00
137	19:02:12.34	-36:59:28.3	21.79 ± 0.14	18.28 ± 0.05	16.03 ± 0.03
138	19:02:12.66	-37:07:12.3	19.79 ± 0.13	16.83 ± 0.02	14.81 ± 0.01
139	19:02:14.15	-36:59:30.9	20.13 ± 0.13	16.96 ± 0.02	14.92 ± 0.01
140	19:02:14.19	-36:58:45.8	21.36 ± 0.14	17.82 ± 0.04	15.17 ± 0.02
141	19:02:14.84	-36:59:40.9	19.50 ± 0.14	15.89 ± 0.01	13.47 ± 0.00
142	19:02:14.95	-37:08:48.7	20.54 ± 0.14	17.07 ± 0.02	14.83 ± 0.01
143	19:02:15.69	-37:06:02.7	21.44 ± 0.15	17.63 ± 0.03	15.34 ± 0.02
144	19:02:15.86	-36:59:02.6	21.52 ± 0.16	17.47 ± 0.03	14.69 ± 0.01
145	19:02:15.86	-36:54:37.4	20.91 ± 0.06	17.73 ± 0.03	15.64 ± 0.02
146	19:02:15.88	-36:59:04.4	21.37 ± 0.16	17.05 ± 0.02	14.09 ± 0.01
147	19:02:16.00	-36:45:46.2	21.69 ± 0.08	17.71 ± 0.03	16.22 ± 0.04
148	19:02:17.02	-37:07:43.4	20.12 ± 0.13	16.98 ± 0.02	14.91 ± 0.01
149	19:02:17.36	-37:06:26.2	21.87 ± 0.28	18.49 ± 0.06	16.02 ± 0.04
150	19:02:17.43	-37:09:14.8	21.64 ± 0.27	18.27 ± 0.05	16.14 ± 0.04
151	19:02:18.05	-36:58:24.7	21.87 ± 0.28	18.36 ± 0.06	15.62 ± 0.02
152	19:02:18.23	-36:57:59.7	21.62 ± 0.15	17.90 ± 0.04	15.19 ± 0.02
153	19:02:19.16	-37:00:53.2	21.70 ± 0.28	18.19 ± 0.05	15.63 ± 0.03
154	19:02:19.30	-37:08:33.4	19.45 ± 0.24	16.59 ± 0.01	14.75 ± 0.01
155	19:02:21.22	-37:04:45.7	21.88 ± 0.31	17.89 ± 0.04	15.05 ± 0.02
156	19:02:21.76	-37:06:55.0	21.61 ± 0.27	18.29 ± 0.05	15.90 ± 0.03
157	19:02:24.93	-37:05:25.6	20.74 ± 0.27	17.42 ± 0.03	15.16 ± 0.02
158	19:02:24.93	-36:58:09.6	21.75 ± 0.28	18.29 ± 0.06	17.35 ± 0.13
159	19:02:25.07	-37:00:59.0	20.88 ± 0.30	17.00 ± 0.02	14.21 ± 0.01
160	19:02:25.14	-37:08:00.9	21.45 ± 0.27	18.17 ± 0.05	16.09 ± 0.03
161	19:02:25.65	-36:59:55.7	21.26 ± 0.33	16.88 ± 0.02	13.52 ± 0.00
162	19:02:26.03	-36:58:31.6	20.99 ± 0.26	17.87 ± 0.04	15.81 ± 0.03
163	19:02:26.13	-36:57:16.0	21.51 ± 0.14	18.03 ± 0.05	15.87 ± 0.03

Table B.6 continued from previous page

ID	RA	Dec	I	J	K
164	19:02:26.28	-36:59:02.2	21.85 ± 0.28	18.47 ± 0.06	15.93 ± 0.03
165	19:02:26.34	-37:05:15.2	21.44 ± 0.30	17.59 ± 0.03	14.89 ± 0.01
166	19:02:26.43	-37:07:15.0	20.33 ± 0.27	17.01 ± 0.02	14.68 ± 0.01
167	19:02:26.79	-36:56:00.4	19.73 ± 0.13	16.81 ± 0.02	14.79 ± 0.01
168	19:02:27.01	-37:10:33.1	21.18 ± 0.29	17.50 ± 0.03	15.13 ± 0.01
169	19:02:27.13	-37:00:02.6	21.38 ± 0.30	17.51 ± 0.03	14.73 ± 0.01
170	19:02:27.20	-37:08:51.2	20.54 ± 0.25	17.53 ± 0.03	15.54 ± 0.02
171	19:02:27.26	-37:00:02.1	20.39 ± 0.29	16.57 ± 0.01	13.86 ± 0.01
172	19:02:28.11	-36:58:30.1	21.97 ± 0.28	18.43 ± 0.06	15.94 ± 0.03
173	19:02:28.23	-36:58:09.4	21.75 ± 0.29	18.15 ± 0.05	15.91 ± 0.03
174	19:02:28.25	-36:56:23.6	21.09 ± 0.18	16.46 ± 0.01	12.97 ± 0.00
175	19:02:28.91	-36:58:50.2	21.00 ± 0.28	17.50 ± 0.03	15.05 ± 0.01
176	19:02:29.48	-36:56:08.7	20.61 ± 0.15	16.95 ± 0.02	14.39 ± 0.01
177	19:02:29.97	-37:00:20.7	21.63 ± 0.27	18.36 ± 0.06	16.28 ± 0.04
178	19:02:30.30	-36:57:41.2	21.56 ± 0.14	18.26 ± 0.06	15.87 ± 0.03
179	19:02:30.38	-36:56:49.0	21.54 ± 0.14	18.29 ± 0.06	15.83 ± 0.03
180	19:02:30.43	-36:59:01.1	19.75 ± 0.26	16.61 ± 0.01	14.38 ± 0.01
181	19:02:30.52	-36:56:55.3	21.91 ± 0.15	18.42 ± 0.07	15.89 ± 0.03
182	19:02:31.16	-36:56:07.0	19.80 ± 0.14	16.19 ± 0.01	13.70 ± 0.01
183	19:02:32.05	-36:56:18.1	20.42 ± 0.15	16.75 ± 0.02	14.36 ± 0.01
184	19:02:32.12	-37:05:35.0	19.56 ± 0.24	16.79 ± 0.01	14.94 ± 0.01
185	19:02:32.26	-36:59:01.7	19.39 ± 0.24	16.52 ± 0.01	14.62 ± 0.01
186	19:02:32.45	-37:07:04.4	21.76 ± 0.28	18.32 ± 0.06	16.32 ± 0.04
187	19:02:33.19	-36:57:26.0	20.58 ± 0.08	17.15 ± 0.02	15.34 ± 0.02
188	19:02:33.83	-36:59:34.0	19.97 ± 0.26	16.76 ± 0.02	14.60 ± 0.01
189	19:02:33.98	-37:07:33.6	20.02 ± 0.25	17.09 ± 0.02	15.22 ± 0.02
190	19:02:34.05	-37:00:47.2	20.61 ± 0.28	17.01 ± 0.02	14.93 ± 0.01
191	19:02:34.06	-36:58:29.0	21.53 ± 0.28	18.04 ± 0.04	15.63 ± 0.02
192	19:02:34.19	-36:56:04.2	19.83 ± 0.12	16.97 ± 0.02	15.10 ± 0.02
193	19:02:34.21	-36:56:57.1	20.99 ± 0.14	17.42 ± 0.03	15.21 ± 0.02
194	19:02:34.30	-37:08:40.1	21.97 ± 0.33	17.72 ± 0.03	14.60 ± 0.01
195	19:02:34.60	-37:04:48.6	20.39 ± 0.27	16.98 ± 0.02	14.72 ± 0.01
196	19:02:35.05	-37:01:29.1	21.84 ± 0.29	18.18 ± 0.05	15.50 ± 0.02
197	19:02:35.15	-36:57:29.0	20.00 ± 0.13	17.08 ± 0.02	15.18 ± 0.02
198	19:02:35.51	-36:58:14.7	19.49 ± 0.25	16.41 ± 0.01	14.26 ± 0.01
199	19:02:36.02	-37:05:07.7	20.72 ± 0.27	17.33 ± 0.02	15.13 ± 0.02
200	19:02:36.03	-36:58:44.2	21.66 ± 0.28	18.23 ± 0.05	15.84 ± 0.03
201	19:02:36.49	-36:58:18.1	20.47 ± 0.25	17.45 ± 0.03	15.44 ± 0.02
202	19:02:36.65	-36:59:26.7	20.51 ± 0.25	17.51 ± 0.03	15.52 ± 0.02
203	19:02:36.80	-37:02:59.0	20.64 ± 0.33	16.22 ± 0.01	13.09 ± 0.00
204	19:02:37.22	-37:04:29.8	19.97 ± 0.26	16.75 ± 0.01	14.60 ± 0.01

Table B.6 continued from previous page

ID	RA	Dec	I	J	K
205	19:02:37.29	-37:04:32.8	21.67 ± 0.27	18.27 ± 0.05	15.89 ± 0.03
206	19:02:37.89	-37:01:38.3	20.18 ± 0.29	16.53 ± 0.01	14.09 ± 0.01
207	19:02:38.37	-37:01:25.9	21.67 ± 0.28	18.19 ± 0.05	15.73 ± 0.03
208	19:02:38.37	-37:05:45.6	20.25 ± 0.29	16.60 ± 0.01	14.05 ± 0.01
209	19:02:38.40	-37:05:25.5	20.00 ± 0.29	16.26 ± 0.01	13.59 ± 0.00
210	19:02:39.41	-36:53:11.4	15.61 ± 0.06	13.16 ± 0.00	12.13 ± 0.00
211	19:02:39.82	-36:57:31.1	21.27 ± 0.14	17.97 ± 0.04	15.73 ± 0.03
212	19:02:39.97	-37:02:55.1	21.99 ± 0.28	18.53 ± 0.07	16.17 ± 0.04
213	19:02:40.04	-36:57:19.0	20.42 ± 0.13	17.45 ± 0.03	15.44 ± 0.02
214	19:02:40.17	-36:57:49.5	20.51 ± 0.15	16.88 ± 0.02	14.39 ± 0.01
215	19:02:40.53	-37:03:07.0	21.72 ± 0.29	18.09 ± 0.04	15.50 ± 0.02
216	19:02:40.56	-37:09:20.2	21.94 ± 0.29	18.27 ± 0.05	15.48 ± 0.02
217	19:02:40.70	-37:02:36.1	20.64 ± 0.28	17.15 ± 0.02	14.91 ± 0.01
218	19:02:40.83	-37:00:06.8	19.42 ± 0.24	16.69 ± 0.01	14.89 ± 0.01
219	19:02:41.01	-37:10:03.7	20.14 ± 0.14	17.08 ± 0.02	15.10 ± 0.01
220	19:02:41.27	-36:57:15.9	20.50 ± 0.13	17.50 ± 0.03	15.59 ± 0.02
221	19:02:41.48	-37:03:21.8	21.82 ± 0.15	18.47 ± 0.06	16.27 ± 0.04
222	19:02:41.55	-37:02:21.0	19.58 ± 0.15	16.12 ± 0.01	13.89 ± 0.01
223	19:02:41.99	-36:58:28.0	20.66 ± 0.15	17.09 ± 0.02	14.78 ± 0.01
224	19:02:42.60	-37:03:22.8	21.12 ± 0.14	17.92 ± 0.04	15.91 ± 0.03
225	19:02:43.08	-37:09:59.6	20.23 ± 0.14	17.10 ± 0.02	15.05 ± 0.01
226	19:02:43.09	-36:59:20.0	21.20 ± 0.14	18.02 ± 0.04	16.01 ± 0.03
227	19:02:43.23	-36:59:03.7	21.44 ± 0.15	17.80 ± 0.04	15.42 ± 0.02
228	19:02:43.32	-36:58:37.6	21.62 ± 0.17	17.48 ± 0.03	14.71 ± 0.01
229	19:02:43.70	-37:04:36.8	21.21 ± 0.14	17.93 ± 0.04	15.94 ± 0.03
230	19:02:43.93	-37:02:31.0	21.98 ± 0.15	18.47 ± 0.06	16.07 ± 0.03
231	19:02:44.31	-36:57:59.0	21.50 ± 0.14	18.18 ± 0.05	15.94 ± 0.03
232	19:02:44.49	-37:04:15.6	19.83 ± 0.14	16.58 ± 0.01	14.52 ± 0.01
233	19:02:45.24	-36:59:40.7	20.15 ± 0.14	17.06 ± 0.02	15.06 ± 0.02
234	19:02:45.72	-37:07:23.3	21.24 ± 0.19	16.41 ± 0.01	12.95 ± 0.00
235	19:02:46.44	-36:58:24.2	20.67 ± 0.15	17.22 ± 0.02	15.00 ± 0.01
236	19:02:47.08	-37:09:11.0	19.50 ± 0.13	16.59 ± 0.01	14.77 ± 0.01
237	19:02:47.18	-37:09:19.8	20.73 ± 0.15	17.24 ± 0.02	15.28 ± 0.02
238	19:02:47.65	-37:02:15.4	20.56 ± 0.16	16.75 ± 0.01	14.35 ± 0.01
239	19:02:48.01	-37:04:24.9	20.12 ± 0.13	17.15 ± 0.02	15.34 ± 0.02
240	19:02:48.46	-37:04:51.5	21.87 ± 0.15	18.25 ± 0.05	15.99 ± 0.03
241	19:02:48.78	-36:59:10.4	21.52 ± 0.15	18.21 ± 0.05	16.29 ± 0.05
242	19:02:49.27	-37:08:34.1	21.65 ± 0.15	18.08 ± 0.05	15.68 ± 0.02
243	19:02:49.55	-36:57:43.8	19.67 ± 0.15	16.07 ± 0.01	13.72 ± 0.01
244	19:02:49.63	-37:08:43.0	20.69 ± 0.14	17.62 ± 0.03	15.64 ± 0.02
245	19:02:49.66	-37:00:32.9	21.89 ± 0.15	18.44 ± 0.06	16.43 ± 0.05

Table B.6 continued from previous page

ID	RA	Dec	I	J	K
246	19:02:49.86	-37:03:29.2	21.55 ± 0.15	17.96 ± 0.04	15.82 ± 0.03
247	19:02:50.08	-37:01:03.6	19.52 ± 0.13	16.56 ± 0.01	14.65 ± 0.01
248	19:02:50.15	-37:02:38.7	21.31 ± 0.17	17.24 ± 0.02	14.58 ± 0.01
249	19:02:50.79	-37:03:56.2	21.11 ± 0.14	17.74 ± 0.03	15.57 ± 0.02
250	19:02:51.39	-37:00:39.0	21.02 ± 0.14	17.87 ± 0.04	15.89 ± 0.03
251	19:02:52.29	-37:09:14.0	21.74 ± 0.15	18.16 ± 0.05	15.90 ± 0.03
252	19:02:52.43	-37:09:19.2	19.79 ± 0.13	16.83 ± 0.02	14.90 ± 0.01
253	19:02:53.52	-37:04:12.1	20.85 ± 0.14	16.64 ± 0.01	14.21 ± 0.01
254	19:02:53.90	-36:52:54.1	21.47 ± 0.10	17.34 ± 0.02	15.88 ± 0.03
255	19:02:54.50	-36:58:50.1	20.50 ± 0.11	17.40 ± 0.03	15.52 ± 0.02
256	19:02:55.12	-37:02:34.8	20.12 ± 0.11	16.95 ± 0.02	15.13 ± 0.01
257	19:02:55.20	-36:56:07.6	19.50 ± 0.06	16.76 ± 0.01	14.98 ± 0.01
258	19:02:56.22	-37:02:04.8	20.21 ± 0.11	17.16 ± 0.02	15.36 ± 0.02
259	19:02:56.22	-37:04:59.6	21.53 ± 0.13	17.81 ± 0.04	15.26 ± 0.02
260	19:02:56.32	-36:59:18.2	21.52 ± 0.12	18.18 ± 0.05	16.22 ± 0.04
261	19:02:56.88	-37:01:12.3	21.62 ± 0.12	18.24 ± 0.05	16.35 ± 0.04
262	19:02:57.52	-37:08:43.9	20.47 ± 0.13	16.52 ± 0.01	13.96 ± 0.01
263	19:02:58.08	-37:04:47.3	20.64 ± 0.11	17.30 ± 0.02	15.06 ± 0.01
264	19:02:58.12	-37:09:57.9	19.54 ± 0.11	16.55 ± 0.01	14.67 ± 0.01
265	19:02:58.45	-37:04:03.7	20.62 ± 0.11	17.33 ± 0.02	15.31 ± 0.02
266	19:02:59.15	-37:04:22.4	21.90 ± 0.12	18.57 ± 0.07	16.40 ± 0.05
267	19:02:59.21	-36:57:12.9	20.91 ± 0.07	17.73 ± 0.03	15.83 ± 0.03
268	19:02:59.58	-37:02:26.6	19.87 ± 0.13	15.75 ± 0.01	13.17 ± 0.00
269	19:02:59.65	-37:10:39.1	19.93 ± 0.11	16.84 ± 0.02	14.76 ± 0.01
270	19:02:59.82	-37:09:36.1	21.40 ± 0.12	17.84 ± 0.04	15.60 ± 0.02
271	19:03:00.28	-36:58:33.9	21.64 ± 0.12	18.27 ± 0.06	16.25 ± 0.04
272	19:03:00.29	-37:11:01.4	20.65 ± 0.11	17.51 ± 0.03	15.48 ± 0.02
273	19:03:00.67	-37:04:39.4	21.95 ± 0.12	18.54 ± 0.07	16.30 ± 0.04
274	19:03:00.67	-37:01:22.5	19.37 ± 0.10	16.50 ± 0.01	14.61 ± 0.01
275	19:03:01.25	-37:09:35.4	21.35 ± 0.12	17.82 ± 0.04	15.64 ± 0.02
276	19:03:01.56	-37:04:47.6	20.88 ± 0.11	17.56 ± 0.03	15.48 ± 0.02
277	19:03:02.77	-37:10:40.4	20.15 ± 0.11	17.04 ± 0.02	14.95 ± 0.01
278	19:03:02.92	-37:11:34.3	21.34 ± 0.14	16.95 ± 0.02	13.83 ± 0.01
279	19:03:03.13	-37:04:30.7	20.58 ± 0.11	17.55 ± 0.03	15.53 ± 0.02
280	19:03:03.65	-37:10:04.4	20.83 ± 0.12	17.38 ± 0.02	15.02 ± 0.01
281	19:03:03.85	-37:11:30.3	21.75 ± 0.14	17.58 ± 0.03	14.80 ± 0.01
282	19:03:03.97	-36:57:52.8	21.99 ± 0.08	18.62 ± 0.08	16.61 ± 0.06
283	19:03:04.40	-37:02:35.6	19.34 ± 0.11	16.16 ± 0.01	14.20 ± 0.01
284	19:03:05.07	-36:59:15.5	20.16 ± 0.10	17.23 ± 0.02	15.53 ± 0.02
285	19:03:05.45	-37:03:29.4	20.23 ± 0.10	17.30 ± 0.02	15.54 ± 0.02
286	19:03:06.66	-37:03:10.6	21.39 ± 0.12	18.05 ± 0.04	16.04 ± 0.03

Table B.6 continued from previous page

ID	RA	Dec	I	J	K
287	19:03:06.96	-36:55:53.3	20.36 ± 0.07	17.12 ± 0.02	15.44 ± 0.02
288	19:03:07.03	-36:58:26.0	19.52 ± 0.10	16.75 ± 0.01	15.04 ± 0.01
289	19:03:07.11	-37:06:35.7	21.63 ± 0.12	18.17 ± 0.05	15.93 ± 0.03
290	19:03:07.23	-37:11:36.2	20.80 ± 0.14	16.33 ± 0.01	12.95 ± 0.00
291	19:03:08.41	-36:56:27.4	20.95 ± 0.07	17.84 ± 0.04	15.97 ± 0.03
292	19:03:08.51	-37:02:57.7	21.15 ± 0.11	17.88 ± 0.04	15.84 ± 0.03
293	19:03:11.27	-36:58:47.0	21.81 ± 0.12	18.45 ± 0.06	16.71 ± 0.06
294	19:03:11.33	-36:58:12.5	19.60 ± 0.11	16.49 ± 0.01	14.87 ± 0.01
295	19:03:11.58	-37:08:38.2	19.97 ± 0.11	16.87 ± 0.02	14.92 ± 0.01
296	19:03:11.68	-37:08:20.9	19.46 ± 0.11	16.33 ± 0.01	14.37 ± 0.01
297	19:03:11.98	-37:10:03.5	21.90 ± 0.14	17.68 ± 0.03	14.98 ± 0.01
298	19:03:12.25	-37:07:26.2	20.71 ± 0.12	17.20 ± 0.02	14.98 ± 0.01
299	19:03:12.26	-37:06:40.1	19.27 ± 0.11	16.25 ± 0.01	14.38 ± 0.01
300	19:03:12.75	-37:07:21.8	20.87 ± 0.12	17.39 ± 0.02	15.10 ± 0.01
301	19:03:13.03	-37:09:46.9	20.12 ± 0.10	17.19 ± 0.02	15.23 ± 0.02
302	19:03:13.21	-37:06:36.0	21.10 ± 0.13	17.20 ± 0.02	14.95 ± 0.01
303	19:03:15.90	-37:10:46.6	21.55 ± 0.12	18.06 ± 0.04	15.76 ± 0.03
304	19:03:17.94	-37:10:18.7	21.15 ± 0.12	17.60 ± 0.03	15.32 ± 0.02
305	19:03:19.24	-37:09:43.5	19.69 ± 0.11	16.67 ± 0.01	14.74 ± 0.01
306	19:03:20.02	-37:06:37.9	19.69 ± 0.12	16.19 ± 0.01	14.08 ± 0.01
307	19:03:22.19	-36:51:03.0	21.63 ± 0.08	18.36 ± 0.06	17.80 ± 0.17
308	19:03:22.54	-37:03:46.1	21.70 ± 0.12	18.24 ± 0.05	16.95 ± 0.08
309	19:03:23.75	-37:06:38.0	19.67 ± 0.10	16.75 ± 0.01	14.84 ± 0.01
310	19:03:24.59	-37:07:57.4	20.93 ± 0.12	17.40 ± 0.02	15.50 ± 0.02
311	19:03:25.10	-36:50:54.6	20.99 ± 0.08	17.77 ± 0.03	17.20 ± 0.09
312	19:03:25.30	-37:07:10.9	20.88 ± 0.11	17.64 ± 0.03	16.01 ± 0.03
313	19:03:27.09	-37:08:19.6	21.35 ± 0.11	18.08 ± 0.05	16.45 ± 0.05
314	19:02:43.45	-37:02:25.1	18.35 ± 0.18	13.82 ± 0.00	11.43 ± 0.00
315	19:00:38.94	-36:58:14.9	16.56 ± 0.12	12.60 ± 0.00	10.92 ± 0.00
316	19:03:06.83	-37:05:16.6	16.91 ± 0.11	13.58 ± 0.00	11.95 ± 0.00
317	19:01:18.95	-36:58:28.4	16.09 ± 0.09	12.70 ± 0.00	11.01 ± 0.00
318	19:02:55.19	-37:04:45.9	16.55 ± 0.13	12.66 ± 0.00	11.30 ± 0.00
319	19:00:25.93	-36:56:33.4	21.72 ± 0.12	18.05 ± 0.04	0.00 ± 0.00
320	19:01:32.33	-36:58:02.8	19.56 ± 0.07	14.84 ± 0.00	11.67 ± 0.00
321	19:01:33.87	-36:57:44.8	19.61 ± 0.08	14.20 ± 0.00	11.11 ± 0.00
322	19:01:51.09	-36:54:11.8	20.61 ± 0.17	14.72 ± 0.00	11.65 ± 0.00
323	19:02:29.16	-37:03:30.7	21.06 ± 0.43	14.96 ± 0.00	10.74 ± 0.00
324	19:02:32.73	-36:57:26.1	21.55 ± 0.14	18.23 ± 0.06	0.00 ± 0.00
325	19:03:02.95	-37:07:03.8	21.59 ± 0.19	15.38 ± 0.00	11.59 ± 0.00
326	19:03:15.58	-36:53:31.1	20.66 ± 0.08	17.30 ± 0.02	0.00 ± 0.00
327	19:03:15.97	-36:53:49.2	20.90 ± 0.08	17.30 ± 0.02	0.00 ± 0.00

Table B.6 continued from previous page

ID	RA	Dec	I	J	K
328	19:03:15.98	-36:53:34.3	20.39 ± 0.07	17.25 ± 0.02	0.00 ± 0.00

Table B.7: *The proposed fields-of-view for follow-up spectroscopy using the KMOS instrument at the VLT.*

FOV	Center (RA)	Center (DEC)	Guide Stars Available	Number of Candidates
A	285.7142443	-37.0702128	1	41
B	285.6461897	-36.9783155	2	53
C	285.5990377	-37.1364681	1	24
D	285.4702481	-36.8738127	2	22
E	285.3893672	-37.0072980	5	20
F	285.2954080	-36.9095669	5	28
G	285.1591031	-36.9402423	4	31